TECHNISCHE UNIVERSITÄT MÜNCHEN

Institut für Wasserchemie und Chemische Balneologie

Lehrstuhl für Analytische Chemie

Applications of D_2O Labelling Combined with Raman Microscopy for Mycobacteria Analysis and Application of SERS for the Investigation of Photocatalytic Reaction

Li Qiu

Vollständiger Abdruck der von der Fakultät für Chemie der Technischen Universität München zur Erlangung des akademischen Grades eines

Doktors der Naturwissenschaften (Dr. rer. nat.)

genehmigten Dissertation.

Vorsitzender: Prof. Dr. Martin Elsner

Prüfer der Dissertation: 1. apl. Prof. Dr. Christoph Haisch

2. Prof. Dr. Ulrich K. Heiz

Die Dissertation wurde am 30.06.2020 bei der Technischen Universität München eingereicht und durch die Fakultät für Chemie am 22.09.2020 angenommen

Acknowledgements

This thesis is based on research performed at the Institute of Hydrochemistry Chair of Analytical Chemistry and Water Chemistry, Technical University of Munich from October 2016 to October 2019 with financial support from the China Scholarship Council (CSC). I would like to give my gratitude to everyone who helped me during my doctoral project, directly or indirectly. It is impossible to complete this thesis without the kind help of them.

First of all, I would like to express my sincere gratitude to Prof. Dr. Christoph Haisch for his friendly supervision. The thesis could not have been completed without his patient guidance. He gave me great guidance and encouragement in the process of selecting research topics, writing manuscripts and improving my English expression. It is a pleasure to work and study under his guidance. I am very grateful for this.

Also, Many thanks to Prof. Dr. Reinhard Nieβner and Prof. Dr. Martin Elsner for their discussions and academic comments on my experimental results at the institute seminars.

Many thanks to PD Dr. Andreas Wieser, Dr. Anna-Cathrine Neumann-Cip, Niki Kriwull and Gabi Liegl who are from Max von Pettenkofer-Institute (MVP), Ludwig-Maximilians-University Munich for their microbiology support.

I also would like to thank all my colleagues in the institute for the academic environment. In particular, a special thank you to the past and present colleagues in the Laser group. In particular, I thank my research partner David Bauer, PhD candidate, for the valuable discussions on experiments and data evaluation using of MATLAB. I thank Dr. Genny A. Pang for her help in paper preparation. Thanks for her friendship and patience. I also thank Dr. Karin Wieland and Dr. Klemens Thaler for their friendship and patience.

Moreover, special thanks to Christine Benning for her kindness in scanning electron microscopy characterization.

At last, many thanks go to my parents for their understanding of my stay abroad and not being able to accompany them often. And special thanks to my husband who helped me and shared my anxiety, depression and happiness in my work. Thanks for all the support from him, without which

Acknowledgements

I would not keep fighting for three years. Many thanks also go to my two sisters and friends in China, for their continuing encouragement.

Publications

The following articles were published during the period of my doctoral study.

Journal papers

Qiu, L., Pang, G. A., Zheng, G., Bauer, D., Wieland, K., & Haisch, C. (2020). Kinetic and mechanistic investigation of the photocatalyzed surface reduction of 4-nitrothiophenol observed on a silver plasmonic film via surface-enhanced Raman scattering, *ACS Applied Materials & Interfaces*.

Bauer, D., Wieland, K., **Qiu, L.**, Neumann-Cip, A. C., Magistro, G., Stief, C. G., ... & Haisch, C. (2020). Heteroresistant bacteria detected by an extended Raman-based antibiotic susceptibility test, *Analytical Chemistry*.

Conference papers

Bauer, D., **Qiu, L**., Wieland, K., Neumann-Cip, A. C., Wieser, A., Magistro, G., ... & Haisch, C. (2020, February). Deuterium uptake in combination with Raman spectroscopy as a tool to investigate antibiotic susceptibility of bacteria. In *Photonic Diagnosis, Monitoring, Prevention, and Treatment of Infections and Inflammatory Diseases 2020* (Vol. 11223, p. 1122302). International Society for Optics and Photonics.

Pang, G. A., **Qiu, L**., Haisch, C., & Laufer, J. (2019, February). Towards biochemical sensing with gold nanoparticles through suppression of nonlinear photoacoustic signal generation. In *Photons Plus Ultrasound: Imaging and Sensing 2019* (Vol. 10878, p. 108786Q). International Society for Optics and Photonics.

Abstract

In this study, D_2O labelling combined with single-cell Raman imaging (SCRI) was applied for the investigation of the metabolic mechanism of mycobacteria. Bacterial cells were fixed on a hydrophobic glass slide surface and measured in an aqueous environment. Numbers of single cell were randomly selected for Raman imaging. Multiple linear regression (MLR) was used for quantitative evaluation. The bacterial metabolic activity was evaluated by calculating the ratio between the deuterium-labeled macromolecules and the non-labeled macromolecules which is defined as the intensity ratio between newly appeared carbon-deuterium (C-D) band and the original carbon-hydrogen (C-H) band. Through the data evaluation, the C-D content distribution in individual cells can be visualized along the longest cell length. The metabolic heterogeneity in individual mycobacterial cells and the differential responses of mycobacteria to different antibiotics at single-cell level were determined. In addition, asymmetric growth of mycobacteria was observed through Raman imaging.

In a second part, the reaction kinetics and mechanism of hydrogenation of 4-nitrothiophenol (4-NTP) to 4-aminothiophenol (4-ATP) were systematically investigated via surface-enhanced Raman microscopy (SERS). The SERS measurements were performed using a new type of simple and cheap silver plasmonic film, which enables monitoring of the reaction under difference conditions. The reaction was observed as the concentration of H^+ and Cl^- were carefully controlled, and the formation of the aromatic azo specie 4, 4-dimercaptoazobenzene (DMAB) and other intermediates of the 4-NTP to 4-ATP reduction was detected only under conditions of low H^+-concentration or limited Cl^--concentration. The reaction rate constant describing the disappearance of 4-NTP was quantitatively determined and was found to vary linearly with the H^+-concentration. Based on the kinetic traces of the intermediates, a reaction mechanism for the 4-NTP to 4-ATP reduction is suggested, and rate constants for the individual reactions are presented that fit the measured kinetic traces.

Contents

1 Introduction

1 Introduction

Mycobacterium tuberculosis (*M. tuberculosis*) causes the disease tuberculosis (TB). TB is easy to catch, but difficult to diagnose. It is still endangering people's health and millions of people die from TB each year.[1] The high lipid and mycolic acid content of the mycobacterial cell wall enable the organism's resistance to chemical damage and dehydration, which limits the effectiveness of drug treatment. It is known that heterogeneous growth and division in Mycobacteria cause the appearance of physiologically distinct subpopulations of bacterial cells.[2] This population diversification enables heterogeneous metabolic activities in response to antibiotics. To understand the mechanism of action of different antibiotics, vibrational imaging method has been applied as a label-free method.

In the past few years, Raman microscopy has been widely used in biological applications because of its characteristics in molecular structure information and quantification capabilities. Raman spectra of bacteria feature an intense carbon-hydrogen (C-H) band in a high wavenumber range (2800-3100 cm^{-1}), which is generated by bacterial macromolecules, such as lipids, proteins, and DNA. The incorporation of D_2O into bacterial macromolecules will lead to the appearance of a new Raman band which is carbon-deuterium bond (C-D). Thus, D_2O labeling combined with Raman microscopy came into people's sight to identify active microbial cells in a complex matrix in 2015.[3] Since then, it has been used for different purposes, such as metabolic activities tracking in animal,[4] characterizing the presence and activity of phosphate solubilizing bacteria (PBS) in complex soil communities,[5] rapid antibiotic susceptibility testing,[6] investigation of cellular metabolic activity in response to antibiotic treatment (NaF, chlorhexidine, and ampicillin),[7] and investigation of the metabolic activities of bacterial persister cells.[8] In these studies, incorporation of deuterium from D_2O into bacterial macromolecules combined with Raman microscopy was demonstrated to be a universal technique in diverse biological applications. In imaging applications, the metabolic heterogeneity of animal cells (size of 100 μm × 100 μm) have been visualized.[4, 9, 10] According to a quantitative calculation in single-cell Raman imaging (SCRI), the C-H to C-D band shift can be used as a powerful indicator correlating to bacterial intercellular and intracellular heterogeneous metabolic activity.

In photochemical reactions, understanding selective surface photocatalytic reaction mechanisms is critical for optimizing many energy conversion applications. Measuring time-resolved concentration profiles of the reactants, products, and intermediates during such reactions is a key

step in elucidating these reaction mechanisms and understanding the role of hot electrons. Surface-enhanced Raman scattering (SERS) is an interface-selective vibrational spectroscopic technique that uses light to excite surface plasmons of a metal surface, typically on metal nanostructures, to enhance Raman scattering. SERS is capable of in-situ detection of chemical reaction processes,[11-14] making it an ideal technique for monitoring selective surface photocatalytic chemical reactions because of the inherent presence of photons. Moreover, SERS does not require the complicated separation and purifying steps that are necessary in conventional analytical techniques, such as, gas chromatography, liquid chromatography and nuclear magnetic resonance.

Aim of this work

There are two main parts of this thesis. In the first section, the aim is to find a way to visualize the intracellular heterogeneity and intercellular heterogeneity in mycobacteria. This is beneficial for understanding the mechanism of antibiotic action in mycobacteria. To gain a deep understanding of mycobacterial metabolic activity within individual cells, SCRI combined with deuterium labelling was used for the observation. MLR was used for quantitative evaluation. Bacterial metabolic activity was evaluated by calculating the ratio between the deuterium-labeled macromolecules and the non-labeled macromolecules which is defined as the intensity ratio between newly appeared C-D stretching band and the original C-H stretching band. Through the data evaluation, the C-D content distribution in individual cells could be visualized along the longest axis. The metabolic heterogeneity in individual mycobacterial cells and the differential responses of mycobacteria to different antibiotics at single-cell level were determined.

In the second part of this thesis, to have a better understanding of the model photoreaction (hydrogenation of 4-nitrothiophenol (4-NTP) to 4-aminothiophenol (4-ATP)), a simple method was described to inexpensively prepare a plasmonic film (AgPF) composed of silver nanoparticles (AgNPs) for SERS experiments. Using this AgPF as a catalyst, we were able to systematically control the concentrations of positive and negative ions in the reaction environment and observe the selective surface reduction of 4-NTP with SERS under different conditions. Using time-resolved SERS measurements, we obtained concentration time histories of the reactants, intermediates, and products of the 4-NTP to 4-ATP reduction, and used these measurements to propose a reaction mechanism for the process and determine individual reaction rate constants.

2 Fundamentals

2.1 Raman microscopy basics

2.1.1 Theory of Raman scattering

The phenomenon of inelastic light scattering was initially predicted by Adolf Smekal in 1923.[15] Afterward, it was experimentally proven by C. V. Raman and his coworkers in 1928.[16, 17] Later on, the scattering was named Raman scattering after C. V. Raman. Raman scattering is a type of secondary radiation.[17] It appears when light strikes and is inelastically scattered by molecules. When considering Raman scattering, there are two theories for interpretation, (1) the classical scattering theory[18, 19] and (2) the quantum scattering theory.[20]

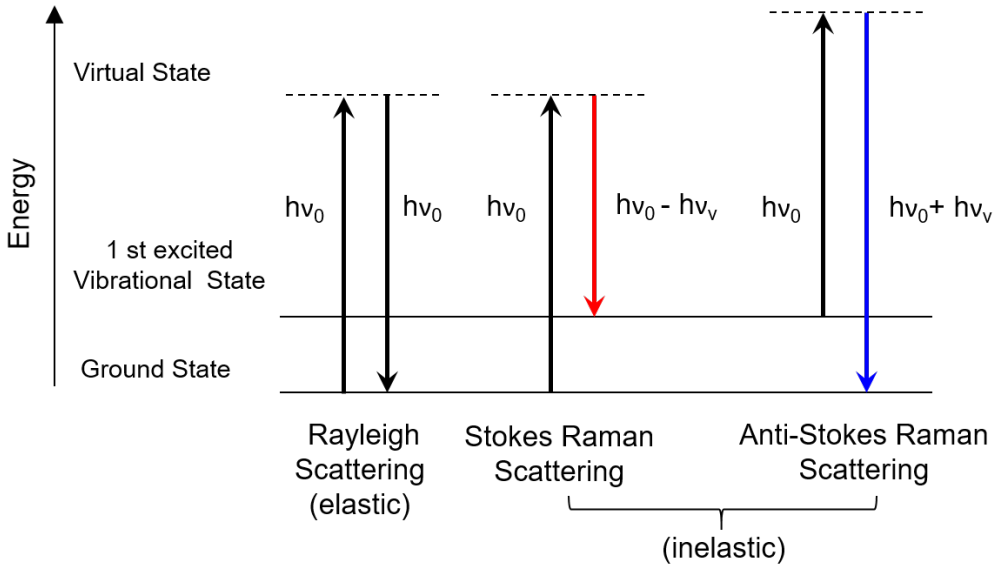

Figure 2.1 Schematic diagram of Rayleigh and Raman scattering. The relation of $h\nu_0$ indicates the energy of incident photons, $h\nu_0 \pm h\nu_v$ represents the Raman scattered photons (anti-Stokes Raman and Stokes Raman, respectively.)

In the classical scattering theory, light is considered as electromagnetic radiation with an electric field (E). This electric field interacts with a molecule and distorts the molecule's electron cloud. The term molecule polarizability (α) is used to indicate the extent to which a molecule's electron cloud is affected by the electric field. The electric field induces an electric dipole moment (P) by interacting with molecule bonds.

$$P = \alpha E \qquad \text{eq. 1}$$

This moment deforms the molecule cloud. The deformation is periodic, and the molecules vibrate at characteristic frequencies. Thus, the molecule can be identified by frequency shifts. In the quantum scattering theory, light is described as a photon that strikes molecules and scatters inelastically. From Figure 2.1, we can see that there are two different kinds of scattered photons when incident monochromatic light strikes the molecule to a virtual energy state, they are elastic and inelastic scattering processes. In most cases, the scattered light is elastic (Rayleigh scattering) that has no energy exchange between incident photons and scattered photons. This elastic scattering does not provide useful information. The rest scattered light is inelastic (Raman scattering) due to molecule vibrational and rotational modes. Only very few of the incident light is Raman scattered. This part of Raman scattering results from energy exchange. The energy of Raman scattered light can be either higher or lower than the energy of incident light source. The higher one is anti-Stokes scattering and the lower is Stokes scattering (Figure 2.1). It should be noticed that the scattered light is in random directions and is different from the direction of incident light.

Stokes Raman scattering and anti-Stokes Raman both provide useful information by revealing the shift of light frequency. In Stokes Raman scattering, incident photon (with the energy of $h\nu_0$) excites a molecule to a virtual energy state. After the scattering process, this molecule relaxes to a vibrational energy state rather than entering its original ground state. A scattered photon (with the energy of $h\nu_0 - h\nu_v$) with less energy than the incident photon, is emitted simultaneously. In anti-Stokes Raman scattering, the molecule is already in a vibrational energy state. As the incident photon strikes the molecule, it is excited to a virtual energy state. And then this molecule relaxes to the ground energy state, resulting in the emission of a photon with more energy (with the energy of $h\nu_0 + h\nu_v$) comparing to the incident photon. It is common that most molecules will be found in the ground energy state at ambient temperature, photons are much less likely to be anti-Stokes scattered. Thus, only the Stokes Raman scattered photons are considered in most Raman measurements.

In conclusion, during the Raman scattering process, the inelastically scattered photons can be monitored and provide useful molecule band vibrational information.

2.1.2 Raman spectrum and Raman vibrations

A Raman spectrum is a vibrational spectrum. A typical Raman spectrum consists of bands, indicating the wavenumber position and signal amplitude of the Raman scattered photons. As described in Raman scattering theory, the Stokes Raman bands are red shifted from incident photons and with higher energy. On the other hand, the anti-Stokes Raman bands are blue shifted from incident photons, with a lower energy level.[17] The scattered photons from Rayleigh and Raman scattering (Stokes and anti-Stokes) processes are collected by a detector and finally presented in a computer as a figure indicating Raman signals. A schematic of a Raman spectrum is shown in Figure 2.2. Normally, the intense Rayleigh lines are filtered out before the detector. It can be seen that Stokes and anti-Stokes Raman bands are distributed symmetrically around Rayleigh lines, with a different energy.

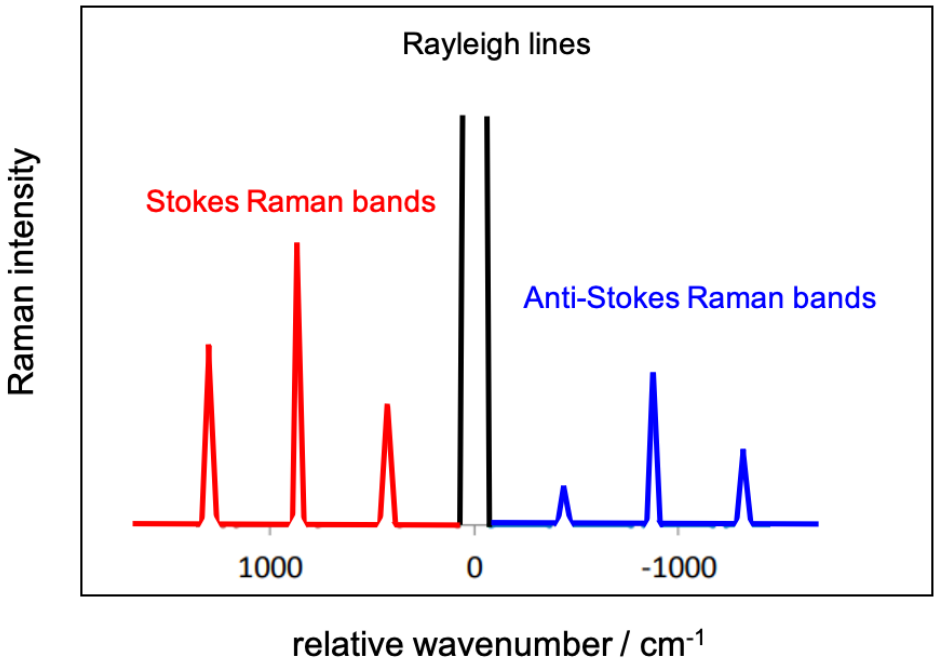

Figure 2.2 Schematic of a Raman spectrum. Strong Rayleigh lines and Raman bands (Stokes bands and anti-Stokes bands) are presented.

In the spectrum, each band is corresponding to a specific Raman vibration. The spectrum is recorded as relative wavenumber in Figure 2.2, corresponding to the frequency shift between scattered photon and incident photon. Normally, this shift is referred to as Raman shift, described in units of wavenumber (cm^{-1}). It is clear that Stokes Raman bands locate at positive wavenumber

range, while anti-Stokes Raman bands locate at the negative range. Thus, the vibrational information provided by the Raman spectrum is a unique fingerprint message for molecule constituents. Basing on this specific spectral information, substances can be detected and identified.

In a Raman spectrum, not all molecule vibrations are visible, because not all vibrations are Raman active. Molecule vibrations can give rise to a change either in dipole moment (μ) or in polarizability α. Only the vibrations with a change in polarizability are Raman active. For example, vibrations in CO_2 molecule include three different functions, symmetric stretching vibration, bending and asymmetric stretching vibration as presented in Figure 2.3. Of these three vibrational modes, only symmetric stretching is Raman active. The other two modes are active in IR vibrational spectrum. It is to say the symmetric vibration is Raman active.

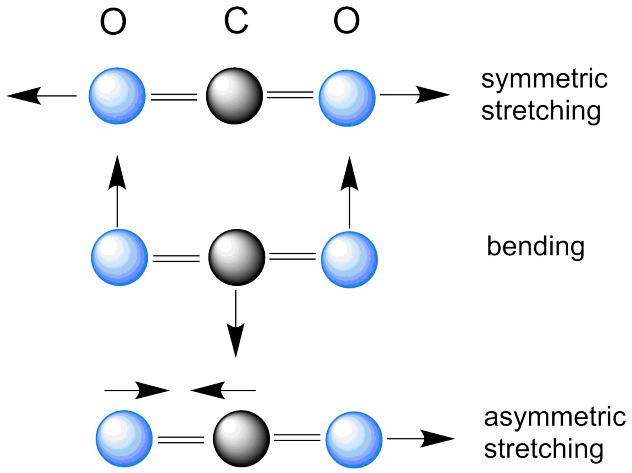

Figure 2.3 Vibrational modes of CO_2. [21]

2.2 Stable isotopic labeling

Stable isotopic labeling (SIL) is a powerful technique that enables tracking an isotope conduction process in a chemical reaction or in a metabolic process. Strictly speaking, stable isotope refers to isotope that does not or unlikely to undergo radioactive decay. In metabolic studies, 'stable isotope' is often used to refer to the stable isotope with relatively low natural abundance. For example, ^{1}H and ^{2}H are stable isotopes for hydrogen, ^{2}H (deuterium) is the stable isotope with a minor natural abundance of 0.02%. The commonly used stable isotopes are ^{13}C, ^{15}N, ^{2}H (D). The chemical compounds consisting of these stable isotopes, have stable physical and chemical properties and are normally used to introduce isotopes into a dynamic system.

2.2.1 Stable isotopic labeling in nuclear magnetic resonance and mass spectroscopy

The SIL technique has been widely used in the study of microbial ecology, allowing for the identification of organisms,[3,5-7] investigation of metabolic fluxes and metabolic pathways[22-25] within complex microbial communities. A typical example for the study of metabolic pathway using stable isotope labeling technique is presented in Figure 2.4. Stable isotope tracers ^{13}C-labeled glucose ($^{13}C_6$-Glc) or ^{13}C, ^{15}N-labeled glutamine ($^{13}C_5$, $^{15}N_2$-Gln) were fed to the cells, tissues or organisms, the biological systems were allowed to grow utilizing these labeled chemicals at a certain period. Related metabolites were extracted and characterized by nuclear magnetic resonance (NMR)[22] and mass spectroscopy (MS)[23-25]. MS and NMR allow discrimination and quantify the stable isotope enriched products from their gyromagnetic ratio and mass, respectively. For the NMR and MS measurements, they are bulk technique providing average biomolecules information. Thus, they are unable to offer cell heterogeneity information. In addition, these techniques demand complex sample preparation steps. They are also time-consuming and cost-effective.

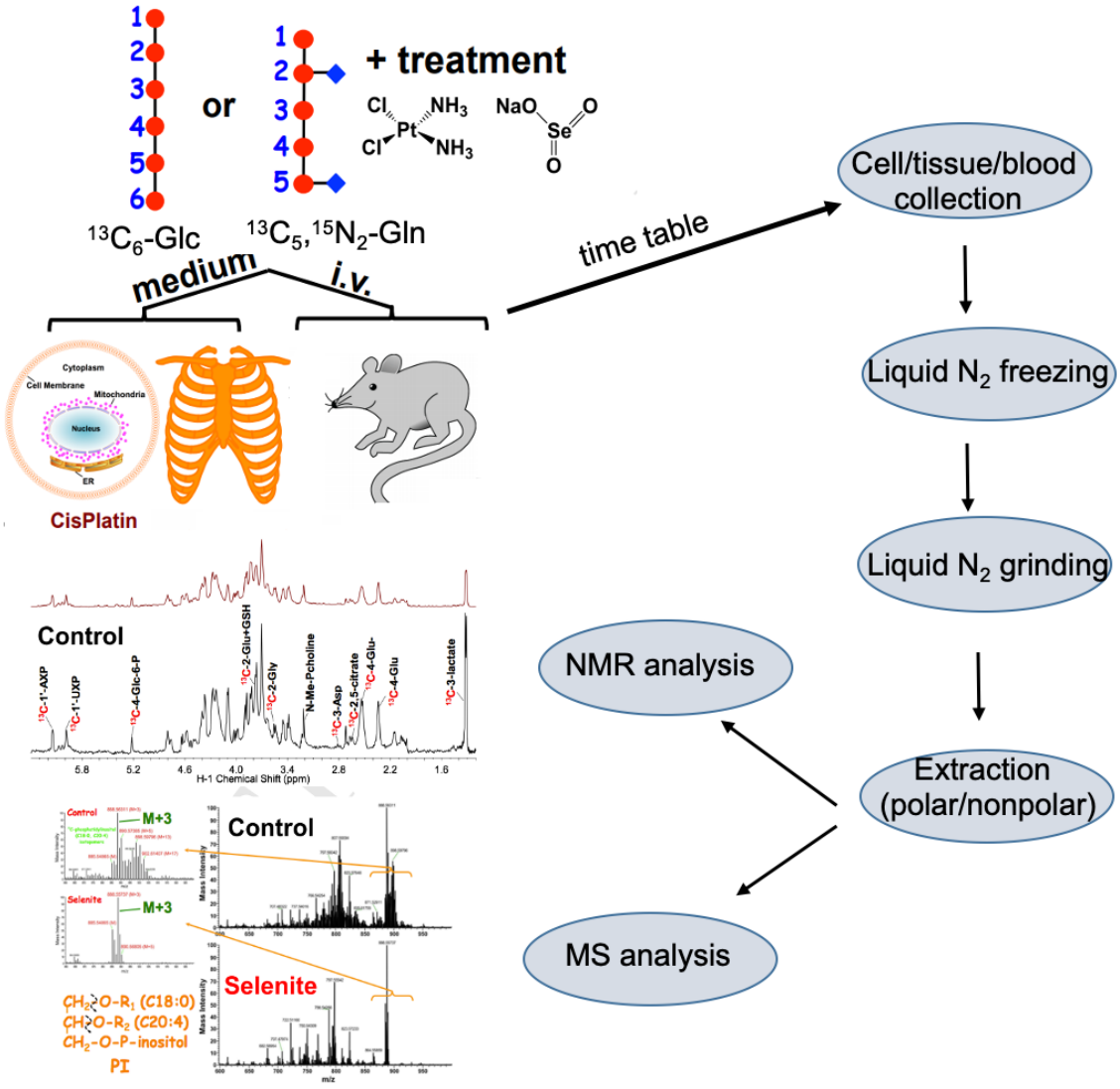

Figure 2.4 A schematic diagram of stable isotopic labeling to resolve metabolism pathways. In the diagram stable isotope tracers $^{13}C_6$-Glc or $^{13}C_5$, $^{15}N_2$-Gln were added to the culture medium as nutrition for cells, tissues, and organisms. The tracers can be metabolized by cells, tissue and organisms. After the tracer incubation for a certain time, targets were collected, and metabolites were finally extracted. The polar metabolites were characterized by NMR, and nonpolar metabolites were characterized by MS. Figure reproduced with permission from Ref.[23]

2.2.2 Stable isotopic labeling in Raman spectroscopy (SIL-Raman)

SIL-Raman theory

Raman spectra describe the chemical fingerprint and report vibrational modes of a molecule or system. It is easy to understand molecule band vibration by assuming a chemical bond as mathematical points held together by a massless spring.[26, 27] The spring here represents the

chemical bond between two atoms. In this case, the frequency of vibrational bond ($\tilde{\nu}, cm^{-1}$) is described by eq. 2.

$$\tilde{\nu} = \frac{1}{2\pi c}\sqrt{\frac{k}{\mu}} \qquad \text{eq. 2}$$

In eq. 2, c is the speed of light ($m \cdot s^{-1}$), k is the force constant of a diatomic bond ($N \cdot m^{-1}$) and μ is the reduced mass (kg) given by eq. 3.

$$\mu = \frac{m_1 \cdot m_2}{m_1 + m_2} \qquad \text{eq. 3}$$

In eq. 3, m_1 and m_2 are the masses of atoms. When one of the atoms is replaced by its heavier isotope, the reduced mass μ is increased and the corresponding frequency $\tilde{\nu}$ shifts to a smaller wavenumber position.

SIL-Raman applications

Currently, stable isotope labeling is used in combination with Raman microscopy for the characterization of an organism's metabolic process due to the easy sample preparation and low price of Raman microscopy. To date, most studies using SIL combined with different Raman scattering techniques (SIL-Raman) have focused on the application of ^{13}C, ^{15}N, D.[28-32] In SIL-Raman, Compared to the spectra of organism cultivated in unlabeled substrate, the shift of isotope dependent Raman bands appears in the spectra of the organism cultivated in labeled substrate. The appearance of these bands is used to indicate the isotope incorporation after incubation in isotope labeled substrate.

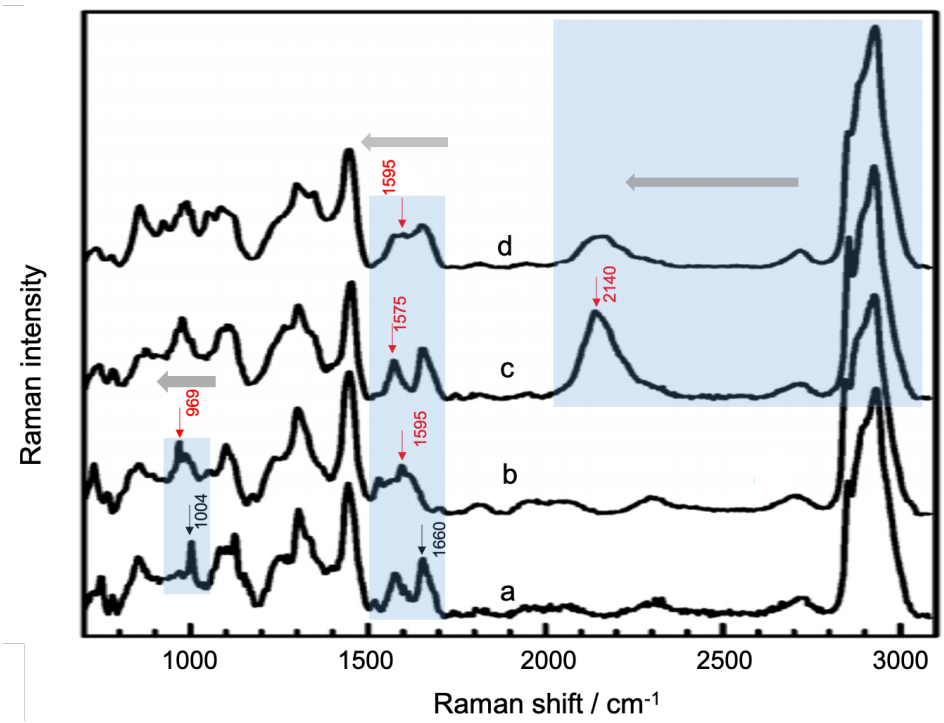

Figure 2.5. Mean Raman spectra of *Rhodococcus opacus* bacterial cell: normal spectra without any isotopic labeling (a), isotopic labeled with ^{13}C-glucose (b), isotopic labeled with D-glucose (c), isotopic labeled with both ^{13}C-glucose and D-glucose (d). Figure reproduced with permission from Ref.[26]

A typical example of *Rhodococcus opacus* investigation is shown in Figure 2.5. The Raman bands at 1004 and 1660 cm^{-1} (Figure 2.5a), corresponding to phenylalanine ring breathing and amide I vibration of polypeptide backbone, are shifted to 969 and 1595 cm^{-1} (Figure 2.5b) in ^{13}C-glucose-labeled bacteria spectra. The Raman spectra of D-glucose-labeled bacteria also features a large redshift from 2800-3038 cm^{-1} C-H vibrational region to 1950-2300 cm^{-1} C-D vibrational region (Figure 2.5c-d). The redshift from D labeling is larger than the minor redshifts from ^{13}C and ^{14}N labeling. It is due to comparably high reduced mass μ change. Since the atomic mass of D is twice that of H, μ is almost doubled resulting in a wider redshift from C-H to C-D vibrational region. Thus, the track of deuterium isotope in organism is easier to be observed in Raman spectra. Recently, labeling with deuterium involved isotope substrates has attracted increasing attention in the study of metabolic activity of various organisms. It should be noted that the Raman band shift occurs only when isotopes actually bind to individual molecules, within microorganisms. Depending on the type of isotope-labeled substrates and metabolic pathways expressed in the analyzed organism, different isotope-labeled substrates cause different Raman band redshifts which are listed in Table 2.1.

Table 2.1 Raman bands shifted due to different isotope-labeled subatrates.[5, 10, 26, 30, 33-36]

Raman bands of unlabeled cells / cm^{-1}	Isotope-labeled substrate	Raman bands of labeled cells / cm^{-1}	Raman bands assignment
1003.01	$^{13}C_6$-glucose	966.36	Phenylalanine ring breath
1001	^{13}C-naphthalene	990, 978, 968	phenylalanine with 2, 4, or 6 ^{13}C atoms in the aromatic ring breath
1128	^{13}C-acetate	1123	C-N stretching
1311	^{13}C-acetate	1307	C-H bending
1583	^{13}C-acetate	1577	C-C antisymmetric stretching
787	^{15}N-NH_4Cl	783	O-P-O breathing of cytosine or uracil
1174	^{15}N-NH_4Cl	1164	C-H in plane bending of tyrosine or phenylalanine
1578	^{15}N-NH_4Cl	1571	Ring stretching of guanine or adenine
2845	[D_7] -glucose	2142	C-H_2 in lipid
2845-2940	[D_7] -glucose	2192	C-H_3 in protein
1001	D-acetate	988, 975, 960	Deuterated phenylalanine ring breathing (part and fully deuterated)
1006	D_2O	994	Phenylalanine aromatic ring stretching
1126	D_2O	1104	lipids
2800-3100	D_2O	2040-2300	C-H vibration

SIL-Raman using different ^{13}C, ^{15}N, D labeled substrates can effectively be applied for direct observation of functional properties of individual microorganisms. The incorporation of ^{13}C and ^{15}N SIL is normally combined with enhanced signal techniques, such as surface-enhanced Raman

scattering (SERS) due to their minor redshifts (Table 2.1). Isotope-labeled substrate D_2O has come into use recently due to its sufficient sensitivity to unravel general metabolic activity without cell reproduction. In addition, because D_2O is a non-carbon tracer can be freely diffuse into microorganisms. Moreover, D_2O is a cost-effective substance for SIL investigation of microbial community metabolic activity while many other commercially substrates are extremely expensive or some are not even commercially available. Also, the D_2O within 50% has no significant effect on the growth of many microbial strains.

2.3 Bacterial Raman microscopy combined with D_2O labeling

2.3.1 Basics of D_2O labeling-Raman microscopy

Water (H_2O) is a universal solvent in living organisms. It participates in most biochemical reactions. For example, in all known lipid biosynthetic pathways, hydrogen from water is involved in the reduction step of the fatty acid synthesis. Moreover, in the overall metabolic activity of microbial cells, the electron carrier nicotinamide adenine dinucleotide phosphate (NADPH) and nicotinamide adenine dinucleotide (NADH) can form C-D bonds via NADPH + H^+ reaction using deuterium.

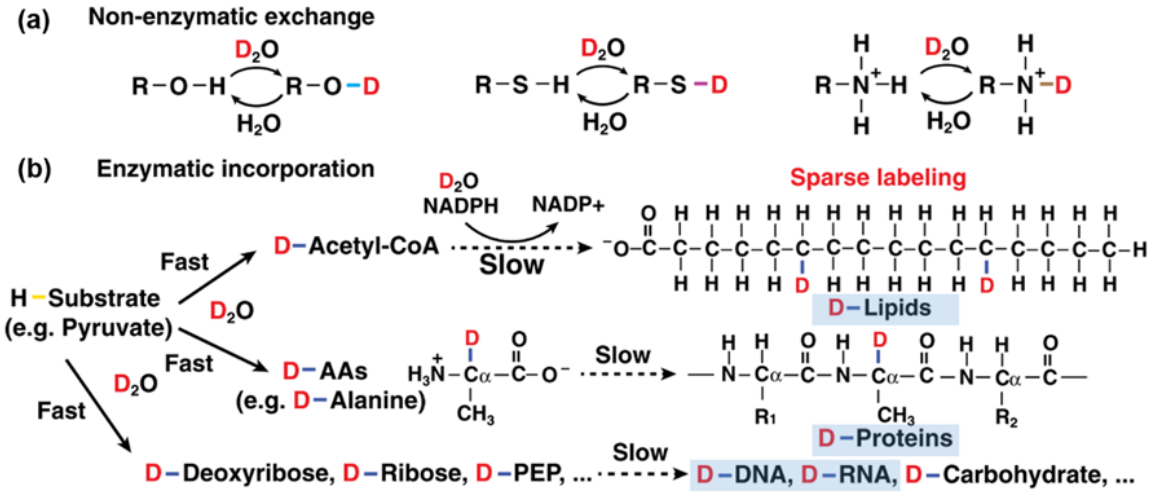

Figure 2.6 Biochemical synthetic incorporation of D from D_2O into macromolecules in living organisms via non-enzymatic exchange (a), and enzymatic incorporation (b). Figure reproduced with permission from Ref.[4]

It is shown in Figure 2.6 that the incorporation of a stable isotope D from water into living organisms can induce obvious Raman bands shifts due to the substitution of ^{1}H (H) with D in chemical components by forming a variety of X-D bonds via non-enzymatic H / D exchange and enzymatic incorporation. The formation of O-D, N-D and S-D bonds on existing molecules via non-enzymatic H / D exchange is spontaneous and reversable, while the enzymatic incorporation to form newly synthesized microbial macromolecules such as proteins, lipids, and DNA is irreversible and slow. Therefore, in D_2O based SIL-Raman (D_2O-Raman), the redshifts caused by the gradual substitution of C-H by C-D bonds in microbial macromolecules can be tracked to monitor the microbial cells activity. The new Raman band of C-D stretching vibration can be observed in the silent Raman spectral region of 1950 to 2300 cm^{-1}. For example, it can be seen in Figure 2.7 that the Raman spectra of *Mycobacterium smegmatis* (*M. smegmatis*) cultivated in D_2O labeled medium for 270 min has an extra Raman band around 1950-2300 cm^{-1}, compared to the Raman spectra that without cultivation in D_2O labeled medium (0 min).

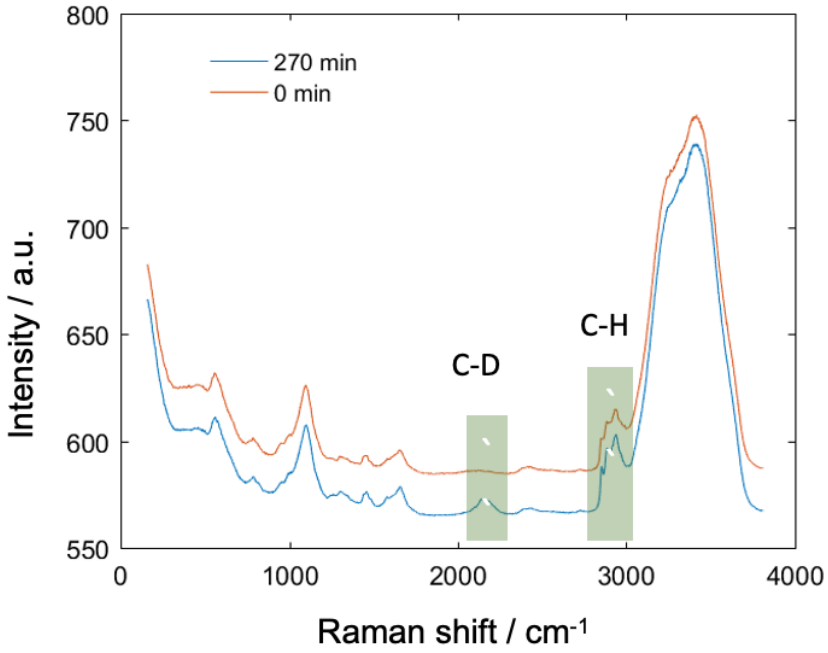

Figure 2.7. Raman spectra of wild type *M. smegmatis* incorporated with D_2O labeled medium for 0 min (red line, control measurement) and 270 min (blue line).

According to the enzymatic incorporation (see Figure 2.6), biochemical precursors of macromolecules can be labeled by deuterium from D_2O, while the precursors are slowly incorporated into macromolecules. The incorporation is governed by cellular metabolic activities.

Thus, a new Raman band for *M. smegmatis* assigned to the C-D vibration is involves following bacterial metabolic. The ratio C-D/C-H can be used as a quantitative indicator of the metabolic activity of individual cells. Thus, D_2O-Raman can provide straightforward and quantitative information on microbial metabolic activities.

2.3.2 Applications

In most cases, D_2O-labeled SIL-approaches have been combined with various Raman scattering techniques for purposes, such as D_2O labeling combined with stimulated Raman microscopy imaging for metabolic activities tracking in animals,[4] D_2O labeling combined with single-cell Raman microscopy for inorganic- and organic-phosphate-solubilizing bacteria investigation in a culture-independent way,[5] and D_2O labeling combined with single-cell Raman microscopy for rapid antibiotic susceptibility testing in clinical samples.[6]

In 2015, D_2O-Raman was initially used to identify active microbial cells in a complex matrix. It is a culture-independent analytical technique that incorporates deuterium into bacterial cells during all known reduction steps of fatty acid synthesis allows the identification of active fast-growing bacteria within 20 min, based on the newly appearing C-D Raman band at 2040-2300 cm^{-1}. The addition of D_2O in combination with different unlabeled substrates is used to study the responses of microbes to different nutrients on single-cell level. It has also proved that this method is a universally applicable technique that has been proved by cultivating various bacterial strains in D_2O. D_2O-Raman does not require cell division for labeling, and it is faster than some other SIL technique such as DNA-SIL.[3]

In metabolic interaction studies of a two-species community (consisting of *Acinetobacter baylyi* ADP1 and *Escherichia coli*), D_2O-Raman coupled with ^{13}C-reverse was applied. This co-labeling technique is useful to probe any carbon substrates' metabolism. In the ^{13}C-reverse labeling process, bacterial cells were initially ^{13}C-labeled by ^{13}C-glucose. It is known that D_2O-Raman can be used to sensitively and reliably identify metabolically active microbial cells but not quiescent cells. Thus, active cells can gradually metabolize ^{12}C substrate where cells were reversed to ^{12}C cells with the appearance of the C-D band. However, those inactive cells cannot metabolize this ^{12}C carbon substrate without C-H band shifting. The reverse isotope labeling is a good tool when stable isotopic substrates are not available or super expensive.[36]

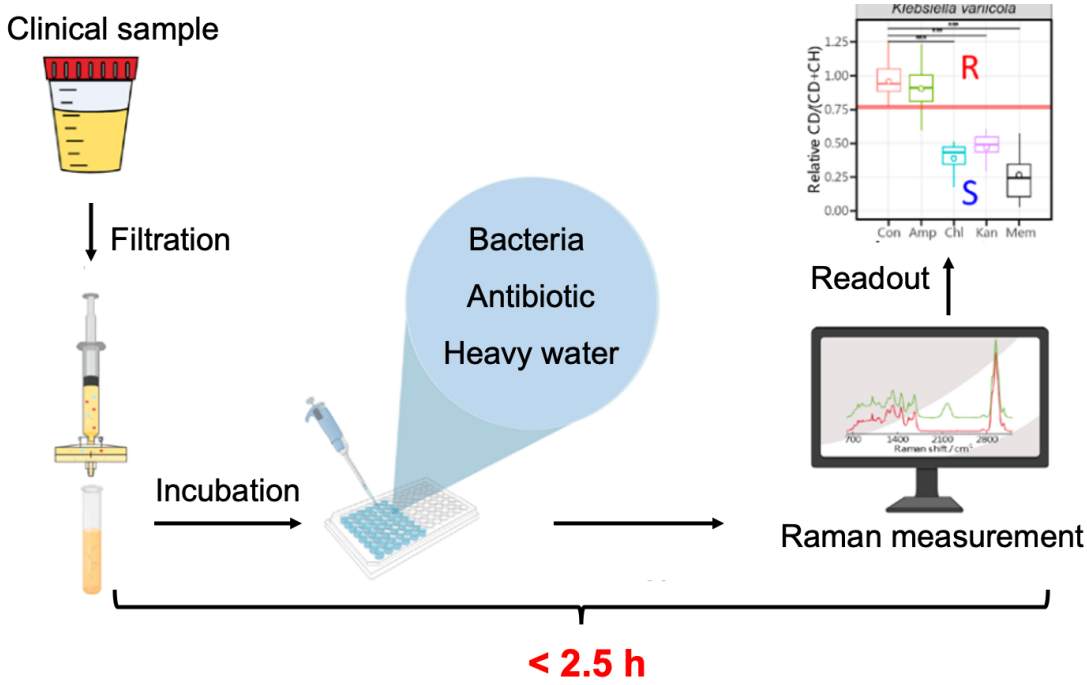

Figure 2.8 A standard workflow for antibiotic susceptibility testing (AST) toward clinical urine samples. Figure reproduced with permission from Ref.[6]

Similarly, the D_2O Raman is applicable for characterizing the presence and activity of phosphate solubilizing bacteria (PBS) in complex soil communities.[5] D_2O-Raman is also suitable for investigation of cellular metabolic activity in response to antibiotic treatment (NaF, chlorhexidine, and ampicillin) based on the redshift of the C-H band vibrations. The observation of the new Raman band in 2040-2300 cm^{-1} caused by C-D vibrations is used as a universal biomarker. As a result, using this technique, the antibiotic susceptible and resistant *Streptococcus mutans* strains can be discriminated in 0.5 h.[7] The D_2O-Raman has proven to be reliable and rapid for clinical applications. A standard workflow (Figure 2.8) has been successfully developed for antibiotic susceptibility testing (AST) toward clinical urine samples in 2.5 h.[6] With this, the antibiotic susceptible and resistant clinical samples can be identified.

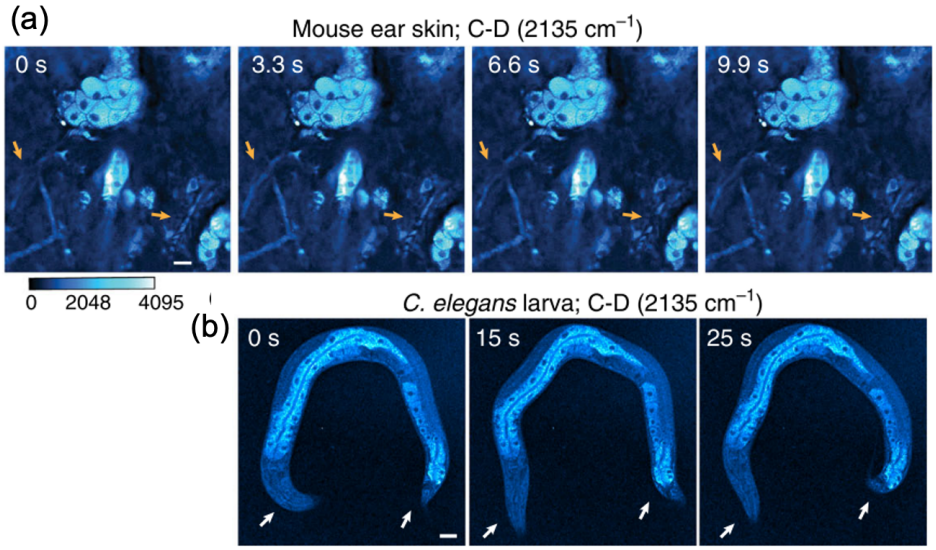

Figure 2.9 SRS microscopic imaging recordings of incorporation of deuterium from D_2O in living cells and animals. (a) Sebocytes in living mouse ear skin and (b) *Caenorhabditis elegans* (*C. elegans*) larva growing in 25% and 20% D_2O, respectively. The orange and white arrows are corresponding to blood flow in mouse and the movement of the *C. elegans* body. Scale bar is 20 µm. Figure reproduced with permission from Ref.[4]

The above applications are suitable for single-point measurements with long integration time at the single-cell level. D_2O-Raman is also applicable to imaging metabolic dynamics. In the case of SIL-Raman imaging of the metabolism in microbial cells, high spatial and temporal resolution are required for fast detection. It takes few milliseconds per pixel for a full window (3000 cm^{-1}) spectrum of spontaneous Raman scattering that is slower than stimulated Raman scattering (SRS). For SRS, a spectrum can be acquired in microseconds, covering a window of hundred wavenumbers.[37] Thus, SRS combined with D_2O labeling (D_2O-SRS) was developed for high-speed and sensitive vibrational spectroscopic imaging in studies of cell metabolic activity. For example, D_2O-SRS was already introduced to image macromolecule metabolism in living cells and animals (Figure 2.9). Based on the generation of C-D bonds from enzymatic incorporation of D_2O contained deuterium into biosynthesized macromolecules, the biosynthesis in animal tissues can be tracked and imaged by SRS. Moreover, an unmixing method was developed to identify lipid-, protein-, and DNA- specific Raman shifts, which can visualize their different metabolisms (Figure 2.10).[4, 38] Although D_2O-SRS is suitable for metabolic activity observation, the equipment is not applicable in each research group. Very recently, D_2O-Raman microscopic imaging has been

used to investigate the metabolic activities of bacterial persister cells.[8] They did not delve into investigating the harmful bacterial strain *Mycobacterium tuberculosis* (*M. Tuberculosis)*.

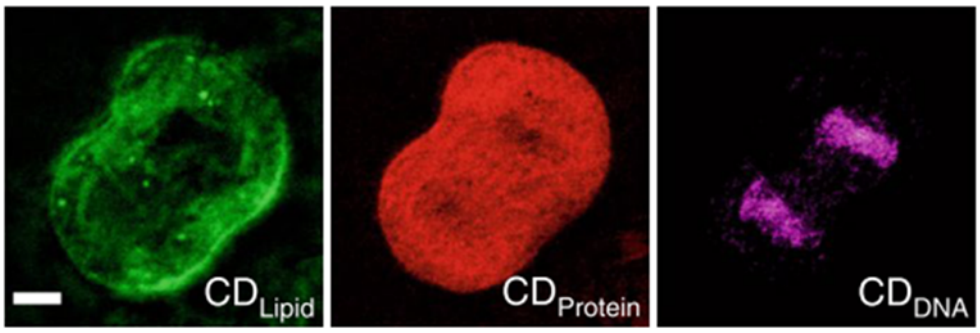

Figure 2.10 SRS microscopic imaging of deuterium-labeled lipids (CD_{Lipid}), proteins ($CD_{Protein}$) and DNA (CD_{DNA}) by spectral unmixing method. Scale bar is 10 μm. Figure reproduced with permission from Ref.[39]

The above literature survey shows that D_2O-Raman is very effective in organism metabolism research. However, it is limited in the application of single bacterial cell imaging. There is only one paper on the application of single-cell D_2O-Raman microscopic imaging.[8] Actually, they do not clearly show the results of microscopic imaging. Straightforward information extraction from Raman images should be studied carefully.

In this thesis, deuterium incorporation from D_2O into bacterial was investigated by a Raman imaging-based method. Within one bacterial doubling time, a new C-D bond, which can easily be distinguished from the original Raman spectra (no incorporation with D_2O) appeared in bacterial Raman spectra. Therefore, the Raman spectral tracing of deuterium isotope can be performed by monitoring C-D bond. Using confocal Raman microscopy, a high-resolution imaging technique, the intracellular and extracellular heterogeneity are observed by tracing bacterial D_2O metabolism. The fast-growing *M. smegmatis* and harmful *M. Tuberculosis* were studied.

Appling the Raman imaging-based method, the effects of different antibiotics on *M. smegmatis* and *M. Tuberculosis* were also studied in single-cell resolution. Different modes of action were observed.

2.4 Surface Enhanced Raman Scattering (SERS)

The weak signal intensity of normal Raman spectrum limits the application of Raman microscopy. It is because most molecules have a very small Raman cross section. In the 1970s, SERS was

initially discovered, as it was found that small organic molecules (pyridine) adsorbed onto the surface of a roughed silver electrode exhibit enhanced Raman intensities (enhancement of 10^6).[40] Afterwards, people started to use SERS to detect low concentration molecules on nanostructured metal surfaces. Even single molecules can be detected by this technique.[41] Since then, SERS has been widely used in electrochemical catalytic reactions,[42] biological and chemical sensors,[43] trace detection, imaging,[44] and biochemical analysis. SERS has been developed experimentally and theoretically. The effects of surface morphology and electronic structure, interaction of light and rough surface, molecule orientation on the surface, surrounding environment of molecules and surfaces, incident light intensity, frequency, degree of polarization and polarization direction on the SERS spectrum are quite complex. These complexities of the SERS system lead to a diversity of SERS perceptions. Different mechanisms have been proposed from various directions and specific experimental conditions. The mechanism responsible for the SERS enhancement effect is still controversial.

At present, there are two major SERS enhancement mechanisms generally accepted by the community. There is an electromagnetic enhancement mechanism and a chemical enhancement mechanism.[45-47] The SERS signal intensity (I_{SERS}) has the following relationship.[47]

$$I_{SERS} \propto [|\vec{E}(\omega_0)|^2 |\vec{E}(\omega_s)|^2] \sum_{\rho,\sigma} \left|(\alpha_\rho, \sigma)_{fi}\right|^2 \qquad \text{eq. 4}$$

In the eq.4 , $\vec{E}(\omega_0)$ and $\vec{E}(\omega_s)$ are the surface localized electric field intensity with the frequency of ω_0 and the surface localized scattered light field intensity with frequency of ω_s, respectively. It is obvious from eq. 4 that a higher intensity of the local electric field of incident and scattered light leads to a higher Raman signal intensity, which contributes to physical enhancement, normally addressed as an electromagnetic enhancement (EME). The ρ and σ are parameters are related to the electric field of the excitation light and Raman scattered light, respectively. The term $(\alpha_\rho, \sigma)_{fi}$ is related to the optical polarizability of the molecule. The sum of $(\alpha_\rho, \sigma)_{fi}$ indicates that larger polarizability yields larger corresponding SERS signal, this is the contribution of SERS chemical enhancement (CE), as a result of chemical interaction between SERS substrate surface and molecule.

2.4.1 Electromagnetic enhancement

In the enhancement of Raman signal, EME is considered to present the majority of the contributions, it has a higher enhancement factor (EF) than CE. The electromagnetic enhancement factor can reach values as high as 10^{10} to 10^{11} by electrodynamics calculations which is much higher than 10^3 in CE.[48] It is commonly believed that the localized surface plasma resonance (LSPR) of plasmonic NPs dominates the EME. The schematic diagram of LSPR is shown in Figure 2.11. The collective oscillation of free conduction electrons (in the metal sphere) can be produced due to the strong coupling with incident light of specific wavelength (electric field in Figure 2.11).

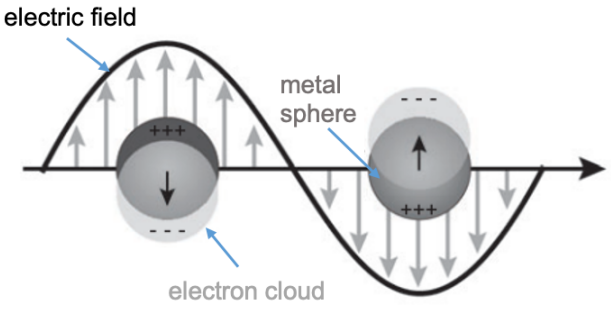

Figure 2.11 Schematic diagram of the localized surface plasmon resonance effect.[45]

In general, when the rough surface of plasmonic nanostructure is stimulated by an incident laser at a certain wavelength, the LSPR of plasmonic nanostructure causes great amplification of the electric field.[49] Thus, an enhanced Raman scattering signal can be obtained from the molecules adsorbed on the surface of plasmonic nanostructure. As described in eq.4, the enhancement from EME is determined by the intensity of the local electric field of incident and scattered light (item of $|\vec{E}(\omega_0)|^2|\vec{E}(\omega_s)|^2$ in eq. 4). In some cases where the surface plasmon width is larger than the Stokes shift, $\vec{E}(\omega_0)$ is assumed the same as $\vec{E}(\omega_s)$. Hence, the SERS intensity (I_{SERS}) can be described as $I_{SERS} \propto |E|^4$.[50-52] This is the widely used $|E|^4$ approximation. In most applications, results produced from the $|E|^4$ expression are useful to evaluate the order of magnitude of EF. This relationship clearly indicates that even a small change in the electromagnetic field makes a great change on I_{SERS}.

LSPR is a specific optical property of noble metal NPs and nanostructures. Only few metals can produce LSPR effect under laser excitation, such as noble metals (Ag, Au and Cu) and free electron

metals (alkali metals) with nanoscale features. The LSPR of NPs is generally related to the NPs size, morphology, arrangement and surrounding environment.[53,54] Therefore, attempts have been made to search the maximum EME in Raman signal enhancement by tuning the NPs shape[48] and arrangement[54]. For example, for Au nanosphere dimer, the SERS EF increases, when the gap size of the dimer is reduced from 10 to 2 nm.[54] In addition, the frequency of incident laser is also considered to be a key element to achieve high enhancement. It is reported that better signal enhancement can be obtained when the frequency of incident laser is matched to the LSPR of plasmonic NPs.[55] Above all, the theoretical mechanism studies of SERS EME provides useful principles to design effective SERS substrates.

2.4.2 Chemical enhancement

In contrast to the EME, chemical enhancement (CE) demands the target molecules to be close enough to metallic substrate surface. When the molecule binds chemically to the metal surface, the EF is particularly large. Signal enhancement caused by CE is about one to three orders of magnitude, which is much smaller than EME contribution. Theoretically, when studying the interaction between para- and meta- substituted pyridine and Ag clusters, the enhancement coming from CE can be as high as 10^3.[56] It is much smaller than 10^{10} in EEM enhancement. And, unlike the long-range effect of EME, the CE is a short-range effect that is usually thought to be a 'first-layer-effect'.[57, 58] The CE is often related to electrons transfer between the SERS substrate and the adsorbed molecule under laser radiation. A resonance effect can be caused by the electronic transition between the metallic SERS substrate and the adsorbed molecule lowest unoccupied energy level (LUMO).

From a theoretical point of view, three different types of enhancement mechanisms can be identified in CE (Figure 2.12): (a) ground state chemical enhancement, which arises basing on ground state interaction between SERS substrate and molecules; (b) the resonance Raman enhancement comes from resonance between the excitation wavelength and molecular transition; (c) charge transfer resonance enhancement occurs from the excitation wavelength being resonant with charge transfer (CT) transition between the metal NPs and the absorbed molecules. The relative importance of these enhancements is difficult to determine experimentally, as they can be separated and stuied only under certain specific constraints. These three possible chemical enhancement effects are all related to the adsorbed molecules, as they reflect the chemical

interaction between absorbed molecules and SERS substrate.[59-61] The chemical enhancement effects were systematically studied by Valley and his coworkers[62] by caculating and comparing the CE EF values for a number of substituted benzene thiolates absorbed on Ag and Au cluster substrates. It has been shown that CE is moleculer specific.

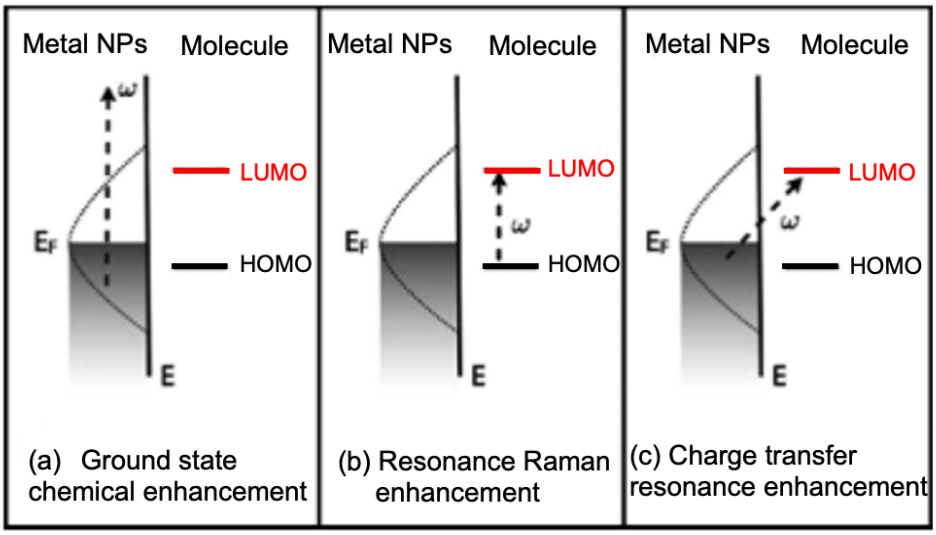

Figure 2.12 Schematic diagram of different types chemical enhancement. (a) Ground state chemical enhancement; (b) resonance Raman enhancement; (c) charge transfer resonance enhancement. Figure reproduced with permission from Ref.[63]

It is important to realize that all the enhancement mechanisms are difficult to be isolate and studied experimentally. Therefore, it is difficult to determine which is more important. The CE mostly depends on the strong interaction between the molecule and SERS the substrate surface, while the EME can be applid to explain weak interaction with a long-range effect. In all, researchers generally believe that the EME plays a major role, and CM also has a certain contribution. The two together constitute in the final enhancement of SERS signal. However, researchers are still struggling to find a unified theory for SERS enhancement mechanism.[64]

2.4.3 SERS active substrates

An ideal SERS substrate should be chemically stable and be able to be prepared reproducibly in large scale at low cost. Importantly, the substrate should exhibit a high EF. The quality of the SERS substrates is critical to the success of any SERS experiment. It has been reported that high enhancement can be obtained at the nanogap of adjacent NPs or very sharp tips of single NP,[65-68]

which are normally named ‘hot spots’. Over the last few decades, researchers have been working hard to prepare SERS active substrates with a well-controlled structure. Generally, substrates based on gold (Au) and silver (Ag) are the most widely used due to their high EF and unique LSPR optical properties in the visible to near infrared (NIR) range.[69-71] Generally, SERS substrates can be used either in the form of colloid or in the state of solid. Up to now, SERS substrates have gone through various fabrication methods which are presented in Table 2.2. The detail of theses substrates will be discussed later.

Table 2.2 Different SERS substrates and their corresponding fabrication methods and applications.

Substrate	Method	Application	
AgNPs suspension	Wet chemical	Single crystal violet molecule detection	[72]
AgNPs clusters in suspension	Wet chemical	Deep study of optical interaction between NPs	[73]
Ag superstructures in suspension	Wet chemical	Investigation of hot electron induced reduction	[74]
AuNP dimers	A solid phase approach	Synthesis various sized AuNP dimers	
Ag film on Si substrate	Electron-beam lithography and electroless deposition	Detection of Rhodamanine 6G (10^{-20} M)	[76]
NP-polymer film	Liquid-liquid film transfer	Organic molecule and bacteria detection	
highly ordered MNPs (Au, Pt)	Talbot lithography combined with ion-beam etching	Gas-phase catalysis study	[78]
AuNR arrays	Focused ion beam lithography	Distinguish cyanuric acid in milk	
Au nanobipyramids (AuNBPs)	AAO template assisted drop-and-dry-method	Determination of dopamine in spiked human serum	[80]
AuNP clusters	AAO template assisted AuNPs self-assembly	Investigation of plasmon-driven photocatalysis of 4-NTP reduction	[81]

Among various kinds of SERS active substrates, the metallic colloid is the simplest one, normally prepared by a cost-effective wet chemical method. Wet chemical method synthesis of SERS active

colloids is often prepared directly by reduction of an Ag or Au precursor salt in a liquid medium. The NPs size and shape can be tuned to the desired optical properties in suspension, which makes the colloid available for different conditions. The size of the NPs can be controlled by using different reducing agents, and the shape of NPs can be adjusted by adding different surfactants during synthesis. For colloidal SERS substrates, plenty of SERS hot spots can be easily achieved by using salt (such as NaCl, KCl) to cause NPs aggregation or clustering in suspension.[82, 83] This kind of substrate still exhibits a high Raman EF. For example, single crystal violet molecule was able to be detected with an EF of 10^{14}-10^{15} in a colloidal silver solution.[72] It should be noted that the surface field and resonance enhancement EF $\approx 10^{15}$. However, reproducibility and quantitative analysis are a great challenge, when metal nanoparticles (MNPs) in the colloidal state are applied for real analytical samples. Addition of salt in NP suspension leads random arrangement of the NPs in aggregates. This aggregation is a dynamic process and the hot spots generated by the aggregation are randomly organized and cannot be controlled (Figure 2.13a). It is difficult to determine the right time for spectra acquisition and spectra collected at different points fluctuate a lot in intensity. In all, these limitations impede the identification of the exact structure of SERS hot spots and a depth study of the SERS mechanism. For reproducible and quantitative analysis, preparation of SERS substrates with controllable assembly is in high demand. Even this problem can be solved by directing NPs self-assembled as ordered layers or arrays (Figure 2.13b) around liquid-liquid (LL)[84] or liquid-air (LA) interfaces.[85] In my opinion, the metallic colloids are not the best choice for commercial purposes due to their limitations in long-term storage.

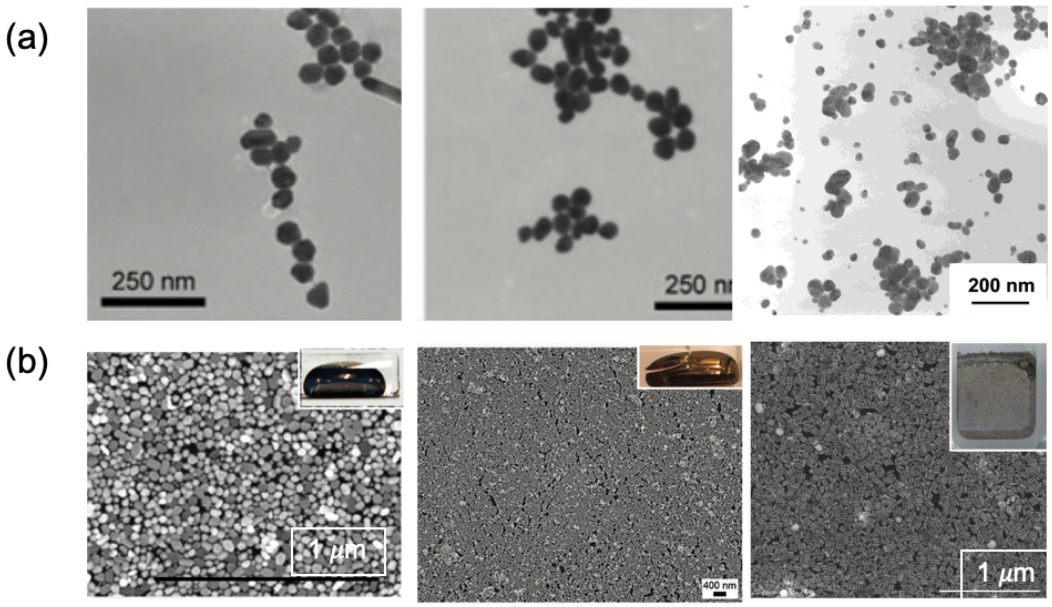

Figure 2.13 Examples of metallic colloid SERS substrates. SEM image of (a) random aggregated nanoparticles, (b) LL and LA assembly of SERS substrates. Figures reproduced with permission from Ref.[86-89]

For solid SERS substrates, the main interest is to obtain highly ordered solid SERS substrates, yielding reproducible and stable SERS results. In this case, adjacent NP gap size,[90] morphology,[91, 92] size[93] and material of NPs are important factors for SERS measurements. With the rapid development of nanofabrication technology, large-area uniformed substrates presenting good reproducibility for SERS measurements can be easily fabricated. Generally, solid SERS substrates can be prepared by immobilizing NPs on a solid support (glass, silica, etc.) or directly by manufacturing NPs on these solid supports. In the next section, I will briefly explain solid SERS substrates in three categories: (1) MNPs immobilized in planar solid supports; (2) nanolithographic techniques; (3) template-assisted techniques.

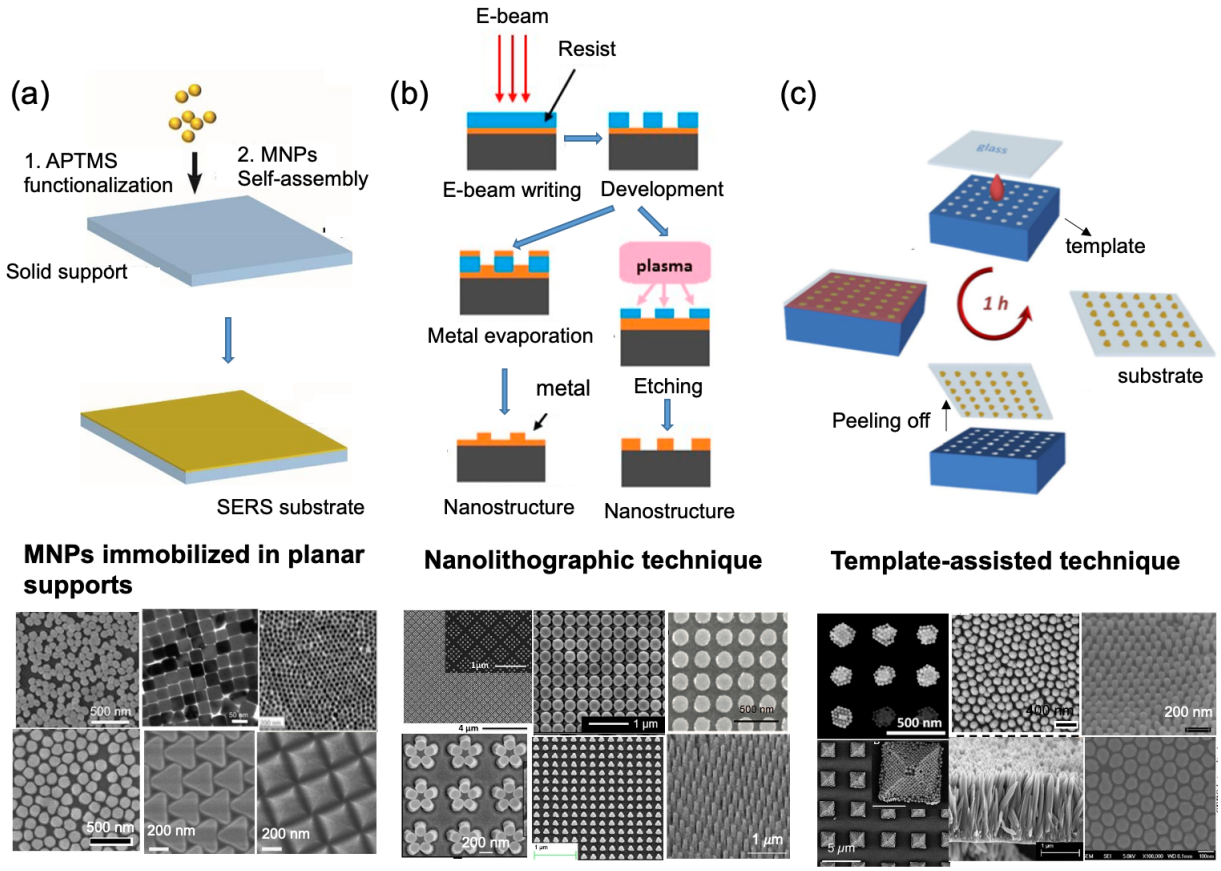

Figure 2.14 Examples of highly ordered solid SERS substrates prepared by different methods: (a) MNPs immobilized in planar solid supports, (b) nanolithographic methods and (c) template-assisted techniques. Figure reproduced with permission from Ref.[85, 94-110]

The first established method to obtain a solid SERS substrate was to immobilize MNPs onto polymer coated substrate.[111] Since then, solid SERS substrates have been reported based on similar methods including Langmuir-Blodgett, electrophoretic deposition, gel trapping, in-situ chemical growth of MNPs,[112] ect. Recently, SERS substrates fabricated based on liquid-liquid (LL) interface and liquid-air (LA) interface self-assembly technology has been widely investigated, in which a MNP array is pre-assembled on the interface and then transferred to a solid support. The typical procedure of MNPs immobilized on planar solid supports is presented in Figure 2.14a. It is shown that the solid supports were initially functionalized with some special molecules, such as (3-Aminopropyl) trimethoxysilane, or (3-Mercaptopropyl) trimethoxysilane to obtain naked thiol or amine groups. Thus, MNPs can be self-assembled on the solid substrates through covalent bonding due to the interaction between the functional groups and the MNPs surfaces. This self-assembly method is easy and cost effective for preparing solid SERS substrates.

With the increasing development of nanotechnologies, advanced nanofabrication process has been developed for well controlled SERS substrate preparation. Nanolithographic techniques, electron beam (E-beam) lithography, focused-ion beam (FI-beam) lithography and photon lithography techniques can be applied. In nanolithographic techniques, desired nanostructures can be produced by writing directly on a silicon or glass slide using an E-beam, FI-beam or photon which can then be used as molds for fabrication of desired SERS nanostructure. Figure 2.14b represents two typical processes based on E-beam lithography. Firstly, the desired nanostructured pattern is developed by E-beam writing. Then, metal lift-off and plasma etching can be used for final SERS substrates preparation. The main advantage of these techniques is to obtain exact geometric controlled nanostructures, which enables high reproducibility and sensitivity in SERS measurements. Furthermore, it is easy to tune the localized surface plasmon resonance (LSPR) that matches with the laser wavelength to obtain optimized SERS enhancement. Moreover, it is easy to fabricate 3D SERS substrates using lithography with high enhancement. However, due to the use of high-energy FI-beam or E-beam to fabricate large area SERS substrates, the nanolithographic techniques are time-consuming and expensive, which limits their practical applications.

Well-controlled SERS substrates can also be fabricated by template-assisted method. The template can be AAO, patterned PDMS stamp, carbon nanotubes, imprinted polymers, etc. A typical process for SERS substrates preparation based on a template-assisted technique can be seen in Figure 2.14c. In this technique, the specific pattern in the templates is the key element for the nanostructure. Huang et al.[107] have developed highly ordered and vertically aligned AgNRs as a large-scale array of SERS substrates using an AAO template-assisted method. The array can provide a large number of uniformly distributed sub-10 nm gaps between adjacent AgNRs. The details of nanofabrication of solid SERS substrates from 2009 to 2013 have been clearly reviewed by Luo et al.[113]

In all, solid SERS substrates are flexible for SERS quantitative applications and very convenient for in situ analysis. These advantages are expected to bring SERS technology closer to practical applications. Nowadays, how to fabricate large-area and uniform SERS active substrates with high density and controllable hotspots in a cost-effective and repeatable way remains the challenge in SERS applications. In this thesis, a simply prepared and cheap SERS substrate Ag plasmonic film

(AgPF) was developed. The AgPF can be used for stable observation of the photoreduction of 4-nitrothiophenol (4-NTP) to 4-aminothiophenol (4-ATP).

2.5 SERS applications in photocatalytic reaction

SERS is powerful technique that can be applied in the field of chemical species identification and trace detection,[80, 95, 114-117] discrimination of bacteria,[118-120] pharmaceuticals,[121] photocatalysis.[13, 122-125] Here, SERS applications in photocatalytic reaction observations are concentrated. The detection of photocatalytic reactions with SERS is mainly focused on model reactions. In recent years, reduction of 4-NTP to 4-ATP, catalyzed by MNPs, has been intensively studied as a model reaction using aqueous $NaBH_4$ solution or H_2 as strong chemical reducing agents. The 4-NTP and 4-ATP molecules can chemically bind to Au/Ag NPs surface with their thiol groups. This enables the SERS observation very easy. In addition, it has been found that molecules having a combination of a nitro or amino group and an aromatic ring have a relatively high Raman cross section and the reaction can be observed with a short acquisition time.

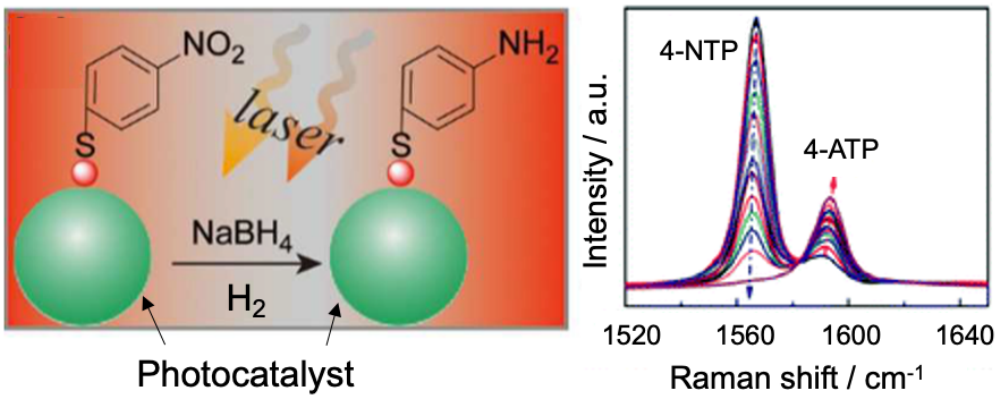

Figure 2.15 Representation of the photoreduction of 4-NTP to 4-ATP by $NaBH_4$ or H_2 on photocatalyst NPs surface. Figure reproduced with permission from Ref.[126]

The combination of SERS active plasmonic substrates and catalytically active MNPs has been widely used for experimental and theoretical SERS investigation of 4-NTP hydrogenation. For example, Au nanoclusters supported on a TiO_2 array (AuNCs/TiO_2 photonic array) was applied for SERS monitored reduction of 4-NTP using $NaBH_4$ as reducing agent. In this metal/semiconductor format nanostructure, the laser irradiation induced dimerization of 4-NTP was not observed. [124] Rodal-Cedeira et al. studied the reduction of 4-NTP to 4-ATP on Au@Pd

core-shell nanorods, and demonstrated excellent plasmonic properties of Au@Pd hybrid particles, enabling monitoring of the catalytic conversion by SERS spectroscopy also in a reducing agent $NaBH_4$.[127] In these studies, complex hybrid nanostructures are used, and chemical reducing agents ($NaBH_4$, H_2) are needed for the hydrogenation. Very recently, reduction of 4-NTP to 4-ATP in the presence of acid halide media, such as HCl, HBr and HI was demonstrated. As can be seen from Figure 2.16, this hot-electron-induced reduction only occurs in the presence of protons and halide ions.

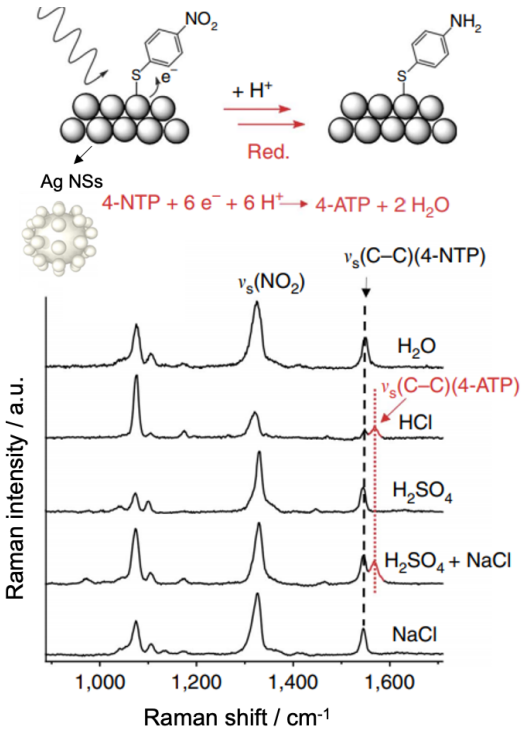

Figure 2.16 Six-electron, six-proton photocatalytic reduction of 4-NTP to 4-ATP. The bottom SERS spectra show the reduction in the presence of different reaction media. Figure reproduced with permission from Ref.[74]

Scheme 2.1 Schematic illustration of reaction pathway for reduction of aromatic nitro compounds to the corresponding aniline.[128]

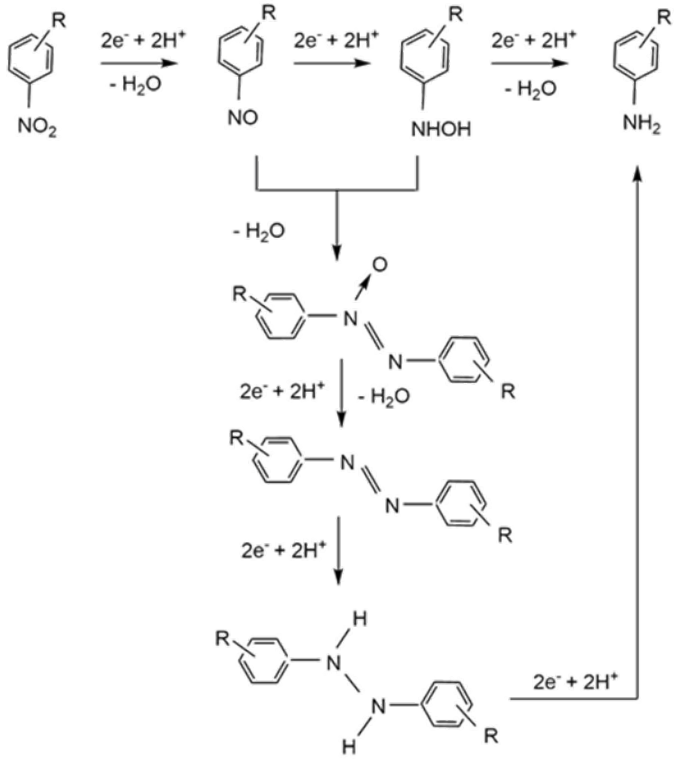

Generally, the reduction of 4-NTP to 4-ATP can occur through two reaction pathways based on the electrochemical model presented by Haber (Scheme 2.1).[128] In the direct reaction pathway, the aromatic compound is firstly being reduced to a nitroso compound and then to a corresponding hydroxylamine, finally reduced to its corresponding aniline. In the indirect reaction pathway, the reduction undergoes a condensation step to form an azo molecule species, before finally being reduced to the corresponding aniline. The indirect reaction pathway is favorable under a relative basic condition. In a theoretical study, Zhao et al[129] proposed that the reaction of 4-NTP to DMAB occurs according to the hot-electron-driven photocatalysis mechanism on gold or silver surface. In a subsequent study, they further concluded that the laser irradiation from the SERS measurement can induce the formation of DMAB as an intermediate product during the six-hot-electron, six-proton photo-reduction of 4-NTP to 4-ATP.[130] Despite the numerous studies on the reduction of 4-NTP, there is still no consensus on the detailed chemical mechanism which the reaction follows, and the available data is insufficient to provide a conclusive inference of photocatalytic pathways. Therefore, a conclusive study on the reduction of 4-NTP to 4-ATP is still necessary.

In this thesis, an easily prepared silver plasmonic film substrate which is suitable for the study of the hot electron-induced photoreduction of 4-NTP by SERS, were presented. The hydrogenation takes place on the surface of silver nanoparticles in the presence of protons and chloride ions rather than a reducing hydrogen source (such as $NaBH_4$, H_2). From the time-resolved SERS measurements, a reaction mechanism was proposed that correctly describes the formation of the 4, 4-dimercaptoazobenzene intermediate under different conditions. The measurements also result in the determination of kinetic rate constants involved in this photocatalytic reaction. The results are critical in clarifying the mechanism for this commonly studied reaction. Moreover, it presents a new simple and cheap substrate for SERS studies that can be applied to other surface photocatalytic reactions that are critical for optimizing energy conversion applications.

3 Materials and Methods

3.1 Chemicals and materials

3.1.1 Chemicals and solvents

The following chemicals solvents were obtained from commercial sources and used without further purification, unless otherwise stated.

Table 3.1 List of chemicals and solvents.

Product	**Company**	
Ammonia (25 %)	Sigma-Aldrich	Taufkirchen, Germany
Bedaquiline	Hycultec GmbH	Beutelsbach, Germany
Benzothiazinone		
Dichloromethane (DCM)	Sigma-Aldrich	Taufkirchen, Germany
DMSO	Merck	Darmstadt, Germany
D_2O	Sigma-Aldrich	Taufkirchen, Germany
Ethanol	Sigma-Aldrich	Taufkirchen, Germany
Formaldehyde solution	Sigma-Aldrich	Taufkirchen, Germany
H_2SO_4	Sigma-Aldrich	Darmstadt, Germany
Hydrochloric Acid (37%, HCl)	Sigma-Aldrich	Taufkirchen, Germany
Linezolid	Sigma-Aldrich	Taufkirchen, Germany
Methanol	Sigma-Aldrich	Taufkirchen, Germany
M7H9 Broth base	Sigma-Aldrich	Taufkirchen, Germany
NaCl	Sigma-Aldrich	Taufkirchen, Germany
$NH_2OH•HCl$	Sigma-Aldrich	Taufkirchen, Germany
Nitrothiophenol (4-NTP)	Sigma-Aldrich	Taufkirchen, Germany
OADC Enrichment	Becton Dickinson	New Jersey, United States
Polyvinylpyrrolidone	Sigma-Aldrich	Taufkirchen, Germany

Rifampicin	Sigma-Aldrich	Taufkirchen, Germany
Silver Nitrate	Sigma-Aldrich	Sigma-Aldrich
Sodium Hydroxide (NaOH)	Merck	Darmstadt, Germany
Sulfuric Acid (95%-98%, H_2SO_4)	Sigma-Aldrich	Taufkirchen, Germany
Tetrabutylammonium Nitrate	Sigma-Aldrich	Taufkirchen, Germany
Trimethoxy(propyl)silane	Sigma-Aldrich	Taufkirchen, Germany
TWEEN® 80	Sigma-Aldrich	Taufkirchen, Germany

Bacterial strains

The mycobacterium strains *Mycobacterium smegmatis* MC^2 155^{17} and *Mycobacterium tuberculosis* $H37_{RV}$ were used in our experiments. The two strains were both provided by Max von Pettenkofer-Institute, Ludwig-Maximilians-University Munich.

3.1.2 Other materials

Double side adhesive tape

Polystyrene semi-micro cuvettes (Brand GmbH, Wertheim, Germany)

Glass slide (26 mm × 76 mm × 1 mm, Carl Roth, Karlsruhe, Germany)

Cover glass (18 mm × 18 mm, Paul Marienfeld, Lauda-Königshofen, Germany)

Hellmanex solution for glass slide cleaning (Hellma, Muellheim, Germany)

3.1.3 Instruments

An Ultrospec 3100 pro (Amersham Biosciences, Little Chalfont, United Kingdom) was used for the optical density 600 (OD 600) measyrement. A Photometer Specord 250 plus spectrometer (Analytik, Jena, Germany) was used to record UV/Vis spectra of the samples. A Zeiss Sigma VP field emission scanning electron microscope (Carl Zeiss GmbH, Berlin, Germany), equipped with an EDS Quantax XFlash 6160 detector (Bruker Nano GmbH, Berlin, Germany) was applied for SEM image acquisition. Plasmonic films were fixed on precleaned glass slides for SERS

measurements. A WITec Alpha 300 R spectroscope equipped with an EM-CCD (WITec GmbH, Ulm, Germany), and a Cobolt DPL 532 nm solid state laser (Cobolt AB, Solna, Sweden) was employed for SERS spectra and Raman imaging collection, 5× objective and 63× (Carl Zeiss AG Jena, Jena, Germany) objective were used for focussing, respectively. A MFD-3D AFM (Asylum Research) equipped with a curvature radius of 7 nm were used to obtain AFM characterization. Double side-adhesive tape was cut by GRAPHTEC cutting plotter CE 6000-40. An ultrapure water purification system (Milli-Q plus 185 Millipore, Schwalbach, Germany) was used for the production of Milli-Q water.

3.2 Experiments and methods for mycobacteria study

3.2.1 Glass treatment

Cleaning

A previously reported method was used for glass slides cleaning.[120, 131] Glass slides were cleaned in a chip reservoir. First, to remove all the possible contaminations, the glass slides were submerged subsequently in various solutions. It starts in 2 % Hellmanex III for 1 h with sonication and then shaking for 16 h. After washing with Milli-Q water and drying with an air flow, the glass slides were dipped in a methanol and hydrochloric acid (volume ratio of 1:1) mixed solution for 1 h during continuous shaking at room temperature. Afterwards, the treated glass slides were thoroughly washed with Milli-Q water again. Afterwards, the slides were submerged in concentrated sulfuric acid for another 1 h under continuous shaking. It was finally cleaned with Milli-Q water, and dried under an air flow.

Hydrophobic treatment

The hydrophobic treatment was also carried out with a modified method.[120] The pretreated glass slides were put in a chip reservoir and submerged in mixed solution containing 150 mL methanol and 150 mL Milli-Q water under continuously magnetic stirring. Afterwards, 2 mL trimethoxy(propyl)silane solution and 3 mL ammonia (25 %) was added to the mixture. Finally, absolute ethanol was used for the cleaning and an air flow for drying. These treated glass slide can be directly used as bottom glass slides in the measurement channels.

3.2.2 Preparation of measurement channels

The Raman measurement were carried out by filling bacterial samples in a lab-made measurement channel. The channel contains three layers, hydrophobic treated glass slides of bottom layer, double side tape of the intermediate layer and the top cover glass layer. The schematic graph of measurement channels is depicted in Figure 3.1.

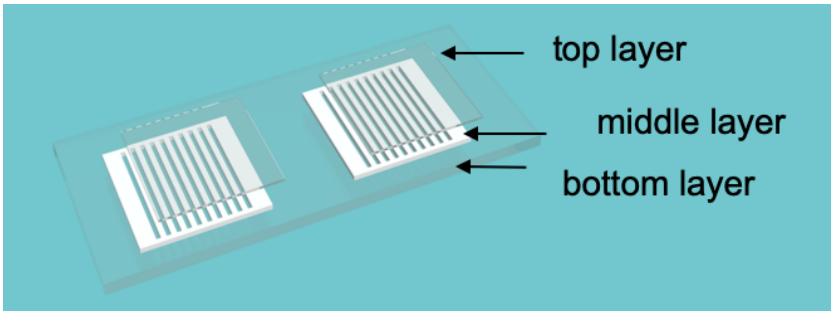

Figure 3.1 Schematic illustration of the experimental set up used for preparation of measurement channels.

3.2.3 Preparation of antibiotic stock solution

Benzothiazinone, bedaquiline, linezolid and rifampicin solutions were prepared by dissolving their chemical compound in dimethyl sulfoxide (DMSO) solvent under a vigorous vortex. The stock solutions of different antibiotics were sterilized before using.

3.2.4 Growth of bacteria in the presence of D_2O and antibiotic

Growth of *Mycobacterium smegmatis* (*M. smegmatis*)

Wide type *M. smegmatis* (strain MC^2 155^{17}) was cultivated aerobically in a sterilized M7H9 medium overnight, supplemented with OADC and 0.05 % Tween-80 (T80) at 37 ℃ under agitation (140 rpm in a shaker). This overnight culture was used for the following antibiotic treatment and deuterium labeling.

An appropriate volume of the *M. smegmatis* overnight culture was used for centrifugation (4500 rpm, 4 ℃). The supernatant was discarded, and the bacterial pellet was resuspended in fresh M7H9 medium to an OD of 0.1. The medium contains 5 × MIC antibiotic and supplements with OADC as well as 0.05 % T80. For accurate measurements, the above bacterial suspension was preincubated with 5 × MIC antibiotic for 3 hours (3 h). Afterwards, the same volume amount of 100% D_2O contained M7H9 medium with OADC and T80 was added to the culture for deuterium

labeling of the bacteria. Thus, 50 % D_2O was included in the merged culture. The bacterial cells then continued to grow at 37 ℃ under agitation. For the investigation of the relationship between deuterium uptake and bacteria growth, bacterial cell cultures (1 mL) growing in the presence of a 50 % D_2O medium for 0 h, 1.5, 3 h, and 4.5 h were taken for formalin fixation and then for SCRI.

Growth of *Mycobacterium tuberculosis* (*M. tuberculosis*)

M. tuberculosis (strain $H37_{RV}$) cultivated in a sterilized M7H9 medium supplemented with OADC and T80 for 7 days. This culture was used for the following antibiotic treatment and deuterium labeling.

An appropriate volume of the *M. tuberculosis* culture was used for centrifugation (4500 rpm, 4 ℃). The supernatant was discarded, and bacterial pellet was resuspended in a fresh M7H9 medium to an OD about 0.2. Similar treatment was done as performed for *M. smegmatis*, but with different 5 × MIC antibiotic concentrations and different D_2O durations. In Raman samples, duration of *M. tuberculosis* deuterium labeling are 0 h, 12 h, 24 h and 36 h.

3.2.5 Bacterial growth curve measurement in the presence of D_2O

The bacterial growth was determined using optical density (OD) measurements at λ=600 nm with a spectrophotometer. Briefly, a fresh bacterial culture was diluted to a proper OD with a fresh sterile nutrient broth containing different percentages of D_2O (0 %, 10 %, 25 %, and 50%). The bacterial OD was monitored at different time points. The medium M7H9 with the corresponding concentration of D_2O was used as a reference. As a result, the growth curve of bacteria was presented by plotting OD (Y-axis) against cultivation time (X-axis).

3.2.6 MIC determination

The MIC (minimum inhibitory concentration) measurement was performed using the broth dilution method as described previously.[132] In short, fresh mycobacterial cultures were grown in a M7H9 medium with increasing concentrations of antibiotics. The MIC value is defined as the lowest concentration that inhibits the growth of bacteria. The growth of bacteria is determined by optical density measurements at λ = 600 nm (OD 600) with a spectrophotometer.

3.2.7 Raman sample preparation and single cell Raman imaging

Raman sample Preparation

For Raman measurement, bacterial cells were initially fixed by formalin solution. In the formalin fixation, 900 µl mycobacterium culture collected in the presence of 50 % D_2O and antibiotic, first mixed with 100 µl formalin (37 %) solution by vortexing. Afterward, the mixture was incubated for 20 min in an ice bath. Later on, a centrifugation step (4500 rpm, 4 °C and 10 min) was used to collect the formalin-fixed bacteria cells. The resulting pellet was washed twice by NaCl (0.9 %) solution for removing residual medium and formalin solution. After another centrifugation step, the bacterial pellet was dispersed and saved in 500µl NaCl (0.9 %) solution. After the treatment, the bacterial suspension can be directly filled in the measurement channels for Raman measurements.

Single cell Raman imaging (SCRI)

The bottom glass slides of the channel were specially treated for hydrophobicity beforehand. The slides were used for catching mycobacteria cells because of the hydrophobic interaction between the hydrophobic glass slide surface and intrinsic hydrophobic nature of the mycobacteria cell wall. The channels filled with formalin-fixed bacterial suspension were sealed with hot wax at its two sides allowing bacteria cells to stay in liquid during the measurement. Before the Raman measurement, the sealed channel was allowed to stand for 20 minutes to ensure that the bacteria cells sediment and are were fixed to the bottom hydrophobic glass slides. Thus, the bacteria cells will not move in the liquid; single cell can be selected for Raman imaging measurement. The bacteria cells fixed in the measurement channel enable the application of a confocal Raman microscopy with an oil immersion objective. The Raman measurement is performed with WITec Alpha 300 R equipped with a Cobolt DPL 532 nm solid state laser (Cobolt AB, Solna, Sweden) and 600 grooves/mm grating. A high numerical aperture (NA) oil immersion objective (63×, NA 1.4, working distance 0.15 mm, Carl Zeiss AG, Germany) lens was used for imaging. The application of high NA microscopy allows a spatial resolution (spatial resolution $d = \frac{0.51\lambda}{NA}$)[133] around 0.23 µm in the measurement. In SCRI measurements, Raman images of different areas were selected depending on the size of different bacterium. For all single organism mapping, 30 mW laser power, 0.5 s per spectrum and 0.25 µm step size were applied for image acquisition. The

spectral center was set at 2200 cm^{-1}. Roughly, 100 single bacteria were measured for each D_2O duration.

3.2.8 Raman data processing for single cell imaging

After spectra acquisition, cosmic rays in the raw data of SCRI were initially removed from all spectra using a graph filter (filter size of 4 and dynamic factor of 7) of WITec project five software. For the quantification of deuterium uptaken by the cells from the growth media, the measured spectra were decomposed to extract the distinct spectral features of C-D and C-H stretching vibrations. The spectral region between 1900 to 3100 cm^{-1} was selected for multiple linear regression (MLR). As sketched in Figure 3.1, each measured spectrum is composed of C-D (1950-2300 cm^{-1}) and C-H (2800-3038 cm^{-1}) bands from bacteria, Raman bands from bottom glass (the bottom hydrophobic glass where bacteria are fixed) and medium (0.9 % NaCl, bacteria are measured in 0.9 % NaCl solution). Raman spectra of these four independent components (C-D, C-H stretching vibrations, bottom glass, and liquid in the channel) were taken as references for the MLR. The reference of C-D bands are fitted by a Gaussian function $y = 1.1 \times e^{-\left(\frac{x-2150}{84}\right)^2}$, with a full width at half maximum of 139.8 cm^{-1} and a fitting tolerance of 0.010. Raman spectra of these four references are displayed in Figure 4.4. Thus, a linear combination of these four components (i_{glass}, i_{media}, i_{CH} and i_{CD}) with their corresponding response coefficients ($ß_{glass}$, $ß_{media}$, $ß_{CH}$ and $ß_{CD}$) were calculated to predict their amount in the overall spectra by the following eq. 5.

$$I_s = I_0 + i_{glass}ß_{glass} + i_{media}ß_{media} + i_{CH}ß_{CH} + i_{CD}ß_{CD} + I_e \quad \text{eq. 5}$$

In eq. 5, I_0 and I_e are the intercept to the y-axis and residue, corresponding to the background and spectra difference (residue) from MLR and measured spectrum, respectively.

The distribution of each component in Raman imaging can be presented by calculating $i_i ß_i$ (subscripted i represents each component) images. It is known that the C-D band intensity is proportional to D_2O concentration and D_2O duration.[3-6] Thus, the ratio between the amount of C-D and C-H ($i_{CD}ß_{CD}/i_{CH}ß_{CH}$, recorded as CD / CH) can be used for indicating bacterial metabolic activity. All Raman images were evaluated by MLR.

A complete Raman spectrum was acquired at every image pixel. Theoretically, for image pixels located at the background area (not bacteria), their regression coefficients for C-D and C-H should be zero. But, in the real calculation, these coefficients are very close to zero, but not zero. Therefore,

we use the following calculation to define whether a pixel belongs to bacteria in each image. For each pixel, if $i_{CH}ß_{CH}$ is larger than the two times standard deviation of all pixels of each image, then it is defined as a bacterial pixel (spectrum containing bacteria C-D and C-H bands). Otherwise, it is part of the background. In boxplots, the average $i_{CD}ß_{CD}/i_{CH}ß_{CH}$ of all bacterial pixels in each image were used as one data point.

To calculate the spatial CD / CH distribution, images of individual bacteria labeled with deuterium were analyzed with MATLAB using the 'convhull' (select the long axis of bacteria based on CD / CH matrix of each imaging) and 'imrotate' (rotate the long axis of bacteria parallel to x-axis in each CD / CH imaging frame) function to place bacterial cells on the long axis parallel to the x-axis in each image. For each bacterium, the CD / CH at each pixel were plotted to its position along the long axis of the bacterium. The 'pcolor' plot was used to present the results on the listed number of individual bacteria from shortest bacterium to the longest bacterium using 'sort' function in MATLAB.

3.3 Experiments and methods for the observation of photocatalytic reaction

3.3.1 Silver colloid preparation

Silver colloid preparation was performed according to the Leopold-Lendl method.[34] In this preparation, $AgNO_3$ is reduced by NH_2OH•HCl. First, reducing solution was freshly prepared with NH_2OH•HCl (11.6 mg, 0.17 mmol) and NaOH solution (3.3 mL, 0.1 M) diluted by Milli-Q water to a volume of 100 mL. Each time, Ag colloid was newly prepared from 45 mL of the above reducing solution with the addition of $AgNO_3$ (5 mL, 10 mM) solution with a greenish yellow color.

3.3.2 Ag plasmonic film (AgPF) preparation

The prepared silver colloid (4 mL) was centrifuged, and the supernatant was discarded. The pellet of the 4 mL silver colloid was redispersed in 1 mL Milli-Q water. Because of the low stability of above silver colloid, PVP (1 mL, 0.01 mg/mL) was primarily added to four times the concentrated silver colloid in a 2 mL centrifugation tube which has hydrophobic surface. After, DCM (500 µL) was added. For interfacial nanoparticle film promotion, tetrabutylammonium nitrite (TBAN, 200 µL, 10^{-2} M) was used in the mixture. After about 1 min under vigorous shaking, free silver

nanoparticles migrated to the interface and formed a metallic layer wrapped around the upper aqueous phase. That is the target metal liquid-like film (MeLLF). The tip of a polymer tube, carrying a circular piece of double side adhesive tape (diameter: 7 mm), was placed horizontally on top surface of MeLLF, thus picking up a fraction of the MeLLF on the adhesive tape. Finally, a plasmonic film was obtained. To ensure the MeLLF build up around the upper aqueous phase, the MeLLFs were prepared in hydrophobic tubes made of polypropylene (PP).

3.3.3 4-NTP reaction test

The 4-NTP was adsorbed onto the AgPF before starting the hot electron-induced reaction test. The AgPFs were submerged into 1 mL aqueous solution of 4-NTP (7.0×10^{-2} M) for two hours to allow for its absorption. Afterwards, the hot electron-induced reduction of 4-NTP was promoted by addition of 100 μL aqueous droplet including NaCl and HCl or H_2SO_4 on 4-NTP modified plasmonic film. Different proton concentrations were generated by the hydrochloric acid concentration. Then, the reaction was initiated and processed by continuous irradiation of a Cobolt DPL 532 nm solid state laser (Cobolt AB, Solna, Sweden). The SERS spectra recorded by a WITec Alpha 300 R microscope (WITec GmbH, Ulm, Germany). using a solid-state laser (532 nm) and 5× objective (with a NA of 0.25). The laser beam size is approximately 2.6 μm. The maximum laser power used in the measurement is 5 mW, corresponding to 0.94 mW μm^{-2}.

4 Results and Discussions

4.1 Growth and antibiotic sensitivity investigation of mycobacteria by Raman spectroscopic imaging of deuterium incorporation at single cell level

4.1.1 Deuterium incorporation in bacteria growth using single cell Raman imaging

To start the experiments, the mycobacterial growth sensitivity to D_2O was tested by cultivating them in the presence of different amounts of D_2O. The bacterial concentration was determined by an OD 600 measurement. It can be seen in Figure 4.1a that $D_2O \leq 50$ % (with respect to the normal water in bacterial medium) in the medium does not significantly affect the growth of *M. smegmatis*. A certain toxicity is present for *M. tuberculosis* in 50 % D_2O (Figure 4.1b). It is clearly shown that D_2O significantly inhibits the growth of *M. tuberculosis*. In this thesis, a medium containing 50 % D_2O was applied for the observation of mycobacterial metabolic activity using Raman microscopic imaging.

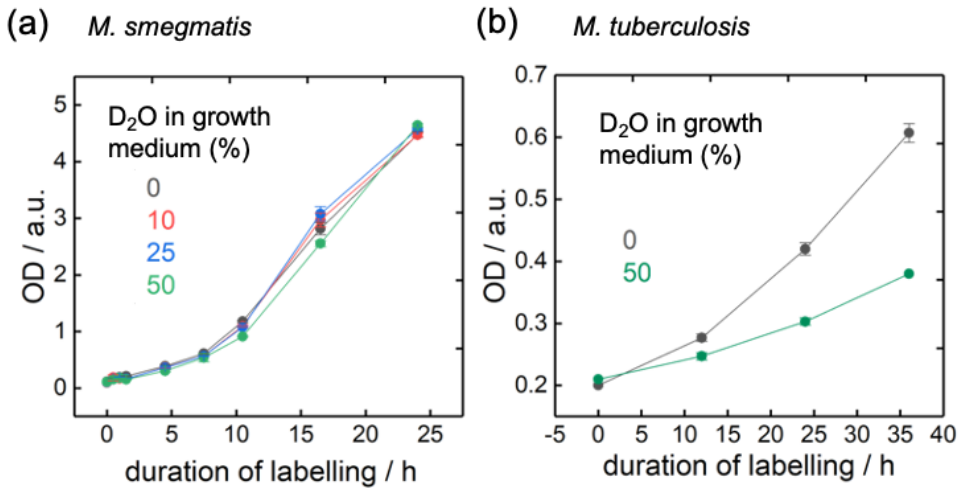

Figure 4.1 Growth cure for *M. smegmatis* and *M. tuberculosis* observed by OD 600 measurement in different amounts of D_2O containing medium.

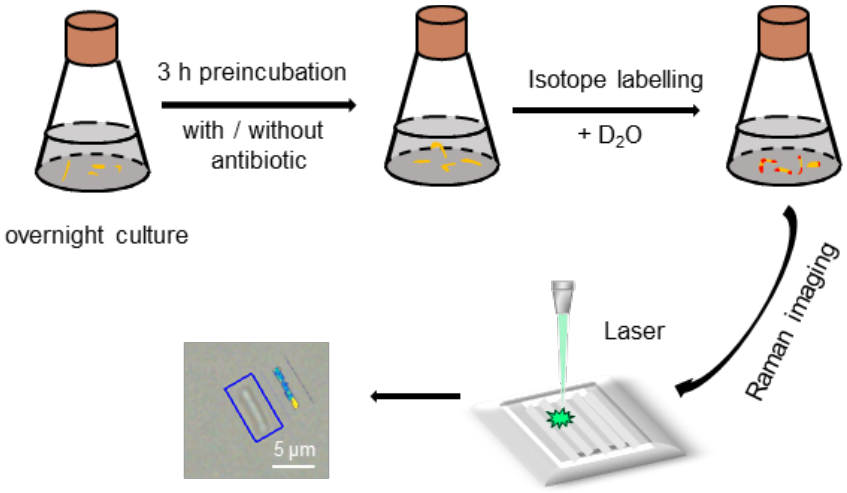

Figure 4.2 Experimental illustration for SCRI protocol.

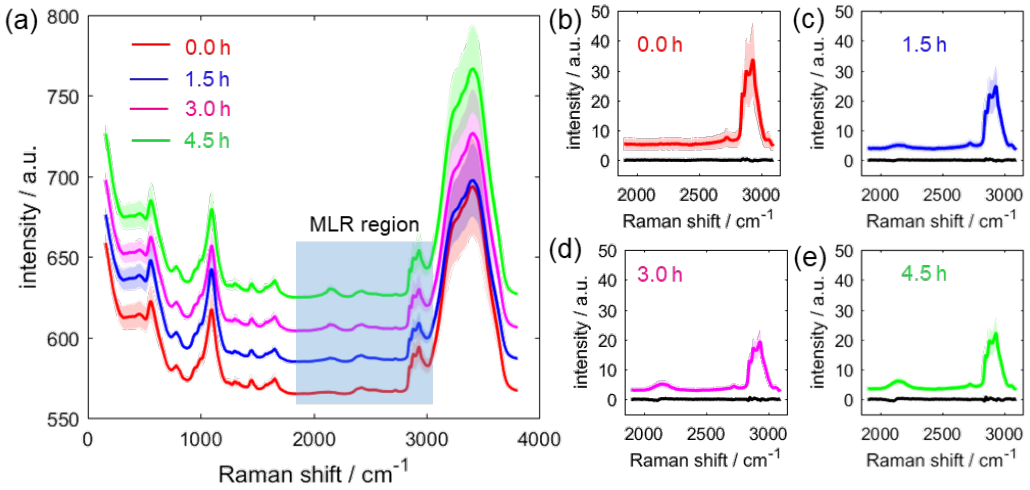

Figure 4.3 Raman spectra of *M. smegmatis*. (a) Average spectra of measured data from 95 to 101 Raman images at each D_2O duration, (b-e) estimated bacterial spectra containing deuterium labeling C-D and non-deuterium labeling C-H bands at different D_2O durations (0.0 h, 1.5 h, 3.0 h, and 4.5 h) and their corresponding regression residue (blacks lines in each figure). The translucent areas in each mean spectrum correspond to their standard deviation from 95, 95, 101, 98 single cell images for 0 h, 1.5 h, 3.0 h and 4.5 h deuterium labeling, respectively.

In bacterial deuterium labeling, overnight *M. smegmatis* culture was preincubated for 3 h. Then, the same amount of pure D_2O prepared medium was added. Thus, bacteria continue to grow in the M7H9 medium containing 50% D_2O. The deuterium-labeled bacteria were collected after labeling with D_2O for 0 h, 1.5 h, 3.0 h and 4.5 h, and then fixed with 3.7% formalin solution to stabilize all proteins, so that the integrity of membranes would not change. This fixation step enables bacteria to be measured with a long integration time (minutes for one cell). The formalin-fixed samples

were then filled in the measurement channels (shown in Figure 3.1) and ready for Raman imaging. Due to the hydrophobicity of the *M. smegmatis* cell wall, bacteria cells were fixed to the bottom hydrophobic treated glass slide of measurement channels. Then, a single cell was selected and measured in a liquid environment. The advantage of performing bacterial Raman measurements in 0.9% NaCl solution is that they are close to their original physiological shape. The workflow is presented in Figure 4.2. For SCRI, bacteria were fixed on the surface of the bottom hydrophobic glass slide (Figure 3.1) and numbers of single cells were randomly selected for Raman imaging. For each cell, Raman spectra were collected from each image pixel. A typical Raman shift caused by deuterium incorporation is presented in Figure 4.3a. At the beginning (0 h incorporation with D_2O), there is no C-D band signal. Overtime, the C-D signature, whose Raman frequency is assigned at range 1950-2300 cm^{-1} emerges and the intensity increases with increasing deuterium duration. The incorporation of D_2O into *M. smegmatis* cells during the reduction steps of fatty acids synthesis causes deuterium to replace hydrogen in the bacterial macromolecules (such as lipids, proteins, and DNA), which is based on bacterial metabolism. Thus, the C-D amount in bacterial Raman spectra can be detected as a general indicator of bacterial metabolic activity. For the quantification of the C-D content, our Raman spectra were evaluated by the MLR at wavenumber region of 1900 to 3100 cm^{-1}, as described in data processing section. In a single-cell image, the MLR can decompose the measured Raman spectra (Figure 4.3a) which contain signals coming from the background (bottom glass and 0.9 % medium) bacteria (C-D and C-H stretching bands). The unmixed bacterial spectra (without signals from bottom glass and medium) can be estimated by combining the MLR regression coefficients of the deuterated (C-D stretching band) and non-deuterated (C-H stretching band) bacterial bands which can be seen in Figure 4.3b-e. In the regression, the spectra in Figure 4.4 are the four reference spectra used for MLR analysis. The reference spectra were normalized before being used for regression. The residual plots (Figure 4.3b-e, black lines) show the difference between measured spectra and the estimated spectra from MLR. The small residuals in Figure 4.3b-e (black lines) and large coefficient of determination (R^2 at each image pixel is larger than 0.90.) indicates that the overall accuracy of the MLR is remarkable, the decomposition of different components in the measured spectra is successful. However, the residuals at the C-D band region increases slightly as the duration of labeling increases. This phenomenon is assumed due to the minor variation in the real Raman spectrum of C-D bond. It has been reported that in the bacterial Raman spectra, the C-H stretching region

contains three main bands, which are derived from lipid-related CH_2 stretching, protein-related CH_3 stretching and DNA-related CH stretching. Thus, the appearance of the C-D band, based on newly synthesized lipids, proteins and DNA, also contains three main bands. However, in our spectra, the C-D stretching frequencies do not allow the separation of the different deuterium-labeled macromolecules, even with the highest C-D intensity (Figure 4.3a of deuterium duration 4.5 h). In all, the C-D band used in the refences of MLR is acceptable.

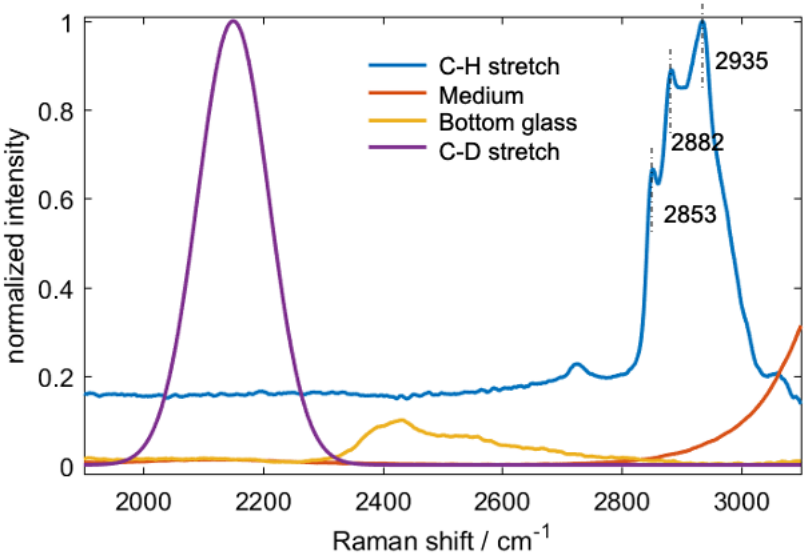

Figure 4.4 Reference spectra for MLR evaluation. Raman spectra of C-H stretching vibration (blue), medium (red), bottom glass (yellow), and C-D stretching vibration (purple).

In the MLR results, the amount of labeled and unlabeled macromolecules can be separately analyzed, based on the regression coefficients of C-D band and C-H band at each bacterial pixel in single cell. Thus, the regression coefficient ratio of C-D band to C-H band (recorded as CD / CH) can be used as an indicator of bacterial metabolic activity. The growth is different from the common symmetric growth of rod-shaped bacteria (such as, *E. coli*), *M. smegmatis* is reported to grow asymmetrically (shown in Figure 4.5a) which has been proved by live cell imaging.[2] Representative Raman images of CD / CH at different D_2O incorporation time are presented in Figure 4.5b, and their corresponding average regressed spectra are shown in Figure 4.5c. Figure 4.5c describes the average regressed bacterial spectra at all bacterial pixels and their standard deviation also presented. The C-D band is visible after 1.5 h with D_2O incorporation. The newly synthesized macromolecule (deuterium-labeled) can be clearly discriminated in our CD / CH image. In these CD / CH images (Figure 4.5b), the yellow pattern indicates high CD / CH area,

which does not show after 0 h of D_2O incorporated image. That pattern appears from one bacterial pole at 1.5 h of D_2O incorporation to two poles at 3.0 h of D_2O. Moreover, it can be clearly seen that the yellow pattern in cell two poles are different, one polar has colored more than the other one. To some extent, we can conclude that *M. smegmatis* asymmetrically metabolic at their poles. It is obvious that longer D_2O exposure leads higher ratio of CD / CH. Each average CD / CH for all pixels of single cell image corresponds to its metabolic activity. During bacterial growth, CD / CH increased significantly in a large cell population (Figure 4.5d). In Figure 4.5d, each CD / CH value of individual scatter represents bacterial metabolic ability in a cell. The variation of metabolic activity between individual cells is clearly shown. Clear subpopulations are present in Figure 4.5d by shown kernel density simulated distribution curve (red outlines). It is clearly shown in Figure 4.5b that the newly synthesized macromolecules are preferentially distributed at bacterial poles. It can summarize that using Raman imaging combined with D_2O labeling enables the visualization of macromolecule metabolic activity by calculating their CD / CH value at the single cell level. Only active cells will consume D_2O for their metabolism, while inactive (dead cells) will not. Thus, the CD / CH of dead bacteria is very small (Figure 4.6), even with a very long incubation time. Above all, the active mycobacterial cells can consume D_2O and incorporate the deuterium into their biomass that can be visible within single cell resolution by Raman imaging measurements. In this way, the heterogeneous response of bacteria to four different antibiotics were investigated at single cell level.

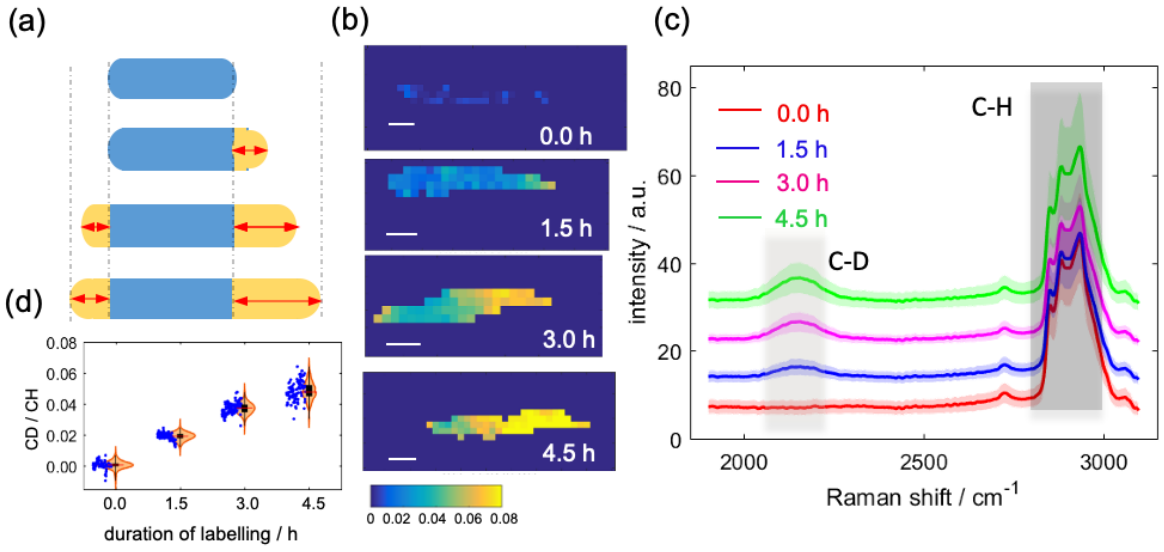

Figure 4.5 (a) Schematic diagram of asymmetric growth of *M. smegmatis*. Before bacterium division, the cell elongates from its two poles. (b) Representative CD / CH ratio images at each labeling duration and (c)

their corresponding average spectra (with standard deviation in translucent color). (d) Temporal dynamics of CD / CH of *M. smegmatis*. Each point represents the average CD / CH of one image. 95, 95, 101, 98 images for 0 h, 1.5 h, 3.0 h and 4.5 h of D_2O incorporation were tested, respectively. The red line in box represents mean CD / CH of these amounts of images in each group.

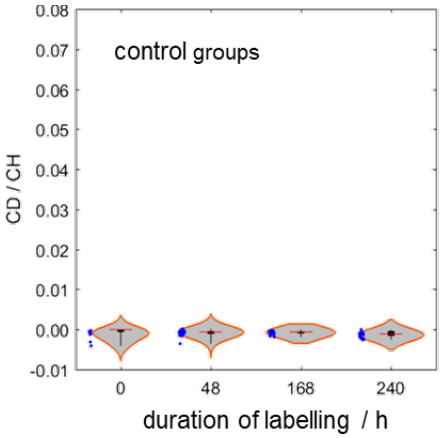

Figure 4.6 CD / CH of dead *M. smegmatis* for different duration of labelling.

4.1.2 Raman imaging of *M. smegmatis* exposed to different antibiotics

The bacteria division and elongation would be inhibited with antibiotic treatment. Bacterial cells response differently to antibiotics. Here, we exposed bacteria to different antibiotics, then tracked the responses of individual bacterial cell metabolic ability by single cell Raman imaging. The rarely pathogenic mycobacterial strain *M. smegmatis* were tested firstly as our modal organism. Following the strategy in Figure 4.2, a pre-incubation time of 3 h with antibiotics was used before D_2O addition. This preincubation with antibiotic is to ensure that the bacteria have time to respond to the antibiotic before deuterium uptake. Thus, the monitoring of the C-D band can representatively describe bacterial metabolic activity in the presence of antibiotics. Prior to antibiotic pre-incubation, the concentration of bacterial dispersion was adjusted to an OD 600 of 0.1 for all *M. smegmatis* tests.

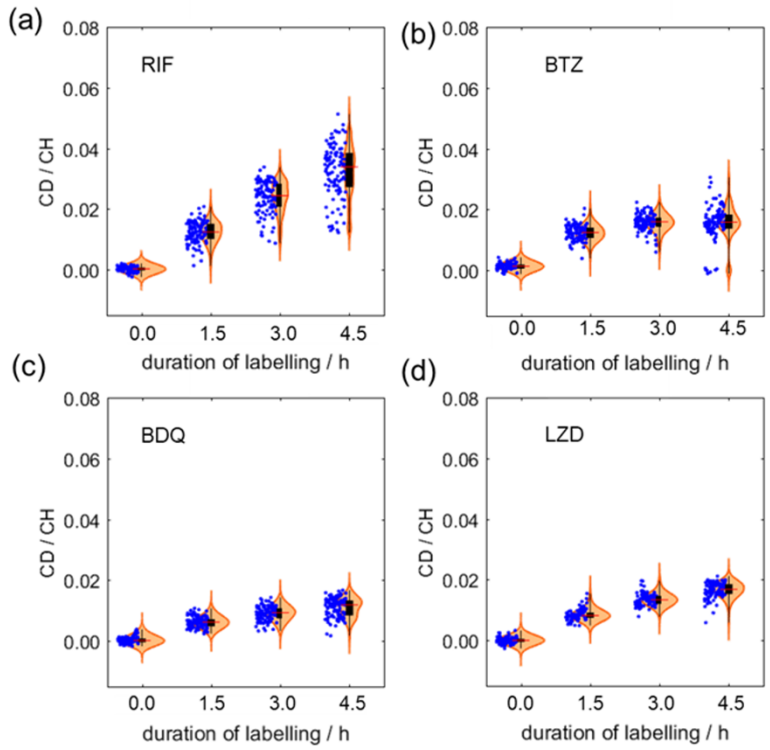

Figure 4.7 Boxplots of mean CD / CH for each single cell Raman image under (a) RIF, (b) BTZ, (c) BDQ and (d) LZD. The analysis here includes more than 90 single cell images at each deuterium incorporation time under different antibiotics. Bacteria were randomly selected for Raman imaging measurement. The red outlines around boxplot are the distribution curves estimated from the kernel density of each group. Each scatter in the plots corresponds to average CD / CH of each image.

Rifampicin (RIF), linezolid (LZD), benzothiazinone (BTZ), and bedaquiline (BDQ) were used to study the effects of antibiotics on *M. smegmatis* and *M. tuberculosis*. It is important to appreciate that different antibiotics have different mechanisms of action. BTZ and BDQ inhibit the cell wall and ATP production in bacteria, respectively. RIF and LZD work by inhibiting the synthesis of RNA and protein, respectively. The minimum inhibitory concentration (MIC) is defined as the minimal dose at which no visible bacterial growth (normally measured at OD 600) is detected within 24 h of antibiotic exposure. The values of MIC are determined using the broth dilution method, the values are listed in Table 4.1. The CD / CH under the influence of different antibiotics with increasing duration of D_2O exposure are displayed in Figure 4.7. For each of the antibiotics, there is an increasing CD / CH ratio with increasing time of deuterium incorporation. That means the bacteria are still metabolically active under the stressor of five times of the MIC value of antibiotic after 4.5 h. Compared to the bacteria without antibiotic treatment in Figure 4.5d, the CD / CH are smaller at same incorporation time. That means the bacterial metabolic activity slowed

down upon antibiotic treatment. Moreover, this slowing effect is different between the four antibiotics. Moreover, it is clear from Figure 4.8 that C-D bands are observed in *M. smegmatis* spectra of RIF and BTZ (0.046 µg/mL and 0.0215 µg/mL in the bacterial suspension, respectively) treated cells with short D_2O duration (1.5 h). A weak C-D band is presented in BDQ and LZD (0.046 µg/mL and 2.1 µg/mL in the bacterial suspension, respectively) treated cells, even with a longer D_2O duration (4.5 h). It could conclude that *M. smegmatis* is more sensitive to BDQ and LZD.

Table 4.1 MIC of antibiotics for *M. smegmatis* and *M. tuberculosis*.

Antibiotic	MIC for *M. smegmatis* (µg/mL)	MIC for *M. tuberculosis* (µg/mL)
RIF	0.0092	0.015
BTZ	0.0043	0.001
BDQ	0.0092	60
LZD	0.42	1.3

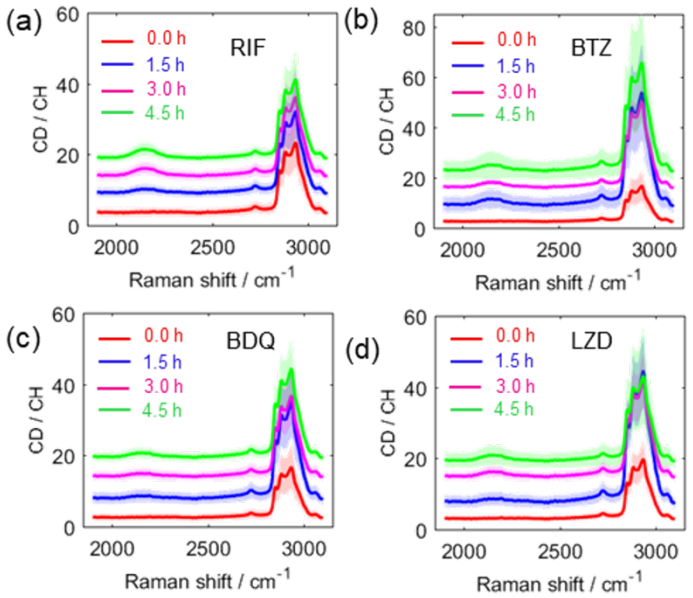

Figure 4.8 Average spectra from more than 90 Raman images of *M. smegmatis* under treatment with (a) RIF, (b) BTZ, (c) BDQ and (d) LZD for different duration of labeling (0 h, 1.5 h, 3 h, and 4.5 h). The translucent areas in each average spectrum correspond to their standard deviation.

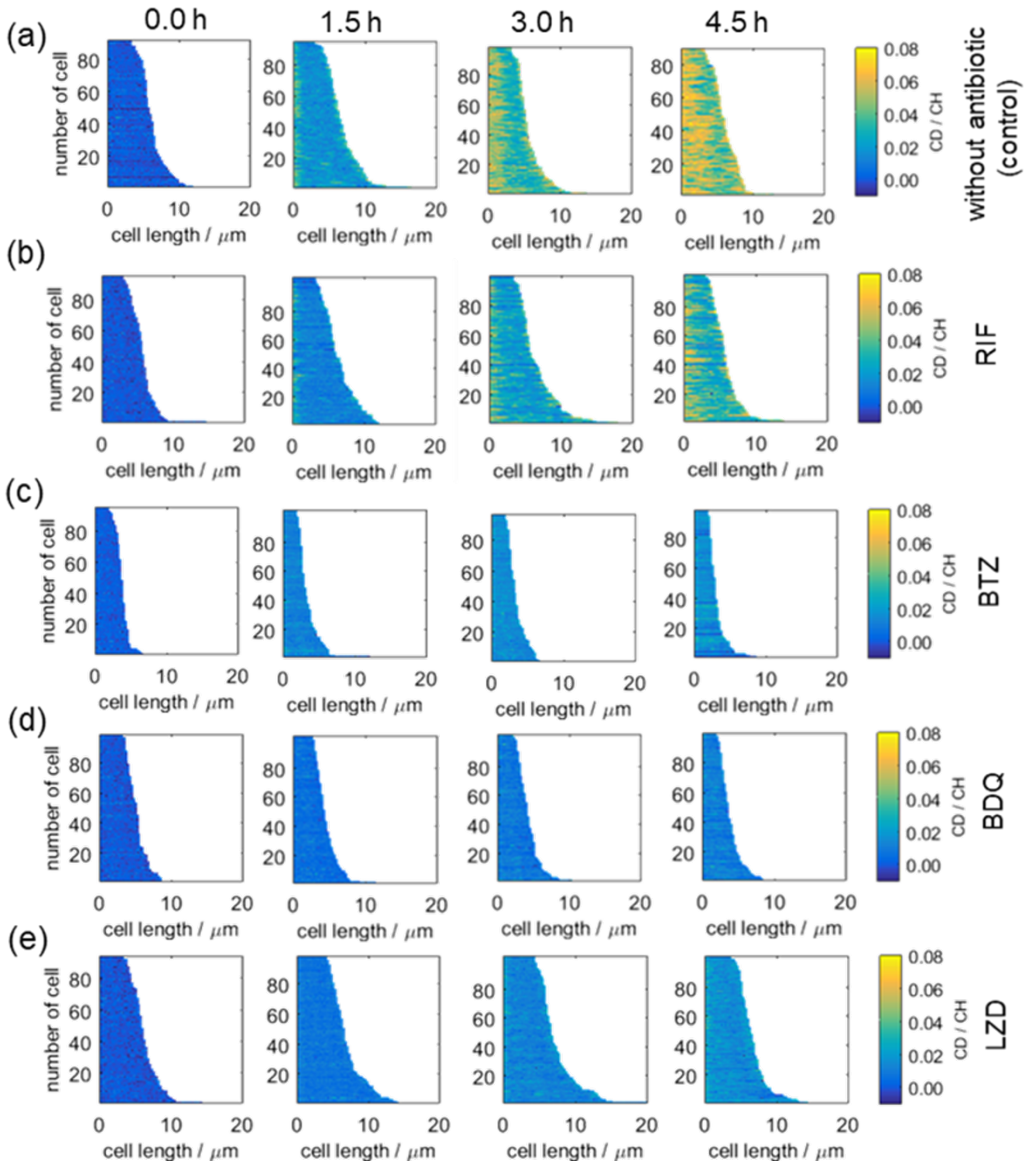

Figure 4.9 Spatial CD / CH ratio distribution along the long axis of *M. smegmatis* at each D_2O durations without (a) antibiotic treatment for the control and with (b) RIF, (c) BTZ. (d) BDQ, (e) LZD treatment.

From the Raman images, not only the CD / CH variation between each individual cell can be obtained, but also insight into the spatial information of CD / CH distribution of each cell is achieved, as shown in Figure 4.5b. Form the Raman images (such as Figure 4.5b), we can see that each position of the long bacterial axis has several bacterial pixels along the short axis of bacteria. To directly view the individual bacterial CD / CH distribution in a population, the average CD / CH ratio along the short axis of bacteria were initially calculated. These average CD / CH represent bacterial metabolic activity at their bacterial long axis position. Then, bacterial spatial information was compacted by plotting these average CD / CH along the long axis of bacterial cell, and all the

results are shown in Figure 4.9. The side with higher CD / CH values is placed on the left. Each heat map presents a set of measurements. Form this figure, we clearly see CD / CH distributions along the long axis of each bacterial cell. The higher the ratio of CD / CH, the more active the biosynthesis. Without an antibiotic-treated group was recorded as a control measurement which is presented in Figure 4.9a. The color bar in Figure 4.9a indicates the CD / CH ratio. The color displayed in yellow represents a larger CD / CH ratio value than blue. Comparing the distribution collected for 0, 1.5, 3 and 4.5 h of D_2O incorporation, it can be seen that deuterium incorporation from D_2O into *M. smegmatis* occurred initially in bacterial one pole at a time of 1.5 h. After that, the incorporation increases and expands into the middle of the same pole. We also noticed that the length of yellow pattern is determined at each D_2O duration. It has nothing to do with the individual bacterial length. For example, in most cells, the length of the yellow pattern at the left side of 1.5 h D_2O incorporation in Figure 4.9a is 0.75 μm. The length of the yellow pattern expanded in 3.0 h D_2O incorporation in most cells is also similar (around 2 μm). In addition, significant differences in bacterial cell length were observed. In the presence of BTZ (0.0215 μg/mL) and BDQ (0.046 μg/mL), the overall cell length is shorter than in the presence of RIF (0.046 μg/mL) and LZD (2.1 μg/mL). This is in accordance with different antibiotic response mechanisms. In summary, the sensitivity of a single bacterium to antibiotics can be identified by calculating the average CD / CH in each single cell. Based on the distribution of CD / CH in a single cell, we can visualize metabolic activity at bacterial poles and in the middle. From Figure 4.9a-b, we can also see that the yellow pattern in bacterial two poles is asymmetric. This further proves the heterogeneous metabolism within individual bacterial cells. Our observation is based on the separation of highly deuterium-labeled and lightly deuterium-labeled macromolecules in a single bacterial cell which has not been investigated previously.

4.1.3 Raman imaging of *M. tuberculosis* exposed to different antibiotics

The above study shows the successful incorporation of deuterium from D_2O into the biomass of *M. smegmatis* for single-cell metabolic imaging. Applying the same technique to the dangerous mycobacteria (*M. tuberculosis*), we also can distinguish the highly deuterium-labeled bacterial patterns from low deuterium-labeled patterns during bacterial metabolism. Its susceptibility to different antibiotics was also tested at single-cell resolution, following the same workflow. For the temporal dynamic measurements, 0 h, 12 h, 36 h, and 48 h for D_2O incorporation were applied,

based on the longer (doubling time of 24 h for *M. tuberculosis* compared to a doubling time of 3-4 h for *M. smegmatis*) doubling time of *M. tuberculosis*. Prior to antibiotic pre-incubation, the concentration of the bacterial solution was adjusted to an OD 600 of 0.2 for all *M. tuberculosis* tests. Figure 4.10 presents the spectra of *M. tuberculosis* collected at different D2O duration in the absence of antibiotics. We can see in Figure 4.10 that the spectrum of *M. tuberculosis* is similar to that of *M. smegmatis* in Figure 4.3a. The difference between these two mycobacterial strains locates at the C-H band. The bacterial Raman bands at 2855 cm^{-1}, 2882 cm^{-1}, and 2936 cm^{-1} correspond to lipid-related CH_2 stretching, protein-related CH_3 stretching, and DNA-related C-H stretching, respectively.[10] In *M. smegmatis*, the intensity of DNA-related C-H stretching band is the highest among these three bands (Figure 4.3a, C-H bands), while the intensity of protein-related CH_3 stretching band is the highest in *M. tuberculosis* (Figure 4.10, C-H bands). The emergence and enrichment of the C-D band in Figure 4.10 means the deuterium incorporation from D_2O into *M. tuberculosis* cells is also sensitive enough to identify active and inactive *M. tuberculosis* cells. The metabolic heterogeneity within individual cells will be presented in the following spatial information analysis part.

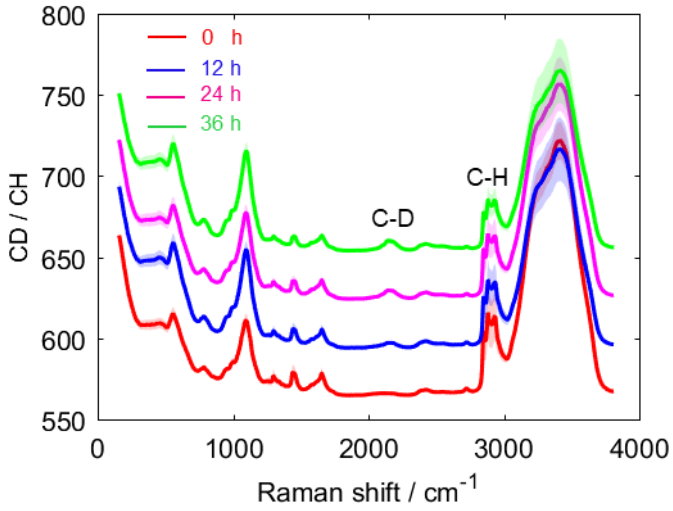

Figure 4.10 Each spectrum corresponds to an average Raman spectrum of *M. tuberculosis* (measured in liquid) from 92 to 99 Raman images at different D_2O duration (0 h, 12 h, 24 h, and 36 h). The bacteria cultivated in the presence of 50 % D_2O medium. The translucent areas in each average spectrum correspond to their standard deviation.

For *M. tuberculosis*, five times of the MIC value of each antibiotic was used. The concentrations of RIF, BTZ, BDQ, and LZD are 0.075 µg/mL, 0.005 µg/mL, 300 µg/mL, and 6.5 µg/mL,

respectively. The CD / CH variation between cells was presented in Figure 4.11. It is clear that the CD / CH at the same time point is smaller in the presence of antibiotics (Figure 4.11a-d) than in the absence of antibiotics (Figure 4.11e). The standard deviation (SD) increases with increasing incubation time in the presence of D_2O and without antibiotics. When *M. tuberculosis* cells were incubated in D_2O for 4.5 h, the percentage SD could reach 240 % (Figure 4.11e). This number indicates the difference in bacterial metabolic activity between individual cells. Clear subpopulations can be defined by kernel density estimation.

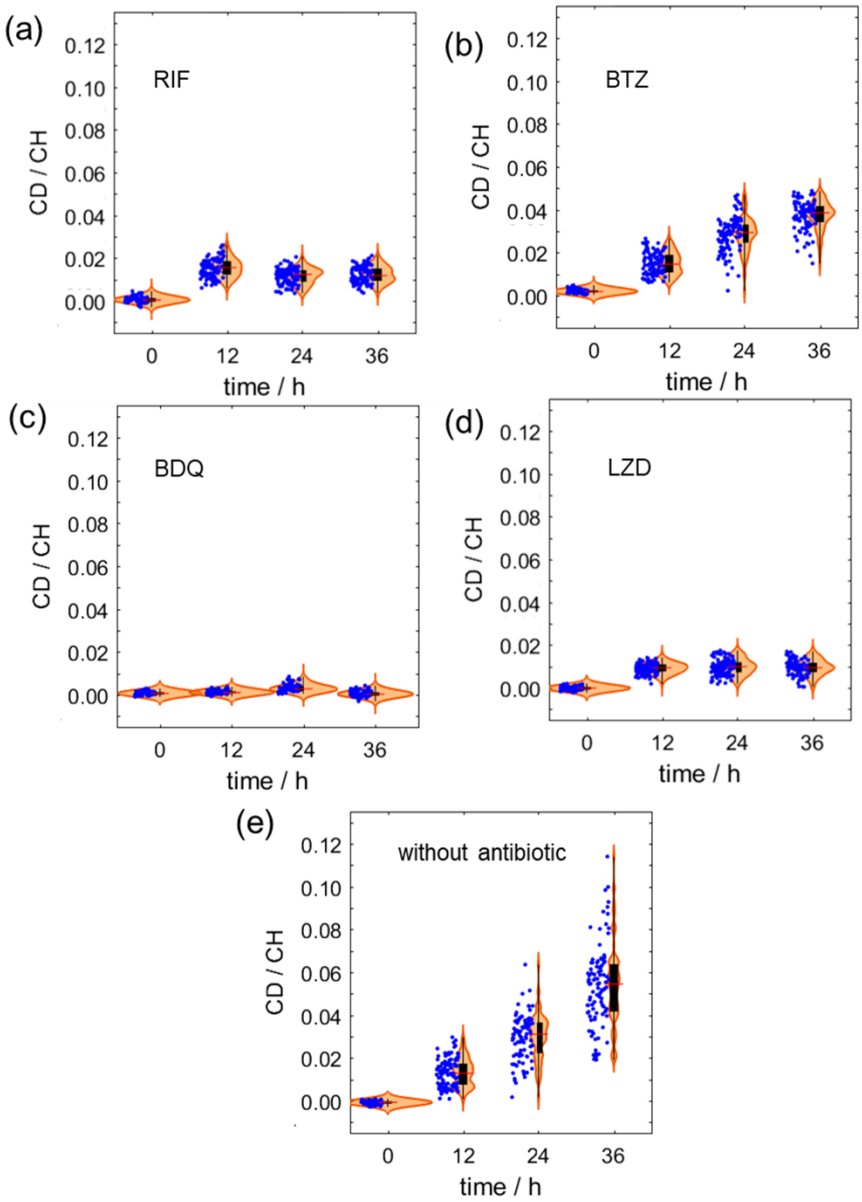

Figure 4.11 Boxplots of average CD / CH for each single cell Raman image under different antibiotics (a) RIF, (b) BTZ, (c) BDQ and (d) LZD, and (e) the control group without antibiotic treatment. The red outlines

around boxplot are the distribution curves estimated from the kernel density of each group. Each point in the figure presents one average CD / CH of one Raman image. The analysis here includes numbers of single cell images at each deuterium incorporation time. Bacteria were randomly selected for Raman imaging measurement. Each scatter in the plots corresponds to average CD / CH of each image.

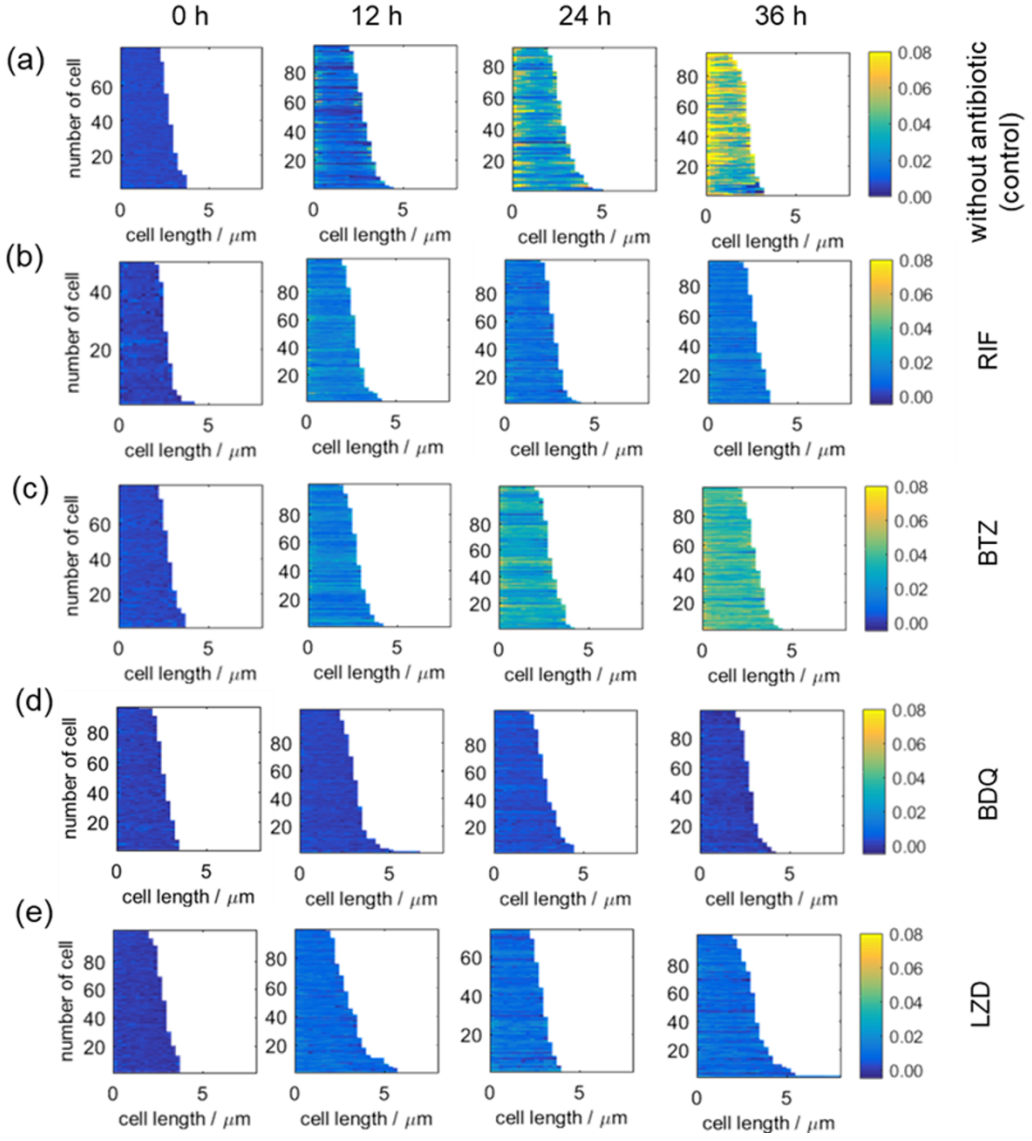

Figure 4.12 Spatial CD / CH ratio distribution along the long axis of *M. tuberculosis* at each D_2O durations (a) without antibiotic treatment and treated with (b) RIF, (c) BTZ. (d) BDQ, (e) LZD. Numbers of single cells were randomly selected for the Raman imaging measurements.

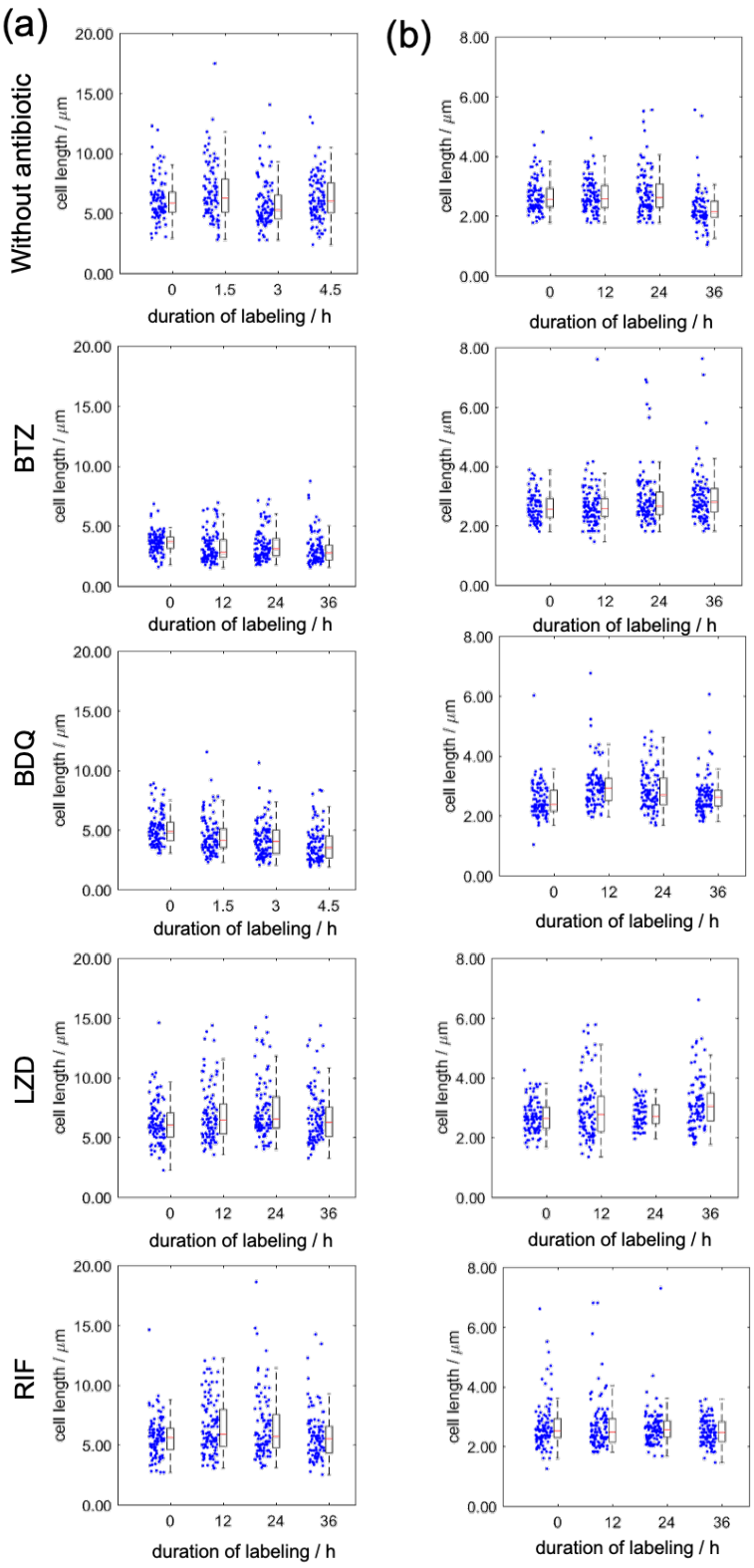

Figure 4.13 Bacterial length of *M. smegmatis* (a) and *M. tuberculosis* (b) in the presence of different conditions.

For the observation of metabolic heterogeneity in individual cells, the CD / CH distribution in *M. tuberculosis* is also plotted along the long axis of individual cells in Figure 4.12. The deuterated molecules are still in higher amounts at the two bacterial poles and expand to the bacterial middle. However, the CD / CH distribution in *M. tuberculosis* cells is not as clear as the CD / CH in *M. smegmatis*. This is because the spatial resolution of normal confocal Raman microscopy is not enough for very small bacteria. When bacteria were exposed to different antibiotics, the inhibitory effect of each antibiotic on bacterial metabolism is obvious, but the effect on the size of the bacteria is not as obvious as the change in the size of *M. smegmatis*, bacterial length in different conditions was calculated and shown in Figure 4.13. The bacterial length was calculated from the CD / CH maps, length of the longest axis in each CD / CH map was calculated as bacterial length. In the control group (Figure 4.12a), significant differences between the bacterial two poles and the middle were observed. However, this heterogeneity is not that obvious in the presence of antibiotics (Figure 4.12b-e). For *M. tuberculosis*, bacterial cells are quite sensitive to BDQ. It can hardly observe the enhancement in CD / CH with increasing incubation time in the presence of D_2O. This means that *M. tuberculosis* becomes inactive in the presence of BDQ. It is not sure if the bacteria have been killed, because mycobacteria can transition to a dormant state to protect themselves from antibiotics. Compared to the other antibiotics (RIF, BDQ, and LZD), BTZ has a smaller decrease in CD / CH with increased incorporation time. That means *M. tuberculosis* is less sensitive to BTZ.

4.2 Kinetic and Mechanistic Investigation of the Photocatalyzed Reduction of 4-Nitrothiophenol

4.2.1 Silver plasmonic film (AgPF) fabrication

It is shown in Figure 4.14a that silver nanoparticles (AgNPs) wrapped around the upper aqueous phase in a hydrophobic container, signify the self-assembly of AgNPs at LL interface during the synthesis process of the AgPF. A fraction of the ensuing metal liquid like film (MeLLF) picked up by a circular piece of double side adhesive tape (diameter: 7 mm) is shown in Figure 4.14b, illustrating a stable homogeneous AgPF. The absorbance spectra of the MeLLF compared to that of AgNPs is shown in Figure 4.14c, where a shift from the LSPR of AgNPs can be seen from 405 nm to 436 nm. The red shift indicates the formation of the MeLLF. Figure 4.14d shows a scanning electron microscopy (SEM) image of the AgPF, illustrating that AgNPs are closely packed on the

adhesive tape. The preparation of AgPF is sketched in Figure 4.15. Atomic force microscopy (AFM) images are shown in Figure 4.16, revealing a surface roughness of the AgPF of 1.88±0.28 nm. To assess the SERS uniformity of the AgPF, the SERS signal from two randomly selected areas were detected using 4-Mercaptobenzoic acid (4-MBA) on the AgPF as a Raman probe. The two Raman images (at band 1585 cm^{-1}) in Figure 4.17 demonstrate a good uniform SERS intensity, where the coefficient of variation at the 1585 cm^{-1} band is 11%. The SERS measurement sensitivity was tested on AgPF using 4-Mercaptobenzoic acid (MBA); the SERS signals shown in Figure 4.18 are indicative that the close packing of the AgNPs yields good sensitivity for Raman active molecules. This simple method of preparing the AgPF requires only 2 hours, which is less time intensive than methods for other substrates, such as the cellulose filter membrane dipping method of Zheng et al.[11]

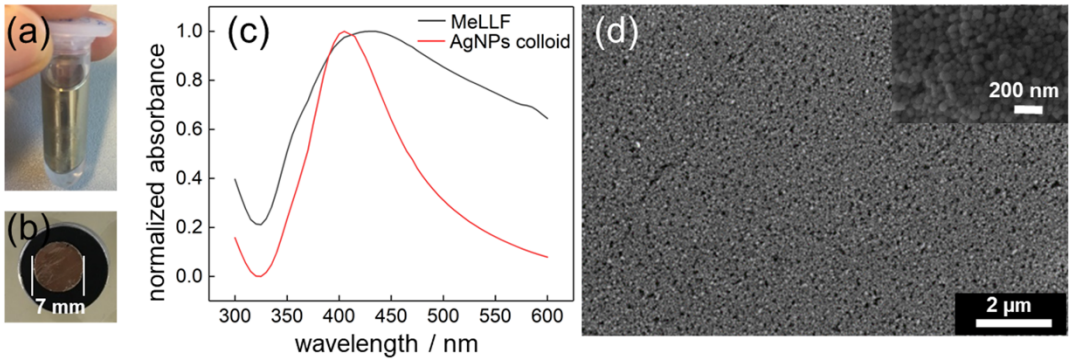

Figure 4.14. Photos of MeLLF formed in a 2 mL centrifugation tube (a) and AgPF (b). (c) UV-vis absorption spectra of AgNPs colloid solution (red line) and MeLLF (black line). (d) SEM image of AgPF. (Inset: highly magnified SEM image of the AgPF, scale bar 200 nm)

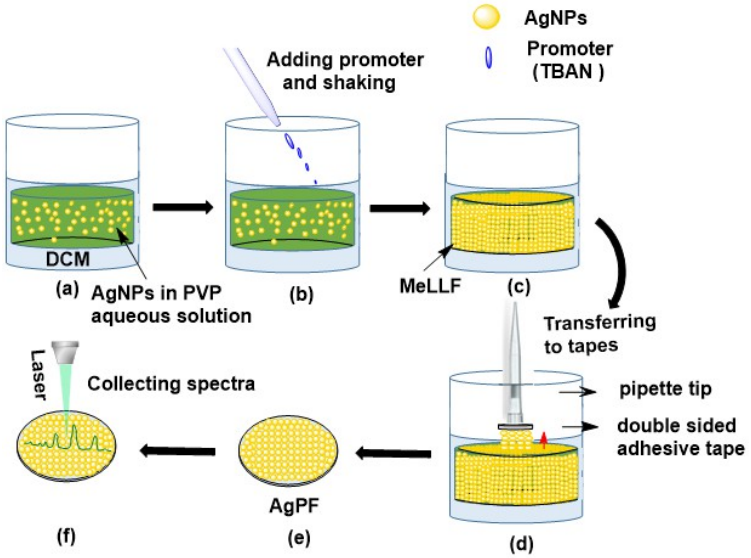

Figure 4.15 Schematic diagram showing the metal-like liquid film (MeLLF) formation and its transformation in the fabrication of the AgPF. (a) The mixture of aqueous phase and DCM organic phase. (b) Addition of TBAN which is used as promoter. (c) The formation of MeLLF. (d) The double-sided adhesive tape-assisted film transposition process. (e) As-prepared AgPF. (f) SERS monitoring of chemical reaction.

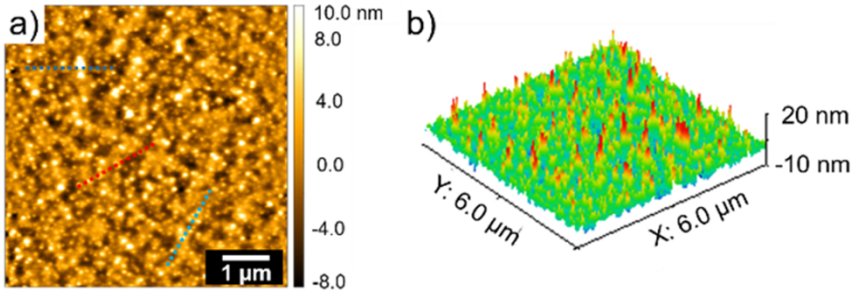

Figure 4.16 AFM characterization of AgPF. (a) 2D image (the blue, red, and light blue lines on the image are used for the calculation of surface roughness). (b) 3D image.

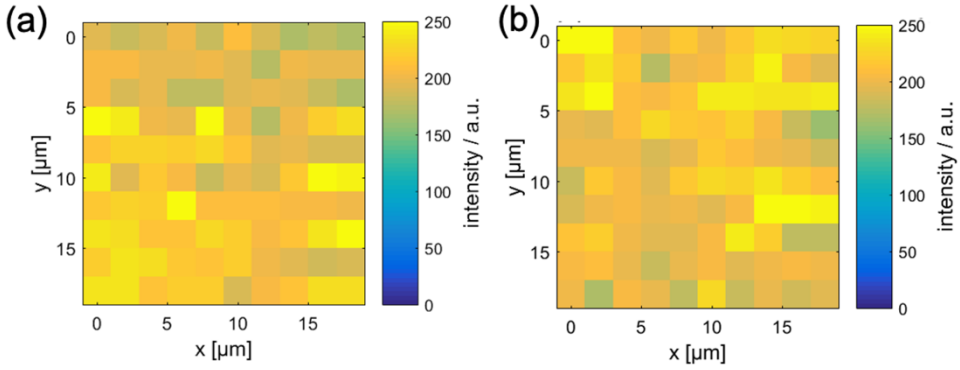

Figure 4.17. SERS images (at 1587 cm^{-1}) of two randomly selected areas (20 × 20 µm) of 4-MBA (10^{-4} M) absorbed on AgPF. Laser power of 0.1 mW, integration time of 0.05 s, step size of 2 µm, and excitation wavelength of 532 nm were used for this detection.

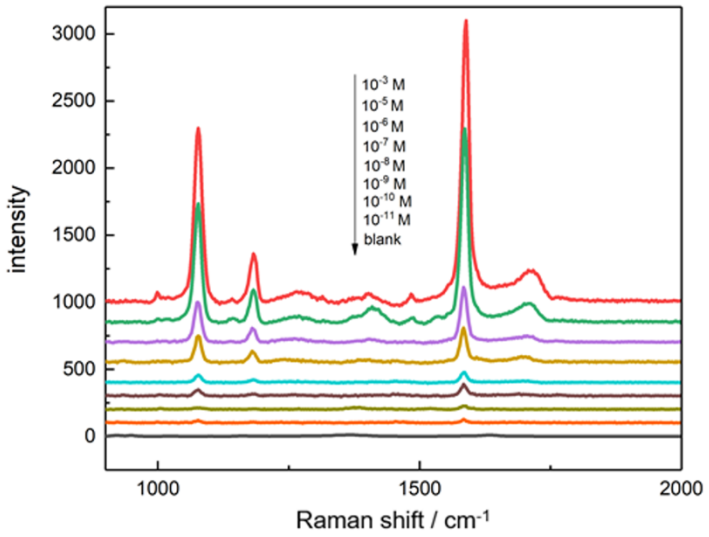

Figure 4.18 SERS spectra measurement of MBA on AgPF substrate with different concentrations to demonstrate the high SERS enhancement sensitivity of our AgPF.

In the SERS experiments of 4-NTP adsorbed on AgPF, the photocatalyzed reduction of 4-NTP can be studied with controlled H^+ and Cl^--concentrations by varying the concentration of HCl or NaCl, respectively, in the aqueous solution placed on the AgPF with adsorbed 4-NTP. The H^+-concentration can also be controlled by using a controlled amount of H_2SO_4 in the aqueous solution on the AgPF. Because the AgPF is dried after the adsorption of 4-NTP, the exact concentration of H^+ and Cl^- ions in the reaction environment is known from the solution properties. The SERS spectra were continuously recorded directly after the addition of the aqueous solution on the AgPF with a time resolution chosen depending on the speed of the reaction under the specific conditions of interest.

4.2.2 Hot-electron-induced dimerization of 4-NTP

The reduction of 4-NTP was first analyzed in the absence of H^+ ions. The SERS spectra at different time intervals after starting the reduction in different environments on the AgPF is shown in Figure 4.19. The formation of DMAB is clearly observed through the emergence of three new SERS bands at 1144 cm^{-1}, 1390 cm^{-1}, and 1432 cm^{-1} (named $\nu DMAB_1$, $\nu DMAB_2$, and $\nu DMAB_3$, respectively). The concentration of DMAB is assumed to be proportional to the intensity of the SERS band, which unless otherwise noted is the SERS intensity at the given wavelength of the band. Results of the 4-NTP reduction in an H^+-free environment where no aqueous solution was

present on the AgPF are shown in Figure 4.19a and 4.19c. In this case, it can be observed that DMAB is formed, although a much smaller amount compared to in the environment with 1 M NaCl (repeated in Figure 4.19b and 4.19d for comparison). It has been previously shown using ultrafast SERS that the dimerization of 4-NTP to DMAB is induced by plasmon-generated hot electrons.[27] Our observations of the formation of DMAB in this H^+-free environment is consistent with this four-electron dimerization. The observation of increased DMAB with the addition of NaCl is consistent with the argument that halide ions (Cl^-, Br^-, I^-) have been proven to recycle the hot-electron generation during the photoreduction of 4-NTP via Ag substrate.[18, 28] This azobenzene species is one of the intermediates during the condensation pathway of aromatic nitro compounds to its corresponding anilines.[20, 21, 25] In the absence of H^+ ions, the formation of 4-ATP is not observed, which is commonly observed at a SERS bands at 1595 cm^{-1}. Table 4.2 summarizes the expected SERS bands for 4-NTP, DMAB, and 4-ATP, and the key SERS bands are also marked in Figure 4.19 as well as all subsequent figures of Raman spectra.

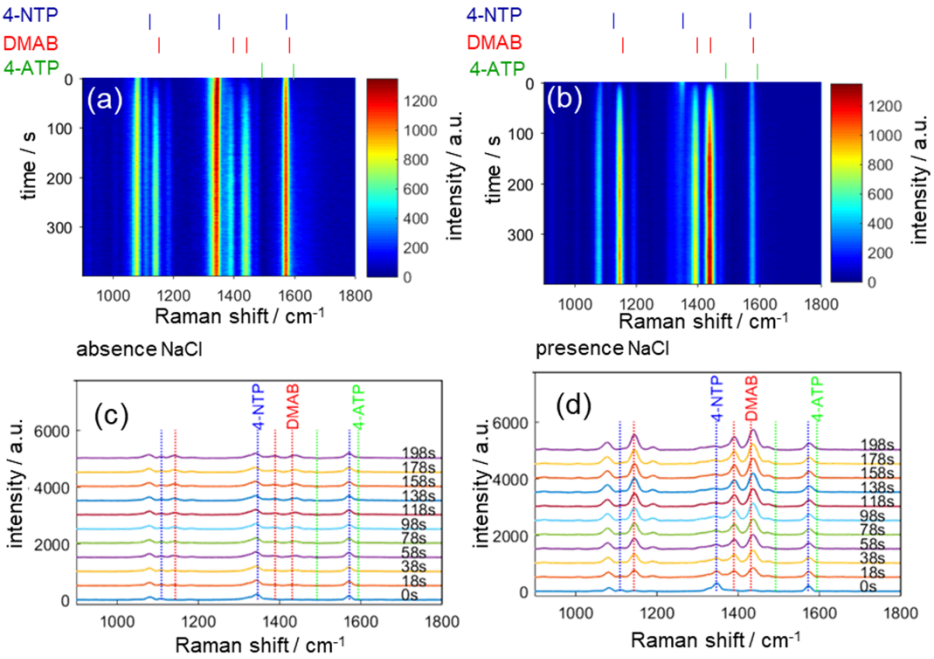

Figure 4.19 Continuous time-dependent spectra of the SERS spectra recorded during the reduction of 4-NTP in (a) dry conditions (absence of NaCl), and in (b) presence of NaCl (1 M) solution. Both cases are with 0 M HCl. (c), (d) The corresponding SERS spectra at discrete time points. In both cases (absence and presence of NaCl), the bands at 1144 cm^{-1}, 1390 cm^{-1}, and 1432 cm^{-1} (ν_{DMAB1}, ν_{DMAB2}, and ν_{DMAB3}) are formed, and the band at 1595 cm^{-1} (ν_{ATP}) is not visible. The measurements were carried out with a laser power of 0.5 mW and 1s integration time.

Table 4.2 The representative bands assignment of the SERS spectra during the reduction. [13, 134-136]

Assignment	Raman shift (cm^{-1})		
	4-NTP	DMAB	4-ATP
Phenyl ring mode	1083	1087	1081
C-N symmetric stretching		1144(ν_{DMAB1})	
N-O stretching	1346 (ν_{NTP1})		
N=N stretching		1390 (ν_{DMAB2})	
C-H in-plane bending mode		1432 (ν_{DMAB3})	
Stretching coordinate of the benzene	1573 (ν_{NTP2})	1575	1595(ν_{ATP})

4.2.3 H^+-concentration-dependent reduction of 4-NTP

Another SERS experiment of the 4-NTP reduction was carried out in excess H^+ ions. To start the photocatalytic reaction under these conditions, 100 µL aqueous solution containing 0.1 M HCl and 1 M NaCl were applied on AgPF as a hydrogen source and to promote hot-electron generation, respectively. The corresponding time-resolved SERS spectra are shown in Figure 4.20. We observe that the band intensities at 1346 cm^{-1} (ν_{NTP1}) and at 1573 cm^{-1} (ν_{NTP2}), corresponding to the stretching vibration of the R-NO_2 group and the stretching vibration of the benzene ring in the 4-NTP molecule, respectively, gradually decrease. At the same time, the band at 1595 cm^{-1} (ν_{ATP}), assigned to the phenyl ring modes in the 4-ATP, appears and increases in intensity. The time-resolved intensities of the SERS bands corresponding to 4-NTP and 4-ATP at νNTP_2 and ν_{ATP}, respectively, are shown in Figure 4.20c. The 4-NTP intensity time history follows an exponential decay, as shown through the exponential fit shown in Figure 4.20c, indicating that under these conditions the 4-NTP reduction is a pseudo-first-order reaction. The time-resolved intensity corresponding to 4-ATP also increases as would be expected assuming it is the product of the 4-NTP reduction with rapidly reacting intermediates. This is shown through the fit in Figure 4.20c, which shows that the rate of 4-NTP depletion is approximately equal to the rate of 4-ATP formation. These results agree well with previous reagent-induced ($NaBH_4$ and H_2) studies,[11, 29] indicating that low-cost AgPF performs comparably to other SERS substrates used for observing the 4-NTP to 4-ATP reaction. There is no observation of SERS bands corresponding to DMAB, as expected based on the results of previous studies with similar reaction conditions.

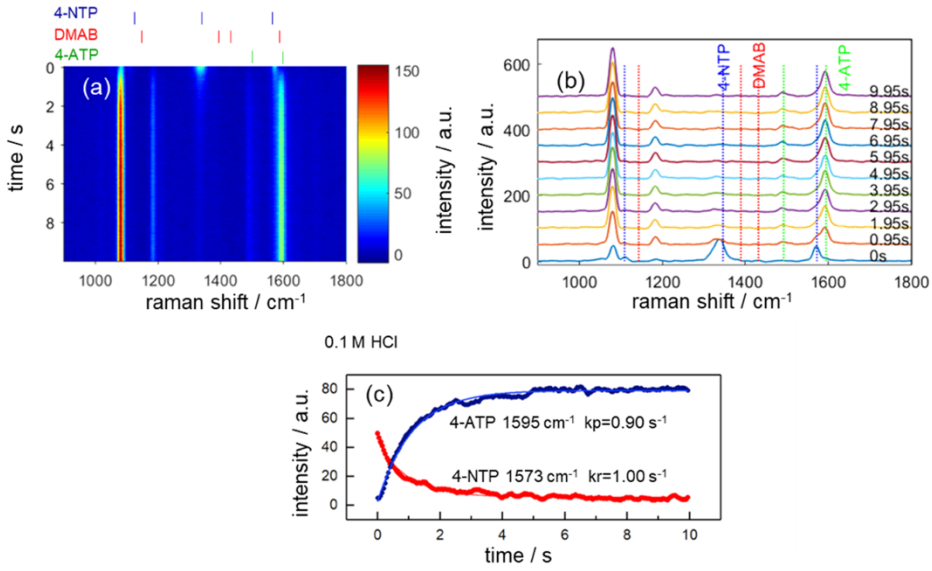

Figure 4.20 Results for conditions of 1 M NaCl and 0.1 M HCl concentration. (a) Continuous time-dependent spectra of the SERS spectra. (b) Corresponding SERS spectra at discrete time points. (c) SERS intensities over time at 1573 cm-1 (ν_{NTP2}) and 1595 cm-1 (ν_{ATP}). Exponential fits to the data are drawn and the respective exponential rates is shown.

To determine how the reaction progresses in environments with intermediate H^+-concentration, the reduction of 4-NTP was monitored with successively lower H^+-concentrations by using six different concentrations of HCl from 0.01 M to 0.0001 M in the 100 µL droplet, while maintaining a fixed concentration of 1 M of NaCl. This varied the H^+-concentration while keeping the concentration of Cl^- nearly constant (the contribution of HCl to the overall Cl^--concentration is in all cases1 % or less). An example of time-resolved SERS spectra of the 4-NTP reduction with 0.001 M HCl is shown in Figure 4.21a. It can be clearly seen that the three SERS bands at 1144 cm^{-1}, 1390 cm^{-1}, and 1432 cm^{-1} (ν_{DMAB1}, ν_{DMAB2}, and ν_{DMAB3}, respectively) are clearly visible at early reaction times, and their intensities gradually decrease over time. Moreover, a clear band shift from the initial 4-NTP band at 1346 cm^{-1} (ν_{NTP1}) to 1334 cm^{-1} can be observed during the reaction process. This shift was not observed in the reaction conditions without H^+ ions, nor was it be seen in excess H^+-concentration. Figure 4.21a marks this shift at 1334 cm^{-1} (which we denote as ν_{I2}) with a purple line. A similar red shift has also been observed by Choi et al.[137], who assumed that this was caused by the appearance of the 4-NTP anion radical ($NTP^{\bullet-}$) intermediate from the first elementary step of one electron transfer. We observe a shift of 11 cm^{-1}, compared to their 6 cm^{-1}. The appearance of an intermediate, hereafter denoted by I2, with a strong SERS band so close to ν_{NTP1} prevents the direct correlation of the concentration of the respective species to the

SERS intensity at the wavenumber of the band. Therefore, to characterize the concentration of 4-NTP and I2, a six-parameter double Lorentzian is performed fit to the SERS spectra between 1310 cm^{-1} and 1360 cm^{-1}, fixing the center of the Lorentzian functions at 1346 cm^{-1} and 1334 cm^{-1}, for 4-NTP and I2, respectively. An example of the double Lorentzian fitting to the SERS spectra is shown in Figure 4.21b. The concentration of 4-NTP and I2 is assumed to be proportional to the magnitude of the respective Lorentzian function. The time-resolved behavior of the concentration of 4-NTP, I2, and DMAB for the condition of 0.001 M HCl are shown in Figure 4.21c. The inset of Figure 4.21c enlarges the first 100 seconds of the reaction, showing that both I2 and DMAB are quickly formed then depleted.

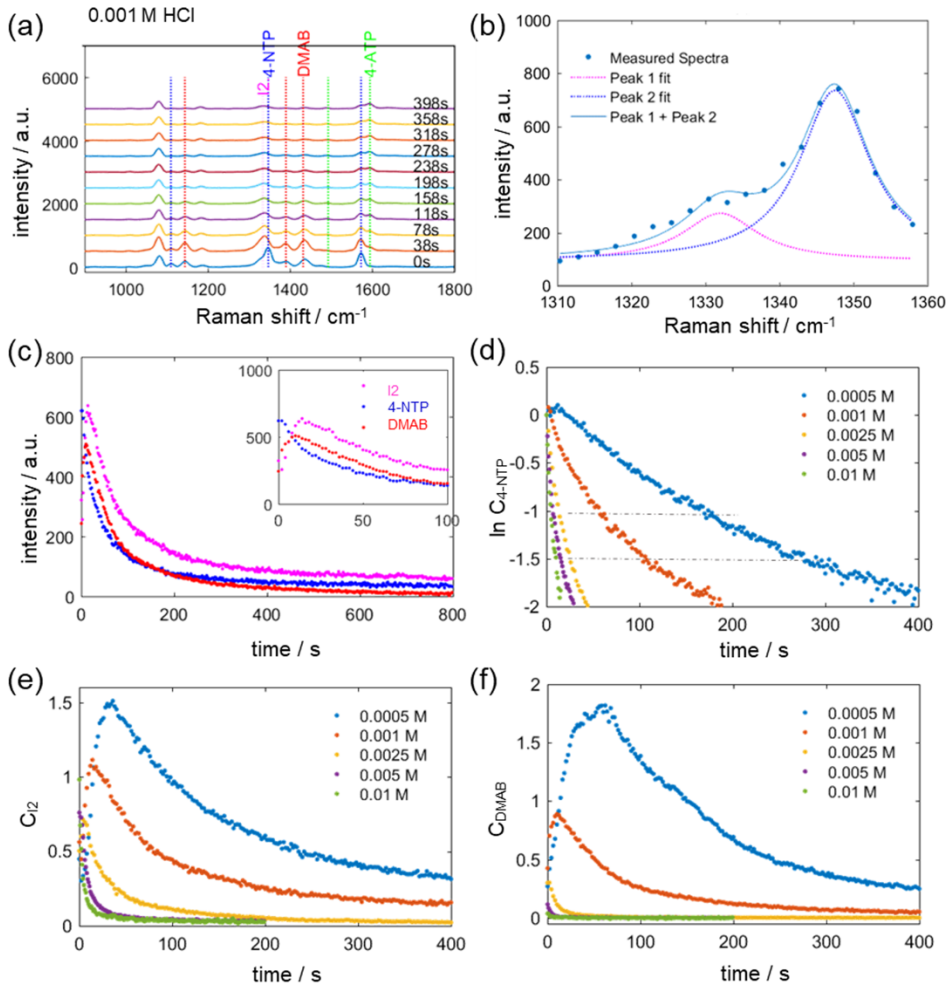

Figure 4.21 (a) Overall SERS spectra measured in conditions of 0.001 M HCl and 1 M NaCl concentration in the aqueous solution at different times after starting the reaction and SERS measurement. (b) SERS at time 0 s showing the wavenumber range where two SERS bands ν_{NTP1} and ν_I are present. The individual SERS bands for ν_I (red, Peak 1) and ν_{NTP1} (blue, Peak 2) determined with a double Lorentzian fit are shown as well as the sum (Peak 1 + Peak 2). (c) The SERS intensities over time at 1334 cm^{-1}, 1346 cm^{-1} and 1432

cm^{-1} corresponding to I2, 4-NTP, and DMAB, respectively. The inset enlarges the first 100 seconds of the reaction. (d-f) Normalized concentration profiles (as described in the text) corresponding to 4-NTP, I2, DMAB, respectively as a function of time at different reaction H^+- concentration (0.0005 M, 0.001 M, 0.0025 M, 0.005 M, 0.01 M). The SERS intensities in each case were normalized to the initial 4-NTP intensity. The grey parallel lines in (d) mark values where the intensity of the 4-NTP band is e^{-1}, $e^{-1.5}$, and e^{-2} of its initial value.

A comparison of the time-resolved concentrations of 4-NTP, I2, and DMAB for the reaction in different HCl concentrations (0.0005 M, 0.001 M, 0.0025 M, 0.005 M, 0.01 M) is shown in Figure 4.21d-f, respectively. Each concentration, represented as C in arbitrary units, is represented by the respective Lorentzian magnitude (for 4-NTP and I2) or SERS intensity (for DMAB), normalized by the initial value of 4-NTP. Figure 4.22 and 4.23 show the corresponding time-dependent SERS spectra for all the HCl concentrations investigated.

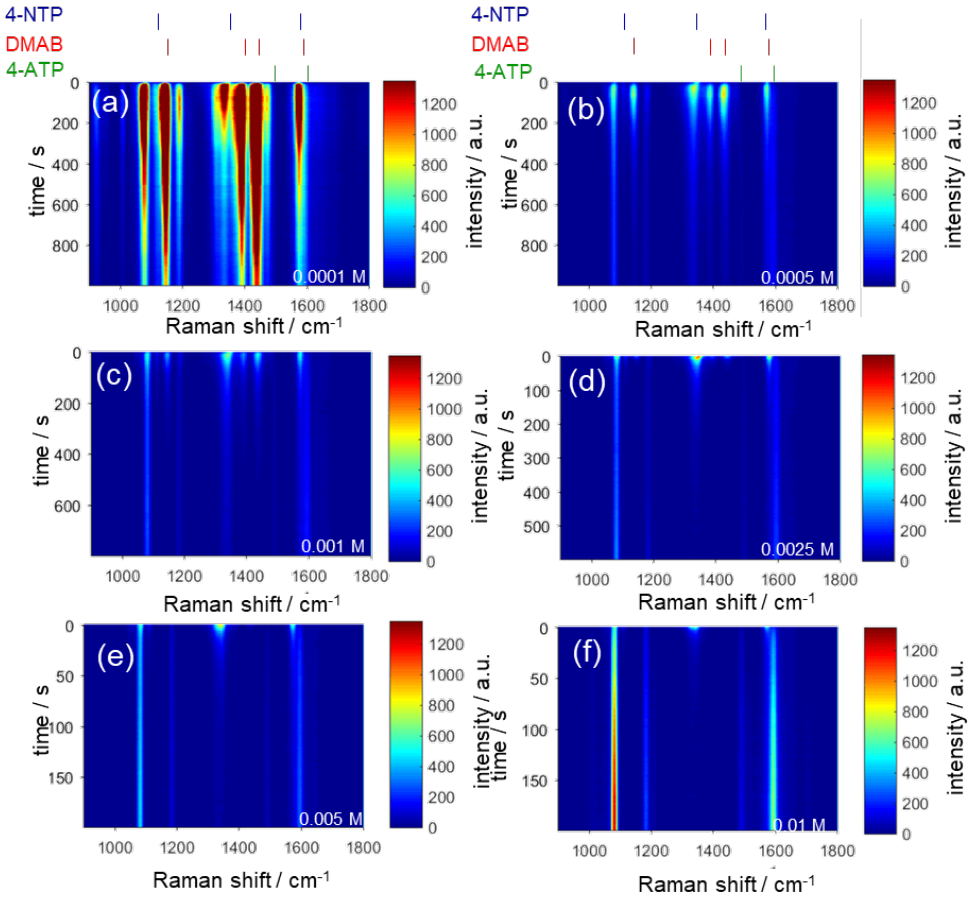

Figure 4.22 Continuous time-dependent spectra of the SERS spectra for the reduction of 4-NTP in reaction conditions of different HCl concentration (0.0001M, 0.0005M, 0.001M, 0.0025M, 0.005M, 0.01M, in a-f, respectively). The NaCl concentration in all cases is 1M.

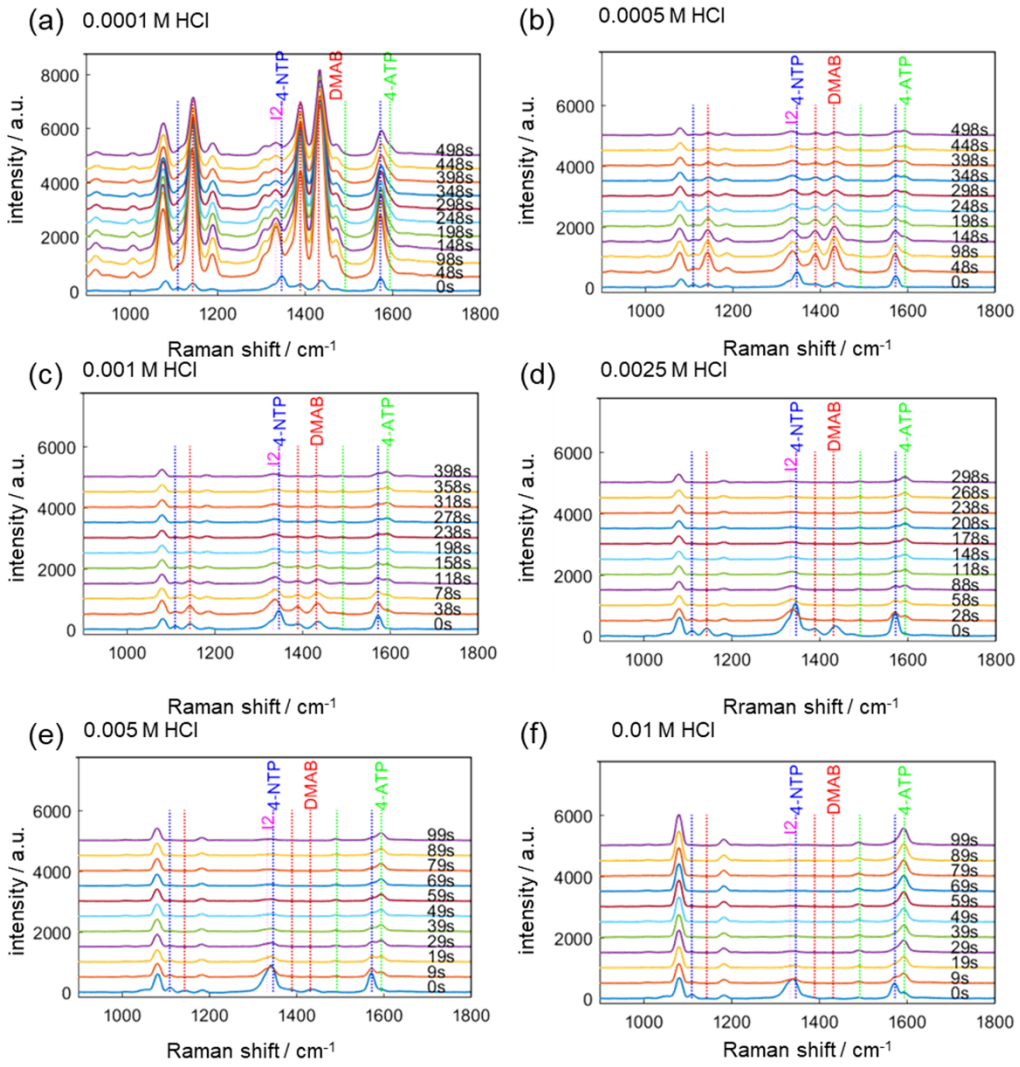

Figure 4.23 SERS spectra at discrete time points during the reduction of 4-NTP in reaction conditions of different HCl concentration (0.0001M, 0.0005M, 0.001M, 0.0025M, 0.005M, 0.01M, in a-f, respectively). The NaCl concentration in all cases is 1M.

The lowest HCl concentration (Figure 4.22a and Figure 4.23a) investigated exhibits very high SERS intensity (in comparison to the other conditions) around the bands ν_{NTP1}, ν_{I2} ,ν_{DMAB1}, ν_{DMAB2}, and ν_{DMAB3} with no clear baseline to be detected, indicating the possible appearance of additional intermediates not considered in the analysis for the other HCl concentrations. As a result, our double Lorentzian fitting could not be applied to this data, and no conclusive information on time-resolved species concentration could be obtained for the concentrations of HCl $\leq$ 0.0001 M. The time-resolved 4-NTP concentration for all the other HCl concentrations studied is shown through the natural logarithm of its value in Figure 4.21d to illustrate that the decay of the reactant follows

a near-exponential function (where a perfect exponential would be linear in Figure 4.21d). At low H^+-concentrations, there is some deviation from the exponential decay, possibly indicating deviation from the pseudo-first order approximation as the change in H^+-concentration may not be negligible during reaction. The concentration of 4-NTP can be clearly seen to decrease faster with higher H^+-concentration, indicating that the first step in the reaction mechanism is dependent on H^+-concentration. For the same initial amount of initial 4-NTP, the maximum concentrations of I2 and DMAB are both higher for lower H^+-concentration (Figure 4.21e-f). At concentrations of HCl > 0.001 M, negligible DMAB is observed, whereas I2 was observed in all conditions (though the peak concentration decreases with increasing HCl concentration, indicating that at some HCl concentration limit no I2 will be observed), with a rate of decay that appears to increase with increasing H^+-concentration. For all H^+-concentrations investigated, the time of the peak DMAB concentration generally occurs before the time of the peak I2 concentration. This suggests that I2 is not a precursor to DMAB, and based on the reaction mechanism shown in Scheme 1, this means that I2 does not contain two oxygen molecules. This indicates that the intermediate that we observe is not the 4-NTP anion radical ($NTP^{\bullet-}$) as suggested by Choi et al.[137] According to our measurements, I2 must be formed through a separate reaction pathway from the pathway producing DMAB, and we proposed the reaction mechanism shown in Scheme 4.1. Our data supports that intermediates I2 and DMAB are formed in two separate parallel pathways and they have a same intermediate precursor (denoted by I1). This mechanism is also consistent with the previous data in an H^+-free environment and in excess H^+ ions. In the H^+-free, no reaction occurred via the direct path (Pathway 1), therefore no I2 was formed and no red shift was observed near ν_{NTP1} (Figure 4.19). In excess H^+ ions, where no DMAB was observed, the reaction occurs primarily via the direct path, but the depletion of I2 is rapid due to the high H^+-concentration, therefore no I2 was observed and no red shift was observed near ν_{NTP1} (Figure 4.20b). In the cases of no red shift near ν_{NTP1}, the concentration of 4-NTP can be represented by the SERS intensity at ν_{NTP1}.

Scheme 4.1. Proposed reaction mechanism of the photoreduction of 4-NTP based on the current experimental observations. The direct pathway is the top row of reactions (k2 and k3) and the indirect pathway is the bottom branch (k4 and k5).

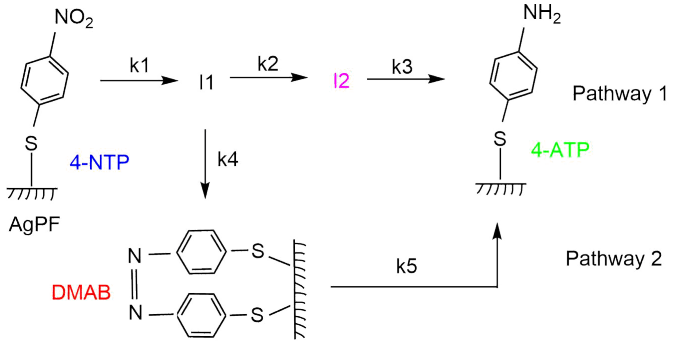

4.2.4 Numerical Simulation of Reaction Mechanism

Definition of reaction rate and rate constants

Scheme 4.1 describes a reaction mechanism with the following reactions:

4-NTP	→	I1	(k1)
I1	→	I2	(k2)
I2	→	4-ATP	(k3)
2I1	→	DMAB	(k4)
DMAB	→	2(4-ATP)	(k5)

The time-resolved concentrations of 4-NTP, I2, and DMAB according to this mechanism were computed numerically assuming that all of the reactions are elementary, which means the rate of the reaction is proportional to the product of the concentration of the reactants, and the proportionality constants are the respective rate constants (which label the reactions above). The derivative of each species concentration in time was set as the contribution from all reaction rates as follows:

$$\frac{\partial}{\partial t}[\mathrm{4NTP}] = -k1[\mathrm{4NTP}]$$

$$\frac{\partial}{\partial t}[\mathrm{I1}] = k1[\mathrm{4NTP}] - k2[\mathrm{I1}] - 2k4[\mathrm{I1}]^2$$

$$\frac{\partial}{\partial t}[\mathrm{I2}] = k2[\mathrm{I1}] - k3[\mathrm{I2}]$$

$$\frac{\partial}{\partial t}[\mathrm{DMAB}] = k4[\mathrm{I1}]^2 - k5[\mathrm{DMAB}]$$

To solve the simulated species concentrations in time, the derivatives were solved numerically in Matlab using a finite difference approximation with time step of 5 ms. The initial conditions were set that the reaction occurred with respect to a concentration of unity for 4-NTP.

The reaction rate constants of the individual reactions in Scheme 4.1 can be determined from the kinetic traces shown in Figure 4.21d-f. We simulated the time-resolved concentration profiles according to the mechanism in Scheme 4.1 numerically, assuming that each reaction depicted is an elementary reaction (indicating that the reactions corresponding to k1, k2, k3, and k5 are first order, or pseudo-first order if the rate constant depends on the H^+ concentration which is assumed to be in excess, and the reaction corresponding to k4 is second order). Based on this numerical simulation of the mechanism, the sensitivity (S_i) of each time-resolved species concentration to reaction n is numerically computed, defined as $S_i = (\partial x_i/\partial k_n) * (k_n/x_i)$ for each species i (where i = 4-NTP, I2, or DMAB and x_i refers to the corresponding species concentration). All the calculations are shown in Figure 4.24. The 4-NTP sensitivity shown in Figure 4.24 proves that the rate constant of the first step (k1) can be determine through the kinetic trace of 4-NTP alone (as the concentration of 4-NTP is only sensitive to k1). To determine the rate constant k1, an exponential decay was fit to the kinetic traces of 4-NTP, using only the initial data before the reaction deviated too much from the pseudo-first order assumption. Figure 4.25 shows the determined values for k1 at the different HCl concentrations investigated, where k1 is the rate of exponential decay of a least squares exponential fit to the 4-NTP kinetic trace using all data points until the concentration of 4-NTP reached $e^{-1.5}$ times its initial value. The error bars indicate the dependence of k1 on the number of data points used for the exponential fitting, where the upper limit uses all data until the concentration of 4-NTP reached e^{-1} times its initial value, and the lower limit uses all data until the concentration of 4-NTP reached e^{-2} times its initial value. As in all analysis of a pseudo-first-order reaction, the reaction will deviation from pseudo-first-order behavior at longer times, therefore, a limit to the points used for the fitting was needed. The error bars thus are partly an indication of the deviation of the reaction from pseudo first order. As can be seen from Figure 4.25, the rate constant k1 depends linearly on the H^+-concentration, suggesting

that one H^+ ion is involved in the reaction of 4-NTP to form I1, not two as suggested by the initial reaction step shown in Scheme 2.1.

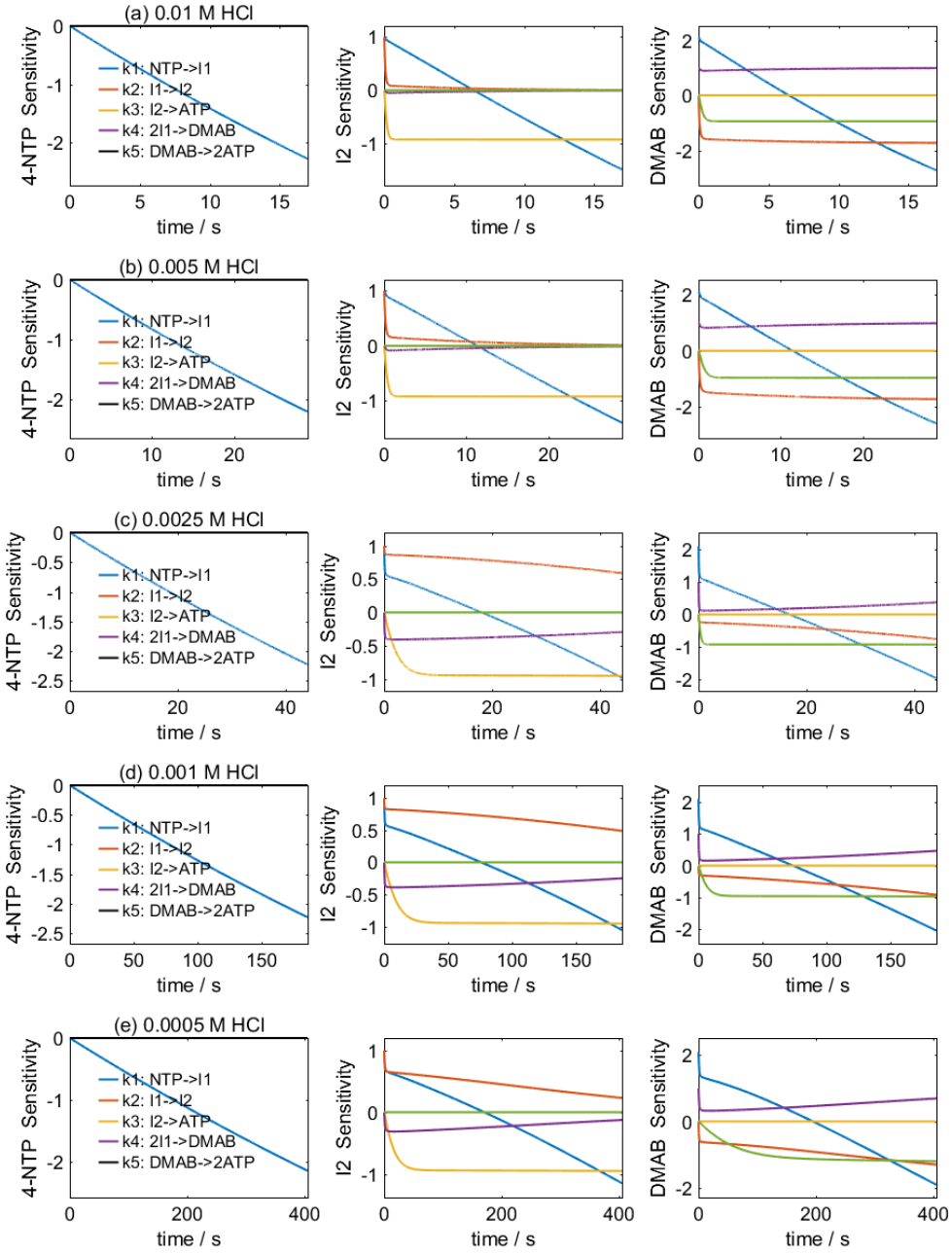

Figure 4.24 Time-resolved sensitivity of the concentration of 4-NTP, I2, and DMAB (left to right) to the different rate constants in the reaction mechanism computed numerically with the rate constants determined with the least squares fitting procedure for different concentrations of HCl (0.01M, 0.005M, 0.0025M, 0.001M, 0.0005M in a-e, respectively).

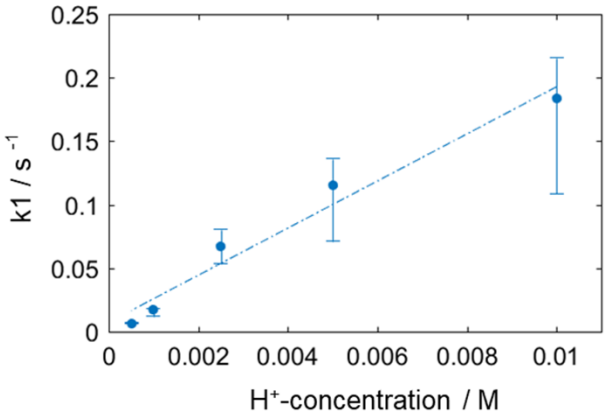

Figure 4.25 Reaction rate constant k1 for the initial step in the reduction of 4-NTP. A linear fit is shown illustrating that k1 depends linearly on H^+-concentration.

The determination of k2 to k5 is more complex, because the concentration of I2 and DMAB have a complex dependence on these rate constants as seen in Figure 4.24. These rate constants were determined through a fit to a numerical simulation of the mechanism shown in Scheme 4.1, with the detailed procedure for the rate constant determination described in the following section.

Procedure to determine Raman cross sections and reaction rate constants from measured kinetic traces

Certain assumptions were made to fit the measured kinetic traces of I2 and DMAB from Figure 4.21e-f, respectively, to a numerical simulation of the respective concentration according to the mechanism shown in Scheme 4.1. The data used for all fitting included all data points until the time that the concentration of 4-NTP reached e^{-2} times its initial value. The value for k1 was also assumed to be the exponential decay rate fit to the 4-NTP data in this time. For the determination of the other rate constants, first, a SERS cross section (SERS cross section is expressed as the transverse area that the incident light hits the molecules absorbed on a SERS substrate) for I2 σ_{I2} (relative to the SERS cross section for 4-NTP $\sigma_{4\text{-NTP}}$) was assumed based on the data from 0.01 M HCl, where negligible DMAB was observed. The SERS cross section was needed to determine the concentration through $x=C/\sigma$. For the determination of σ_{I2} a least squares three-parameter fit ($\sigma_{I2}/\sigma_{4\text{-NTP}}$, k2, k3) was performed numerically to match the simulated I2 concentration to the measured I2 kinetic trace. This was done because for these conditions, the I2 concentration is only sensitive to k2 and k3 (see Figure 4.24). The results indicate that $\sigma_{I2}/\sigma_{4\text{-NTP}}$ must be greater than or equal to 50 to reasonably fit the measured I2 kinetic trace. A value of 50 was assumed for $\sigma_{I2}/\sigma_{4\text{-}}$

$_{NTP}$ which was kept constant for all other concentrations of HCl, though a subsequent analysis with $\sigma_{I2}/\sigma_{4\text{-}NTP} = 100$ supports the conclusion that the final trends of the rate constant determination is not highly sensitive to the value of $\sigma_{I2}/\sigma_{4\text{-}NTP}$ assumed. Using $\sigma_{I2}/\sigma_{4\text{-}NTP} = 50$, a value for $\sigma_{DMAB}/\sigma_{4\text{-}NTP} = 60$ was determined, and this is relatively insensitive to the value of $\sigma_{I2}/\sigma_{4\text{-}NTP}$ assumed (a factor of 2 change in $\sigma_{I2}/\sigma_{4\text{-}NTP}$ only changes $\sigma_{DMAB}/\sigma_{4\text{-}NTP}$ by 25%). While this relative SERS cross section for DMAB is larger than the relative Raman cross section estimated through theoretical calculations by Choi et al.[137,138], who suggested $\sigma_{DMAB}(1432\ cm^{-1})/\sigma_{4\text{-}NTP}(1346\ cm^{-1}) = 3.7$, it was found that using this Raman cross section ratio as the SERS cross section ratio suggested a relative concentration of DMAB that was far too high to be fit by our suggested mechanism in Scheme 2. Our determination of $\sigma_{DMAB}/\sigma_{4\text{-}NTP}$ is, however, consistent with the conclusion of Choi et al. that DMAB is significantly more Raman active than 4-NTP (at the respective wavenumbers of interest). From our 3-parameter fit, we were also able to determine k2 and k3 for the aforementioned conditions of 0.01 M HCl. We made the assumption that k2 is linear with respect to the H^+-concentration, as the formation of I2 is clearly slower with lower H^+-concentration (see Figure 4b where for high H^+-concentration, I2 is formed immediately, and for low H^+-concentration, I2 gradually forms) indicating that this an H^+ ion could be involved during the course of the reaction. With this, we could determine the value of k2 for all concentrations of HCl. With this additional assumption, a two-parameter fit (k3, k4) to the I2 kinetic trace for 0.0005 M HCl was carried out to determine k3 and k4 (because I2 is sensitive to k1, k2, k3, and k4, but k1 and k2 were previously determined). Using these same conditions of 0.0005 M HCl, we determined a value for the Raman cross section for DMAB σ_{DMAB} (relative to the Raman cross section for 4-NTP $\sigma_{4\text{-}NTP}$) from a two-parameter fit ($\sigma_{DMAB}/\sigma_{4\text{-}NTP}$, k5) to the DMAB kinetic trace. We determined that with, our assumptions, $\sigma_{DMAB}/\sigma_{4\text{-}NTP} = 60$, and this is relatively insensitive to the value of $\sigma_{I2}/\sigma_{4\text{-}NTP}$ assumed (a factor of 2 change in $\sigma_{I2}/\sigma_{4\text{-}NTP}$ only changes $\sigma_{DMAB}/\sigma_{4\text{-}NTP}$ by 25%). After our determination of $\sigma_{DMAB}/\sigma_{4\text{-}NTP}$, we obtained k3, k4, and k5 for the remaining HCl conditions through a least squares 3-parameter fit to the I2 and DMAB kinetic traces. In this case, the least squares minimization was the sum of squares of the residuals from both traces. For the 0.01 M HCl concentration, where k2 and k3 were already determined, a two-parameter least squares fit (k4, k5) to the measured DMAB kinetic trace (albeit with very low concentration) was carried out to obtain k4 and k5 for these conditions.

The values for k2 to k5 were determined through the abovementioned least squares fitting method, and the results are shown in Figure 4.26. Figure 4.27 shows the numerical computation of the concentrations of 4-NTP, I2, and DMAB using these determined rate constants, compared to the respective measured kinetic traces. It was found that the trends determined in the rate constants shown in Figure 4.26 was not considerably sensitive to the SERS cross section ratio, as shown by the open symbols in Figure 4.26 which were determined with the relative SERS cross section of $\sigma_{I2}/\sigma_{4\text{-NTP}}$ perturbed by a factor of two.

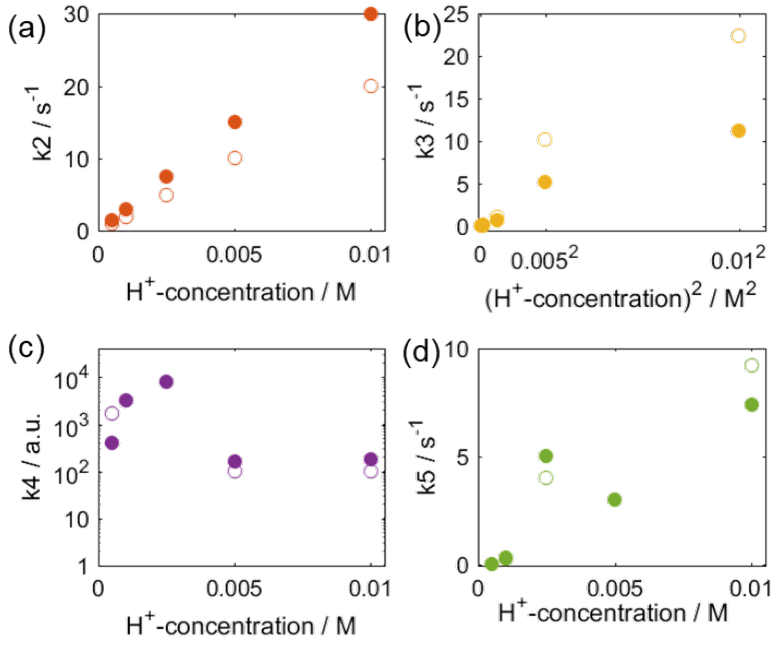

Figure 4.26 Reaction rate constants as a function of H^+-concentration for k2-k5 (a-d, respectively) for the reaction mechanism shown in Scheme 2. Filled symbols represent the rate constants determined with the $\sigma_{I2}/\sigma_{4\text{-NTP}} = 100$ as described in the text. Open symbols represent the rate constants determined with $\sigma_{I2}/\sigma_{4\text{-NTP}}$ perturbed by a factor of 2.

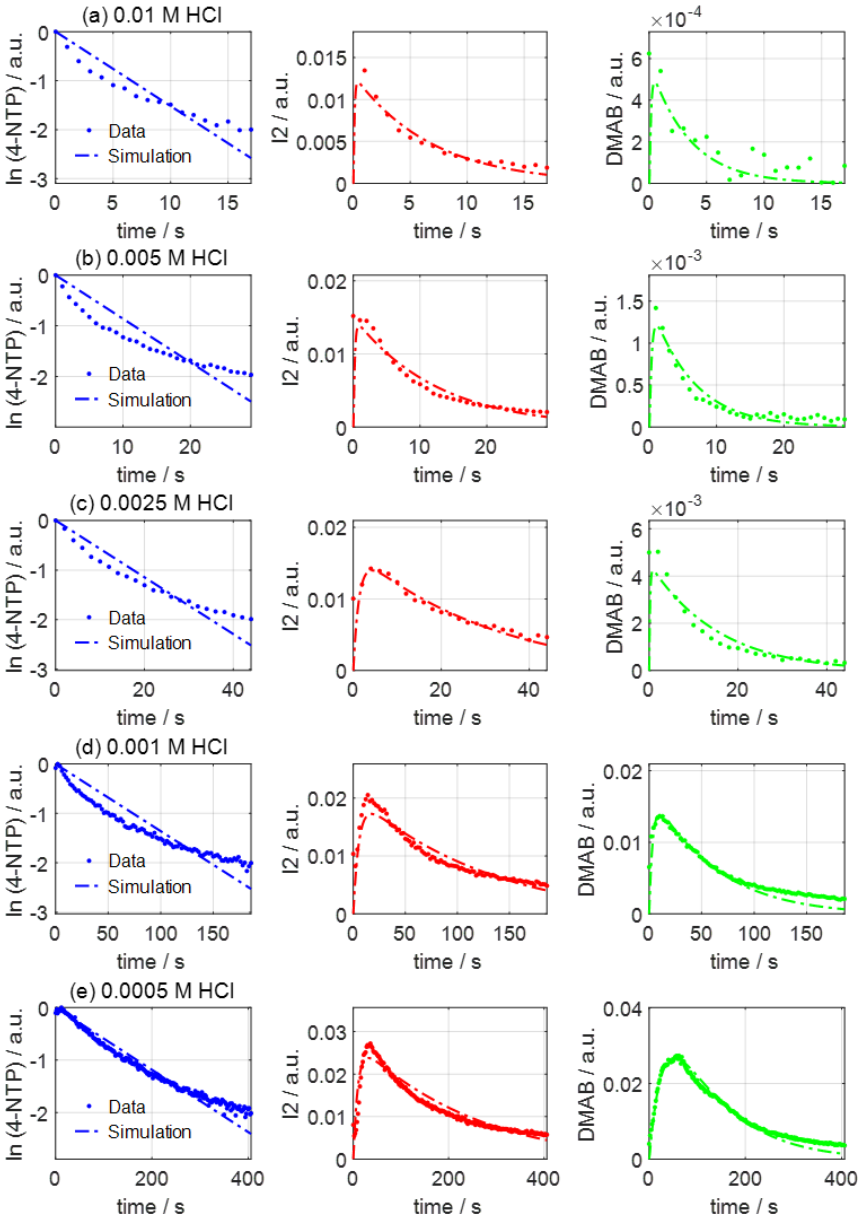

Figure 4.27 Comparison of measured time-resolved concentrations of 4-NTP, I2, and DMAB (left to right) to the respective simulated values using the mechanism in Scheme 2 with the rate constants determined with the least squares fitting procedure for different concentrations of HCl (0.01M, 0.005M, 0.0025M, 0.001M, 0.0005M in a-e, respectively).

From Figure 4.25, we can see that k2 and k5 also increase approximately linearly with increasing H^+-concentration, suggesting that these reactions also consume H^+ ions in the course of the reaction. The reaction rate for k3 appears to have a dependence on the H^+-concentration squared, suggesting that two H^+ ions are involved in the reaction, consistent with the first step in the direct pathway branch shown in Scheme 1. While the magnitude of k2, k3, and k5 have some dependence

on the relative SERS cross section used in the analysis (comparison of the open and filled symbols in Figure 4.25), the linear relationships to H^+-concentration and H^+-concentration squared is independent of the SERS cross section. There does not appear to be a systematic dependence of k4 on the H^+-concentration. It should be noted, however, that this reaction is a second order reaction (requiring two reactant molecules to its dimer), thus the rate of this reaction depends on the initial concentration of the reactants (hence the units of the determined rate constant are arbitrary, based on the initial concentration of 4-NTP), unlike the other reactants that are pseudo-first order. Thus, small changes in the initial concentration of 4-NTP (which could result due to random fluctuations even though the same initial 4-NTP amount is used in the synthesis) could result in changes of the observed reaction rate. Moreover, the sensitivity of both I2 and DMAB to k4 is the lowest compared to sensitivity of the other rate constants, therefore the determination of k4 through these measured kinetic traces is not as precise. It can conclude that with increasing H^+-concentration, the observed concentration of I2 decreases because its depletion (though k3, dependent on H^+-concentration squared) speeds up faster than its formation (through k2, dependent linearly on H^+-concentration). The decreasing observed DMAB seen with increasing H^+-concentration is largely due to the decreasing competition from the direct pathway (through k2) as k2 speeds up with increasing H^+-concentration. Another contributing factor is the increased speed of consumption of DMAB (through k5). It can be concluded that DMAB is a stable product of 4-NTP photoreduction under a relative basic condition on Ag surface. The results of the determined rate constants k2 to k5 support that at high H^+-concentration, the 4-NTP reduction occurs primarily through the direct pathway, and at low H^+-concentration, the indirect pathway with DMAB formation plays a larger role. At H^+-concentrations lower than 0.0005 M, the SERS spectra indicate that other intermediates may be formed (Figure 4.22a and Figure 4.23a) and Scheme 4.1 may not completely describe the reaction mechanism. Additional methods may be needed for molecular species discrimination in order to make conclusion about the reaction mechanism for such low H^+-concentrations**.**

4.2.5 Cl^--concentration-dependent reduction of 4-NTP

To investigate the influence of Cl^- on the reaction, the photoreduction of 4-NTP was investigated under conditions of different NaCl concentration (0 M, 0.5 M, 1 M) with a fixed concentration of 0.005 M H_2SO_4 (0.01 M H^+). The selected SERS spectra and the continuous time-dependent SERS

spectra are shown in Figure 4.28, respectively. In conditions with this fixed H^+-concentration, no DMAB was observed in the previous experiments (indicating that the direct reaction pathway is dominant), and this remains consistent with higher NaCl concentrations as seen in Figure 4.28 b-c and e-f. However, Figure 4.28a and 4.28d shows that a high concentration of DMAB is now observed in the Cl^--free environment (0 M NaCl), and a resulting in a SERS spectra similar to that measured in conditions of low H^+ concentration (<0.0005 HCl, shown in Figure 4.22a and Figure 4.23a). Our results indicate that DMAB production via the indirect pathway becomes more dominant in the absence of Cl^- ions.

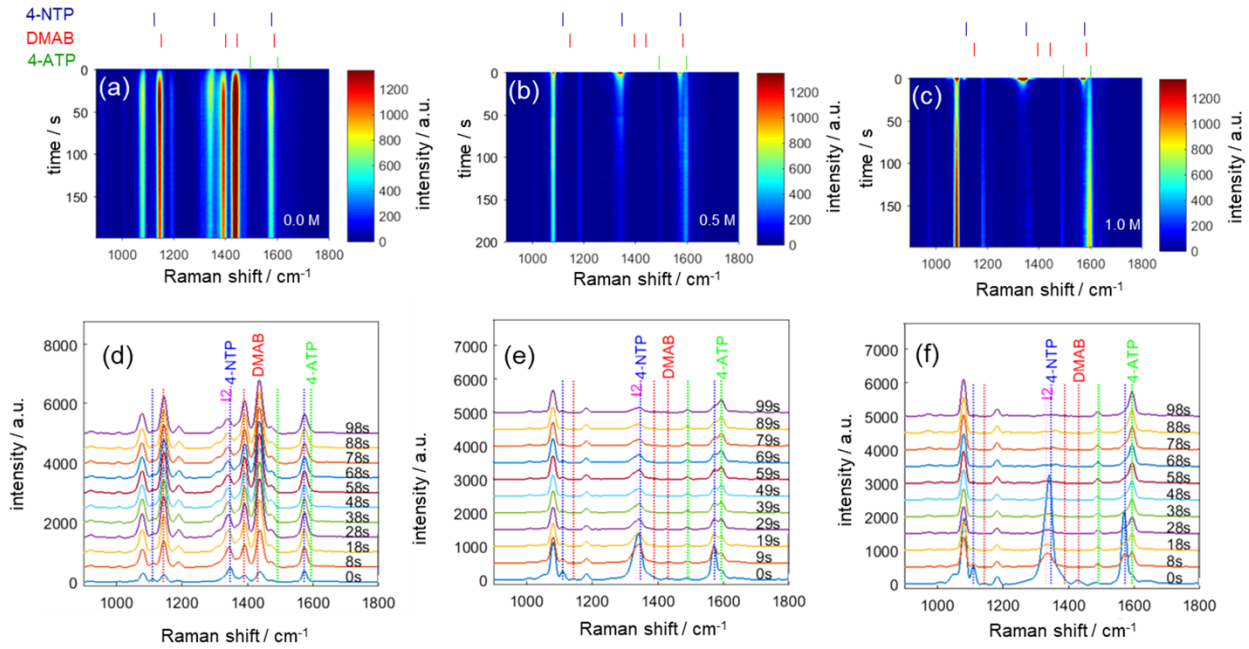

Figure 4.28 Continuous time-dependent spectra of the SERS spectra for the reduction of 4-NTP in reaction conditions with different NaCl concentration (0.0 M, 0.5 M, 1.0 M, a-c, respectively). The H_2SO_4 concentration all cases is 0.005 M. And their corresponding selected spectra from the time-dependent SERS measurement (d-f).

We performed an additional experiment that provides evidence that the presence of Cl^- is necessary for formation of 4-ATP from DMAB. After generation of DMAB formed from the dimerization of 4-NTP after laser illumination, SERS spectra (shown in Figure 4.29) were collected under laser illumination over 600 s after 100 µL H_2O, 0.05 M H_2SO_4, or 0.1 M HCl aqueous solution were dropped on the AgPF. In the presence of water or sulfuric acid, no reduction of DMAB is observed. Only HCl was able to induce the reduction of DMAB (seen through a reduction of the intensity of

the DMAB-related bands after 10 minutes, and the appearance of the 4-ATP band at 1595 cm^{-1}) due to the presence of Cl^-. As described above, halide ions are a key element to cause the formation of 4-ATP from DMAB. This could be explained in that the hot electrons formed in the presence of Cl^- have a higher energy due to the formation of AgCl, which reduces the Fermi level of Ag, increasing the energy of the hot electrons generated.[139,140] As a result, these hot electrons have sufficient energy to overcome the energy barrier to break N=N bond leading to the formation of 4-ATP from DMAB, whereas in the absence of Cl^-, the hot electrons lack sufficient energy for the reaction to proceed. The first generation of hot electrons directly formed by the decay of excited surface plasmons of AgNPs can only reduce 4-NTP to DMAB.

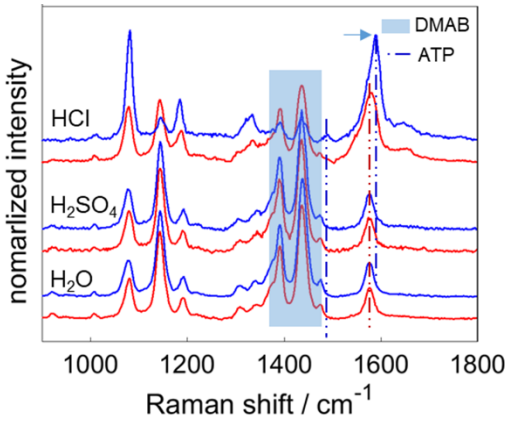

Figure 4.29 After 4-NTP converting to DMAB, H_2O, 0.05 M H_2SO_4 and 0.1 M HCl aqueous solution was dropped onto the AgPF and spectra were collected before at t = 0 min (red line) and after t = 10 min (blue line) 10 min, respectively.

4.2.6 Laser power-dependent reduction of 4-NTP

The role of hot electrons was also investigated in the reaction progress by observing the 4-NTP photoreduction with constant 0.01 M H^+- concentration and 1.0 M Cl^--concentration under different laser power settings. Figure 4.30 shows the time-resolved SERS spectra for laser power of 0.5 mW, 1 mW, 2 mW and 5 mW. Figure 4.31 shows k1 derived from this data as a function of laser power, illustrating that a higher laser power results in a faster reaction of 4-NTP. Because a higher laser power results in the generation of more hot electrons, the observation supports that hot-electrons consumed in the initial step of the 4-NTP reduction mechanism. With decreasing laser power, a longer delay is observed before 4-ATP formation, and in all cases no obvious DMAB bands are observed. This indicates the direct pathway is dominant regardless of laser power under these conditions which further supports the role of Cl^- in hot-electron recycling. The

reduction product, therefore, is dependent on both free hydrogen source (H^+) and hot electrons (Cl^-).

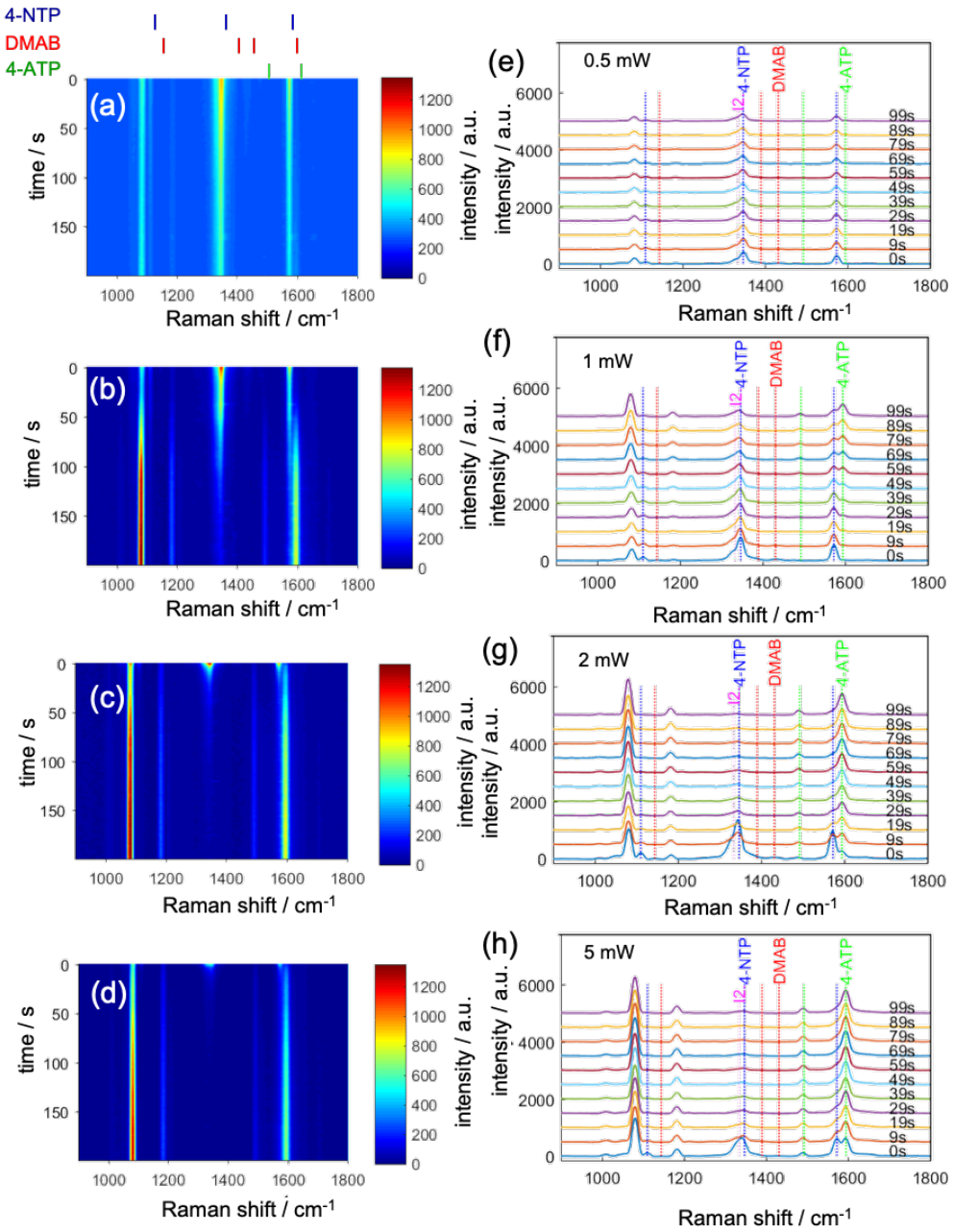

Figure 4.30 Continuous time-dependent spectra of the SERS spectra during the reduction of 4-NTP with laser power of 0.5 mW, 1 mW, 2 mW and 5 mW (a-d, respectively). The corresponding SERS spectra at discrete time points are shown in (e-h). In all cases, HCl and NaCl concentration in aqueous are 0.01 M and 1 M, respectively.

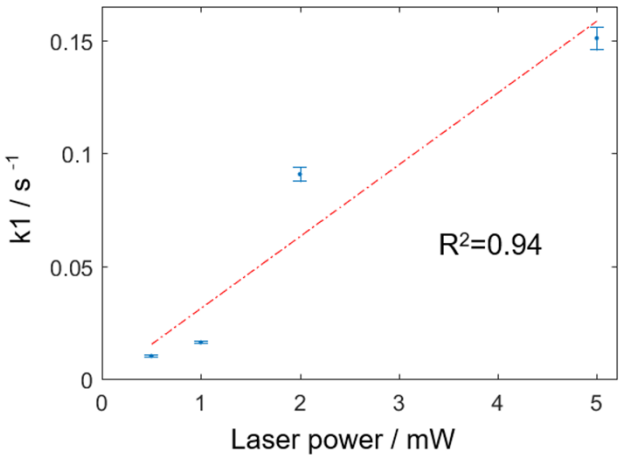

Figure 4.31 Rate constant k1 describing the 4-NTP decay as a function of laser power. In all cases, HCl and NaCl concentration in aqueous are 0.01 M and 1 M, respectively.

5 Summary and Outlook

5.1 Summary

This thesis contains two main parts. In the first part, we presented the application of SCRI combined with D_2O labeling to investigate the metabolic dynamics in mycobacteria (*M. smegmatis* and *M. tuberculosis*) and their responses to four different antibiotics. Incorporation of deuterium from D_2O in living cells induces the generation of C-D band in bacterial Raman spectra. Our findings indicate D_2O-Raman microscopic imaging is sensitive enough within a short corporation time and it can be used in individual mycobacterial cell imaging to sensitively visualize the heterogeneity of bacteria growth in individual cells. A linear combination of different components in the Raman spectra was carried out using multiple linear regression in MATLAB. Thus, the bacterial metabolic activity can be determined by calculating the ratio of deuterium-labeled macromolecules to non-deuterium-labeled macromolecules (CD / CH). By calculating the single-cell CD / CH Raman image, we found the metabolic heterogeneity between the bacterial poles and the bacterial middle. The metabolism is more active on the bacterial two sides than the metabolism in the bacterial middle. Importantly, with D_2O labeling combined with SCRI, it can not only observe the metabolic heterogeneity in the individual cell, but also the metabolic heterogeneity between different cells. Moreover, asymmetric and heterogeneous growth were both observed in *M. smegmatis* and *M. Tuberculosis*. Using the same technique, the variation in bacterial antibiotic sensitivity was also investigated and it found that the heterogeneous metabolic activity between the bacterial poles and the bacterial middle will decrease in the presence of antibiotics.

In the second part, a simple and low-cost method is proposed to fabricate a AgPF for SERS investigation of selective surface photocatalyzed reactions, and this is used to study the photoreduction of the photoreduction of 4-NTP to 4-ATP in a systematic set of controlled environments. In addition to the controlled concentrations possible through deposition of aqueous solutions on the chemical reactant absorbed on the AgPF, selective surface photocatalyed reactions could be observed without a chemical reducing agent. With AgPF, the first experimental evidence of the formation of the DMAB intermediate is presented in the photocatalyzed reduction of 4-NTP in the absence of a chemical reducing agent. Moreover, the influence of different H^+- and Cl^--concentrations on the kinetics of the reaction were quantitatively studied and a reaction mechanism was proposed for the reduction reaction that is consistent with the experimental measurements. The first reaction step which consumes 4-NTP follows a pseudo-first order assumption, though

deviations from this assumption appear at low H^+-concentration when the H^+ ions are no longer in excess. This observation in addition to the data showing that the reaction rate for this step increases linearly with respect to H^+-concentration implies that the initial reaction step involves one H^+ ion. In a strong acidic environment (H^+-concentration is 0.1 M), no SERS bands of DMAB were detected. When the H^+-concentration decreased below 0.01 M, considerable levels of DMAB were detected, and an increasing amount of DMAB was observed with decreasing H^+-concentration. In addition to observing the DMAB intermediate, we observe another strongly Raman active intermediate that is also formed only when the reaction progresses in low H^+-concentration environments. The results indicate that two reaction pathways coexist, and the dominating pathway depends on the H^+-concentration and the presence of Cl^- ions. This is consistent with the explanation that hot electrons generated from the photoexcitation participate in the reaction mechanism. The experiments using different laser powers also support this conclusion. The reaction in environments with extremely low H^+-concentration ($\leq$ 0.0001 M) progresses to yield very high SERS spectra in the region near the DMAB bands, indicating the possible formation of additional intermediate species. Further investigation is needed to understand the reaction mechanism at ultralow H^+-concentration conditions. The study of reaction kinetics and mechanism is useful for better understanding of hot-electron transformation during surface photoreactions.

5.2 Outlook

The results of D_2O combined Raman imaging offer valuable insights into single bacterial metabolism. To extend the work, efforts should be paid on the establishment of a standard procedure for fast Raman imaging acquisition and spectra processing. The reduction of Raman imaging acquisition might be obtained by using stimulated Raman. In addition, the large number of Raman spectra requires the development of advanced statistical techniques to extract valuable information. The improved procedure should be applicable for any other single bacterial cell.

For the mechanistic investigation of photocatalytic reactions, it is interesting to study the reaction behavior on a SERS substrate which can response to polarized laser. First, a suitable SERS substrate should be developed. The idea is to use small chiral molecules to obtain the chirality of AgNPs or nanostructures. In addition, this kind of SERS substrate is applicable for chiral sensing.

6 Abbreviations

4-ATP	4-aminothiopenol
AFM	Atomic force microscopy
AgNPs	Silver nanoparticles
AgPF	Silver plasmonic film
a. u.	Arbitrary unit
BDQ	Bedaquiline
BTZ	Benzothiazinone
$^{13}C_6$-Glc	^{13}C labeled glucose
$^{13}C_5$-Gln	^{13}C glutamine
C-D	Carbon-deuterium
CE	Chemical enhancement
C-H	Carbon-hydrogen
CT	Charge transfer
DCM	Dichloromethane NA
DMAB	4, 4-dimercaptoazobenzene
DMSO	Dimethyl sulfoxide
E-beam	Electron beam
EME	Electromagnetic enhancement
EF	Enhancement factor
FI-beam	Focused-ion beam
h	Hours
I_{SERS}	SERS intensity
LA	Liquid-air
LL	Liquid-liquid

LSPR	Localized surface plasma resonance
LUMO	Lowest unoccupied energy level
LZD	Linezolid
MBA	4-Mercaptobenzoic acid
MeLLF	Metal liquid like film
MIC	Minimum inhibitory concentration
MLR	Multiple linear regression
MNPs	Metal nanoparticles
MS	Mass spectroscopy
M. smegmatis	*Mycobacterium smegmatis*
M. tuberculosis	*Mycobacterium tuberculosis*
4-NTP	4-nitrothiopenol
NA	Numerical aperture
$NTP^{\bullet-}$	4-NTP anion radical
$^{15}N_2$-Gln	^{15}N-labeled glutamine
NA	Numerical aperture
NMR	Nuclear magnetic resonance
OD 600	Optical density at wavelength of 600 nm
RIF	Rifampicin
SCRI	Single-cell Raman imaging
SD	Standard deviation
SEM	Scanning electron microscopy
SERS	Surface-enhanced Raman microscopy
SIL	Stable isotopic labeling

SRS	Stimulated Raman scattering
TB	Tuberculosis
TBAN	Tetrabutylammonium nitrite
T80	Tween-80
μ	Dipole moment

7 References

7 References

1. Nguyen, L., Antibiotic resistance mechanisms in M. tuberculosis: an update. *Arch. Toxicol.* **2016,** *90* (7), 1585-1604.

2. Aldridge, B. B.; Fernandez-Suarez, M.; Heller, D.; Ambravaneswaran, V.; Irimia, D.; Toner, M.; Fortune, S. M., Asymmetry and aging of mycobacterial cells lead to variable growth and antibiotic susceptibility. *Science* **2012,** *335* (6064), 100-104.

3. Berry, D.; Mader, E.; Lee, T. K.; Woebken, D.; Wang, Y.; Zhu, D.; Palatinszky, M.; Schintlmeister, A.; Schmid, M. C.; Hanson, B. T.; Shterzer, N.; Mizrahi, I.; Rauch, I.; Decker, T.; Bocklitz, T.; Popp, J.; Gibson, C. M.; Fowler, P. W.; Huang, W. E.; Wagner, M., Tracking heavy water (D_2O) incorporation for identifying and sorting active microbial cells. *Proc. Natl. Acad. Sci. U.S.A.* **2015,** *112* (2), 194-203.

4. Shi, L.; Zheng, C.; Shen, Y.; Chen, Z.; Silveira, E. S.; Zhang, L.; Wei, M.; Liu, C.; de Se-Tomas, C.; Targoff, K.; Min, W., Optical imaging of metabolic dynamics in animals. *Nat. Commun.* **2018,** *9* (1), 2995.

5. Li, H. Z.; Bi, Q. F.; Yang, K.; Zheng, B. X.; Pu, Q.; Cui, L., D_2O-isotope-labeling approach to probing phosphate-solubilizing bacteria in complex soil communities by single-cell Raman spectroscopy. *Anal. Chem.* **2019,** *91* (3), 2239-2246.

6. Yang, K.; Li, H. Z.; Zhu, X.; Su, J. Q.; Ren, B.; Zhu, Y. G.; Cui, L., Rapid antibiotic susceptibility testing of pathogenic bacteria using heavy-water-labeled single-cell Raman spectroscopy in clinical samples. *Anal. Chem.* **2019,** *91* (9), 6296-6303.

7. Tao, Y.; Wang, Y.; Huang, S.; Zhu, P.; Huang, W. E.; Ling, J.; Xu, J., Metabolic-activity-based assessment of antimicrobial effects by D_2O-labeled single-cell Raman microspectroscopy. *Anal. Chem.* **2017,** *89* (7), 4108-4115.

8. Ueno, H.; Kato, Y.; Tabata, K. V.; Noji, H., Revealing the metabolic activity of persisters in mycobacteria by single-cell D_2O Raman imaging spectroscopy. *Anal. Chem.* **2019,** *91* (23), 15171-15178.

9. Wei, L.; Shen, Y.; Xu, F.; Hu, F.; Harrington, J. K.; Targoff, K. L.; Min, W., Imaging complex protein metabolism in live organisms by stimulated Raman scattering microscopy with isotope labeling. *ACS. Chem. Biol.* **2015,** *10* (3), 901-908.

10. Zhang, L.; Shi, L.; Shen, Y.; Miao, Y.; Wei, M.; Qian, N.; Liu, Y.; Min, W., Spectral tracing of deuterium for imaging glucose metabolism. *Nat. Biomed. Eng.* **2019,** *3* (5), 402-413.

11. Xie, W.; Schlucker, S., Surface-enhanced Raman spectroscopic detection of molecular chemo- and plasmo-catalysis on noble metal nanoparticles. *Chem. Commun. (Camb)* **2018,** *54* (19), 2326-2336.

12. Shi, C.; Zhang, W.; Birke, R. L.; Lombardi, J. R., Detection of short-lived intermediates in electrochemical reactions using time-resolved surface-enhanced Raman spectroscopy. *J. Phys. Chem.* **1990,** *94* (12), 4766-4769.

13. Xie, W.; Walkenfort, B.; Schlucker, S., Label-free SERS monitoring of chemical reactions catalyzed by small gold nanoparticles using 3D plasmonic superstructures. *J. Am. Chem. Soc.* **2013,** *135* (5), 1657-60.

14. Xie, W.; Herrmann, C.; Kompe, K.; Haase, M.; Schlucker, S., Synthesis of bifunctional Au/Pt/Au Core/shell nanoraspberries for in situ SERS monitoring of platinum-catalyzed reactions. *J. Am. Chem. Soc.* **2011,** *133* (48), 19302-19305.

15. Smekal, A., Zur Quantentheorie der Dispersion. *Sci. Nat.* **1923,** *11* (43), 873-875.

16. Singh, R.; Riess, F., Sir CV Raman and the story of the Nobel Prize. *Curr. Sci.* **1998,** *75* (9), 965-971.

17. Raman, C. V., A new radiation. **1928**.

18. King, F. W.; Van Duyne, R. P.; Schatz, G. C., Theory of Raman scattering by molecules adsorbed on electrode surfaces. *J. Chem. Phys.* **1978,** *69* (10), 4472-4481.

19. Siebert, F.; Hildebrandt, P., *Vibrational spectroscopy in life science*. John Wiley & Sons: 2008.

20. Raymer, M.; Walmsley, I.; Mostowski, J.; Sobolewska, B., Quantum theory of spatial and temporal coherence properties of stimulated Raman scattering. *Phys. Rev. A* **1985,** *32* (1), 332.

21. Wolfgang Langbein, P. B. In *Resonant Nonlinear Optical Microscopy*, Proceedings of the International School of Physics' Enrico Fermi', Wolfgang Langbein, P. B., Ed. IOS Press: **201**4; pp 141-173.

22. Kainosho, M.; Torizawa, T.; Iwashita, Y.; Terauchi, T.; Mei Ono, A.; Guntert, P., Optimal isotope labelling for NMR protein structure determinations. *Nature* **2006,** *440* (7080), 52-57.

23. Fan, T. W.; Lorkiewicz, P. K.; Sellers, K.; Moseley, H. N.; Higashi, R. M.; Lane, A. N., Stable isotope-resolved metabolomics and applications for drug development. *Pharmacol. Therapeut.* **2012,** *133* (3), 366-391.

24. Sun, R. C.; Fan, T. W. M.; Deng, P.; Higashi, R. M.; Lane, A. N.; Le, A.-T.; Scott, T. L.; Sun, Q.; Warmoes, M. O.; Yang, Y., Noninvasive liquid diet delivery of stable isotopes into mouse models for deep metabolic network tracing. *Nat. Commun.* **2017,** *8* (1), 1-10.

25. Lane, A. N.; Higashi, R. M.; Fan, T. W. M., NMR and MS-based stable isotope-resolved metabolomics and applications in cancer metabolism. *TrAC-Trend Anal. Chem.* **2019,** *120*, 115322.

26. Lorenz, B.; Wichmann, C.; Stockel, S.; Rosch, P.; Popp, J., Cultivation-free Raman spectroscopic investigations of bacteria. *Trends Microbiol.* **2017,** *25* (5), 413-424.

27. Popp, J.; Tuchin, V. V.; Chiou, A.; Heinemann, S. H., Handbook of Biophotonics, Vol. 1: Basics and techniques. Wiley-VCH Verlag GmbH & Co. KGaA, Weinheim: **2011**.

28. Li, M.; Huang, W. E.; Gibson, C. M.; Fowler, P. W.; Jousset, A., Stable isotope probing and Raman spectroscopy for monitoring carbon flow in a food chain and revealing metabolic pathway. *Anal. Chem.* **2013,** *85* (3), 1642-1649.

29. Kubryk, P.; Niessner, R.; Ivleva, N. P., The origin of the band at around 730 cm^{-1} in the SERS spectra of bacteria: a stable isotope approach. *Analyst* **2016,** *141* (10), 2874-2878.

30. Xu, J.; Zhu, D.; Ibrahim, A. D.; Allen, C. C. R.; Gibson, C. M.; Fowler, P. W.; Song, Y.; Huang, W. E., Raman deuterium isotope probing reveals microbial metabolism at the single-cell level. *Anal. Chem.* **2017,** *89* (24), 13305-13312.

31. Wang, Y.; Huang, W. E.; Cui, L.; Wagner, M., Single cell stable isotope probing in microbiology using Raman microspectroscopy. *Curr. Opin. Biotechnol.* **2016,** *41*, 34-42.

32. Huang, W. E.; Stoecker, K.; Griffiths, R.; Newbold, L.; Daims, H.; Whiteley, A. S.; Wagner, M., Raman-FISH: combining stable-isotope Raman spectroscopy and fluorescence in situ hybridization for the single cell analysis of identity and function. *Environ. Microbiol.* **2007,** *9* (8), 1878-1889.

33. Wang, Y.; Ji, Y.; Wharfe, E. S.; Meadows, R. S.; March, P.; Goodacre, R.; Xu, J.; Huang, W. E., Raman activated cell ejection for isolation of single cells. *Anal. Chem.* **2013,** *85* (22), 10697-10701.

34. Kubryk, P.; Kolschbach, J. S.; Marozava, S.; Lueders, T.; Meckenstock, R. U.; Niessner, R.; Ivleva, N. P., Exploring the potential of stable isotope (resonance) Raman microspectroscopy and surface-enhanced Raman scattering for the analysis of microorganisms at single cell level. *Anal. Chem.* **2015,** *87* (13), 6622-6630.

35. Angel, R.; Panholzl, C.; Gabriel, R.; Herbold, C.; Wanek, W.; Richter, A.; Eichorst, S. A.; Woebken, D., Application of stable-isotope labelling techniques for the detection of active diazotrophs. *Environ. Microbiol.* **2018,** *20* (1), 44-61.

36. Wang, Y.; Song, Y.; Tao, Y.; Muhamadali, H.; Goodacre, R.; Zhou, N. Y.; Preston, G. M.; Xu, J.; Huang, W. E., Reverse and multiple sable isotope probing to study bcterial metabolism and interactions at the single cell level. *Anal. Chem.* **2016,** *88* (19), 9443-9450.

37. Eichorst, S. A.; Strasser, F.; Woyke, T.; Schintlmeister, A.; Wagner, M.; Woebken, D., Advancements in the application of NanoSIMS and Raman microspectroscopy to investigate the activity of microbial cells in soils. *FEMS Microbiol. Ecol.* **2015,** *91* (10).

38. Takhaveev, V.; Heinemann, M., Metabolic heterogeneity in clonal microbial populations. *Curr. Opin. Microbiol.* **2018,** *45*, 30-38.

39. Hu, F.; Shi, L.; Min, W., Biological imaging of chemical bonds by stimulated Raman scattering microscopy. *Nat. Methods* **2019,** *16* (9), 830-842.

40. McQuillan A.J.: Hendra P.J.: Fleischmann M., Raman spectroscopic investigation of silver electrodes. *J. Electroanal. Chem. Interfacial Electrochem.* **1975,** *65* (2), 933-944.

41. Etchegoin, P.; Liem, H.; Maher, R. C.; Cohen, L. F.; Brown, R. J. C.; Hartigan, H.; Milton, M. J. T.; Gallop, J. C., A novel amplification mechanism for surface enhanced Raman scattering. *Chem. Phys. Lett.* **2002,** *366* (1-2), 115-121.

42. Gao, P.; Gosztola, D.; Weaver, M. J., Surface-enhanced raman spectroscopy as a probe of electroorganic reaction pathways. 1. Processes involving adsorbed nitrobenzene, azobenzene, and related species. *J. Phys. Chem.* **1988,** *92* (25), 7122-7130.

43. Zhang, G., Nanostructured substrates for surface-enhanced raman spectroscopy (SERS) and detection of biological and chemical analytes by electrical double layer (EDL) capacitance. U.S. Patent No. 8865402, **2014**.

44. Ando, J.; Fujita, K.; Smith, N. I.; Kawata, S., Dynamic SERS imaging of cellular transport pathways with endocytosed gold nanoparticles. *Nano Lett.* **2011,** *11* (12), 5344-5348.

45. Stiles, P. L.; Dieringer, J. A.; Shah, N. C.; Van Duyne, R. P., Surface-enhanced Raman spectroscopy. *Annu. Rev. Anal. Chem.* **2008,** *1*, 601-626.

46. Jin, R., Nanoparticle clusters light up in SERS. *Angew. Chem. Int. Ed.* **2010,** *49* (16), 2826-2829.

47. Le Ru, E. C.; Etchegoin, P. G., Quantifying SERS enhancements. *MRS Bull.* **2013,** *38* (8), 631-640.

48. Camden, J. P.; Dieringer, J. A.; Wang, Y.; Masiello, D. J.; Marks, L. D.; Schatz, G. C.; Van Duyne, R. P., Probing the structure of single-molecule surface-enhanced Raman scattering hot spots. *J. Am. Chem. Soc.* **2008,** *130* (38), 12616-12617.

49. Xia, Y.; Campbell, D. J., Plasmons: why should we care? *J. Chem. Educ.* **2007,** *84* (1), 91.

50. Schatz, G. C.; Young, M. A.; Van Duyne, R. P., Electromagnetic mechanism of SERS in *Surface-enhanced Raman scattering*, **2006**; pp 19-45.

51. Gersten, J.; Nitzan, A., Electromagnetic theory of enhanced Raman scattering by molecules adsorbed on rough surfaces. *J. Chem. Phys.* **1980,** *73* (7), 3023-3037.

52. Le Ru, E.; Etchegoin, P., Rigorous justification of the $|E|^4$ enhancement factor in surface enhanced Raman spectroscopy. *Chem. Phys. Lett.* **2006,** *423* (1-3), 63-66.

53. Ding, S.-Y.; Yi, J.; Li, J.-F.; Ren, B.; Wu, D.-Y.; Panneerselvam, R.; Tian, Z.-Q., Nanostructure-based plasmon-enhanced Raman spectroscopy for surface analysis of materials. *Nat. Rev. Materi.* **2016,** *1* (6), 1-16.

54. Ding, S.-Y.; You, E.-M.; Tian, Z.-Q.; Moskovits, M., Electromagnetic theories of surface-enhanced Raman spectroscopy. *Chem. Soc. Rev.* **2017,** *46* (13), 4042-4076.

55. Sharma, B.; Frontiera, R. R.; Henry, A.-I.; Ringe, E.; Van Duyne, R. P., SERS: Materials, applications, and the future. *Mater. Today* **2012,** *15* (1-2), 16-25.

56. Wu, D. Y.; Duan, S.; Ren, B.; Tian, Z. Q., Density functional theory study of surface-enhanced Raman scattering spectra of pyridine adsorbed on noble and transition metal surfaces. *J. Raman Spectrosc.* **2005,** *36* (6-7), 533-540.

57. Otto, A., The 'chemical'(electronic) contribution to surface-enhanced Raman scattering. *J. Raman Spectrosc.* **2005,** *36* (6-7), 497-509.

58. Otto, A., Theory of first layer and single molecule surface-enhanced Raman scattering (SERS). *Phys. Status Solidi A* **2001,** *188* (4), 1455-1470.

59. Wang, Y.; Sun, Z.; Wang, Y.; Hu, H.; Zhao, B.; Xu, W.; Lombardi, J. R., Surface-enhanced Raman scattering on mercaptopyridine-capped CdS microclusters. *Spectrochim. Acta A* **2007,** *66* (4-5), 1199-1203.

60. Islam, S. K.; Tamargo, M.; Moug, R.; Lombardi, J. R., Surface-enhanced Raman scattering on a chemically etched ZnSe surface. *J. Phys. Chem. C* **2013,** *117* (44), 23372-23377.

61. Sun, Z.; Zhao, B.; Lombardi, J. R., ZnO nanoparticle size-dependent excitation of surface Raman signal from adsorbed molecules: Observation of a charge-transfer resonance. *Appl. Phys. Lett.* **2007,** *91* (22), 221106.

62. Valley, N.; Greeneltch, N.; Van Duyne, R. P.; Schatz, G. C., A look at the origin and magnitude of the chemical contribution to the enhancement mechanism of surface-enhanced Raman spectroscopy (SERS): Theory and experiment. *J. Phys. Chem. Lett.* **2013,** *4* (16), 2599-2604.

63. Jensen, L.; Aikens, C. M.; Schatz, G. C., Electronic structure methods for studying surface-enhanced Raman scattering. *Chem. Soc. Rev.* **2008,** *37* (5), 1061-1073.

64. Ding, S. Y.; You, E. M.; Tian, Z. Q.; Moskovits, M., Electromagnetic theories of surface-enhanced Raman spectroscopy. *Chem. Soc. Rev.* **2017,** *46* (13), 4042-4076.

65. Kleinman, S. L.; Frontiera, R. R.; Henry, A.-I.; Dieringer, J. A.; Van Duyne, R. P., Creating, characterizing, and controlling chemistry with SERS hot spots. *Phys. Chem. Chem. Phys.* **2013,** *15* (1), 21-36.

66. Xu, H.; Bjerneld, E. J.; Aizpurua, J.; Apell, P.; Gunnarsson, L.; Petronis, S.; Kasemo, B.; Larsson, C.; Hook, F.; Kall, M. In *Interparticle coupling effects in surface-enhanced Raman scattering*, nanoparticles and nanostructured surfaces: Novel reporters with biological applications, International Society for Optics and Photonics: **2001**; pp 35-42.

67. Le Ru, E. C.; Grand, J.; Sow, I.; Somerville, W. R.; Etchegoin, P. G.; Treguer-Delapierre, M.; Charron, G.; Félidj, N.; Lévi, G.; Aubard, J., A scheme for detecting every single target molecule with surface-enhanced Raman spectroscopy. *Nano Lett.* **2011,** *11* (11), 5013-5019.

68. Pilot, R.; Signorini, R.; Durante, C.; Orian, L.; Bhamidipati, M.; Fabris, L., A review on surface-enhanced Raman scattering. *Biosensors (Basel)* **2019,** *9* (2), 57.

69. Moskovits, M., Surface-enhanced spectroscopy. *Rev. Mod. Phys.* **1985,** *57* (3), 783.

70. Raether, H., Surface plasmons on smooth surfaces. In *Surface plasmons on smooth and rough surfaces and on gratings*, Springer: 1988; pp 4-39.

71. Stiles, P. L.; Dieringer, J. A.; Shah, N. C.; Van Duyne, R. P., Surface-enhanced Raman spectroscopy. *Ann. Rev. Anal. Chem.* **2008,** *1*, 601-626.

72. Kneipp, K.; Wang, Y.; Kneipp, H.; Perelman, L. T.; Itzkan, I.; Dasari, R. R.; Feld, M. S., Single molecule detection using surface-enhanced Raman scattering (SERS). *Phys. Rev. Lett.* **1997,** *78* (9), 1667-1670.

73. Pazos-Perez, N.; Wagner, C. S.; Romo-Herrera, J. M.; Liz-Marzan, L. M.; Garcia de Abajo, F. J.; Wittemann, A.; Fery, A.; Alvarez-Puebla, R. A., Organized plasmonic clusters with high coordination number and extraordinary enhancement in surface-enhanced Raman scattering (SERS). *Angew. Chem. Int. Ed.* **2012,** *51* (51), 12688-12693.

74. Xie, W.; Schlucker, S., Hot electron-induced reduction of small molecules on photorecycling metal surfaces. *Nat. Commun.* **2015,** *6*, 7570.

75. Sardar, R.; Heap, T. B.; Shumaker-Parry, J. S., Versatile solid phase synthesis of gold nanoparticle dimers using an asymmetric functionalization approach. *J. Am. Chem. Soc.* **2007,** *129* (17), 5356-5357.

76. Coluccio, M. L.; Das, G.; Mecarini, F.; Gentile, F.; Pujia, A.; Bava, L.; Tallerico, R.; Candeloro, P.; Liberale, C.; De Angelis, F.; Di Fabrizio, E., Silver-based surface enhanced Raman scattering (SERS) substrate fabrication using nanolithography and site selective electroless deposition. *Microelectron. Eng.* **2009,** *86* (4-6), 1085-1088.

77. Xu, Y.; Konrad, M. P.; Trotter, J. L.; McCoy, C. P.; Bell, S. E., Rapid one-pot preparation of large freestanding nanoparticle-polymer films. *Small* **2017,** *13* (2), 1602163.

78. Le-The, H.; Berenschot, E.; Tiggelaar, R. M.; Tas, N. R.; van den Berg, A.; Eijkel, J. C. T., Large-scale fabrication of highly ordered sub-20 nm noble metal nanoparticles on silica substrates without metallic adhesion layers. *Microsyst. Nanoeng.* **2018,** *4* (1),1-10.

79. Sivashanmugan, K.; Liao, J.-D.; Liu, B. H., Focused-ion-beam-fabricated homogeneous acute-angled Au nanorods for surface-enhanced Raman scattering. *Appl. Phys. Express* **2015,** *8* (5), 052402.

80. Lin, B.; Chen, J.; Kannan, P.; Zeng, Y.; Qiu, B.; Guo, L.; Lin, Z., Rapid synthesis of a highly active and uniform 3-dimensional SERS substrate for on-spot sensing of dopamine. *Mikrochim. Acta* **2019,** *186* (4), 260.

81. Nam, N. N.; Bui, T. L.; Ho, N. T.; Son, S. J.; Joo, S.-W., Controlling photocatalytic reactions and hot electron transfer by rationally designing pore sizes and encapsulated plasmonic nanoparticle numbers. *J. Phys. Chem. C* **2019,** *123* (38), 23497-23504.

82. Li, Y.-S.; Cheng, J.; Wang, Y., Surface-enhanced Raman spectra of dyes and organic acids in silver solutions: chloride ion effect. *Spectrochim. Acta A:* **2000,** *56* (11), 2067-2072.

83. Pamies, R.; Cifre, J. G. H.; Espín, V. F.; Collado-González, M.; Baños, F. G. D.; de la Torre, J. G., Aggregation behaviour of gold nanoparticles in saline aqueous media. *J. Nanopart. Res.* **2014,** *16* (4), 2376.

84. Wang, M.; Zhang, Z.; He, J., A SERS study on the assembly behavior of gold nanoparticles at the oil/water interface. *Langmuir* **2015,** *31* (47), 12911-12919.

85. Guo, Q.; Xu, M.; Yuan, Y.; Gu, R.; Yao, J., Self-assembled large-scale monolayer of Au nanoparticles at the air/water interface used as a SERS substrate. *Langmuir* **2016,** *32* (18), 4530-4537.

86. Leopold, N.; Lendl, B., A new method for fast preparation of highly surface-enhanced Raman scattering (SERS) active silver colloids at room temperature by reduction of silver nitrate with hydroxylamine hydrochloride. *J. Phys. Chem. B* **2003,** *107* (24), 5723-5727.

87. Xu, Y.; Konrad, M. P.; Lee, W. W.; Ye, Z.; Bell, S. E., A method for promoting assembly of metallic and nonmetallic nanoparticles into interfacial monolayer films. *Nano Lett.* **2016,** *16* (8), 5255-5260.

88. Smirnov, E.; Peljo, P.; Scanlon, M. D.; Gumy, F.; Girault, H. H., Self-healing gold mirrors and filters at liquid-liquid interfaces. *Nanoscale* **2016,** *8* (14), 7723-7737.

89. Tian, L.; Su, M.; Yu, F.; Xu, Y.; Li, X.; Li, L.; Liu, H.; Tan, W., Liquid-state quantitative SERS analyzer on self-ordered metal liquid-like plasmonic arrays. *Nat. Commun.* **2018,** *9* (1), 3642.

90. Wang, H. H.; Liu, C. Y.; Wu, S. B.; Liu, N. W.; Peng, C. Y.; Chan, T. H.; Hsu, C. F.; Wang, J. K.; Wang, Y. L., Highly raman-enhancing substrates based on silver nanoparticle arrays with tunable sub-10 nm gaps. *Adv. Mater.* **2006,** *18* (4), 491-495.

91. Li, X.; Zhang, J.; Xu, W.; Jia, H.; Wang, X.; Yang, B.; Zhao, B.; Li, B.; Ozaki, Y., Mercaptoacetic acid-capped silver nanoparticles colloid: formation, morphology, and SERS activity. *Langmuir* **2003,** *19* (10), 4285-4290.

92. Rycenga, M.; Camargo, P. H.; Li, W.; Moran, C. H.; Xia, Y., Understanding the SERS effects of single silver nanoparticles and their dimers, one at a time. *J. Phys. Chem. Lett.* **2010,** *1* (4), 696-703.

93. dos Santos Jr, D. S.; Alvarez-Puebla, R. A.; Oliveira Jr, O. N.; Aroca, R. F., Controlling the size and shape of gold nanoparticles in fulvic acid colloidal solutions and their optical characterization using SERS. *J. Mater. Chem.* **2005,** *15* (29), 3045-3049.

94. Wu, Y.; Jiang, Y.; Zheng, X.; Jia, S.; Zhu, Z.; Ren, B.; Ma, H., Facile fabrication of microfluidic surface-enhanced Raman scattering devices via lift-up lithography. *Roc. Soc. Open Sci.* **2018,** *5* (4), 172034.

95. Liu, X.; Wang, J.; Wang, J.; Tang, L.; Ying, Y., Flexible and transparent surface-enhanced Raman scattering (SERS)-active metafilm for visualizing trace molecules via Raman spectral mapping. *Anal. Chem.* **2016,** *88* (12), 6166-6173.

96. Wei C.; Zhang, C.; Zhang, J.; Xu, M.; Yuan Y.; Yao, J, Insights into the heterogeneous distribution of SERS effect in plasmonic hot spots between Au@SiO2 monolayer film and gold single crystal plates. *RSC Adv.* **2017**, 48544-48553.

97. Lee, Y. H.; Shi, W.; Lee, H. K.; Jiang, R.; Phang, I. Y.; Cui, Y.; Isa, L.; Yang, Y.; Wang, J.; Li, S.; Ling, X. Y., Nanoscale surface chemistry directs the tunable assembly of silver octahedra into three two-dimensional plasmonic superlattices. *Nat. Commun.* **2015,** *6*, 6990.

98. Yue, W.; Wang, Z.; Yang, Y.; Chen, L.; Syed, A.; Wong, K.; Wang, X., Electron-beam lithography of gold nanostructures for surface-enhanced Raman scattering. *J. Micromech. Microeng.* **2012,** *22* (12), 125007.

99. Das, G.; Chirumamilla, M.; Toma, A.; Gopalakrishnan, A.; Zaccaria, R. P.; Alabastri, A.; Leoncini, M.; Di Fabrizio, E., Plasmon based biosensor for distinguishing different peptides mutation states. *Sci. Rep.* **2013,** *3*, 1792.

100. Kanipe, K. N.; Chidester, P. P.; Stucky, G. D.; Moskovits, M., Large format surface-enhanced raman spectroscopy substrate optimized for enhancement and uniformity. *ACS Nano* **2016,** *10* (8), 7566-7571.

101. Yu, Q.; Guan, P.; Qin, D.; Golden, G.; Wallace, P. M., Inverted size-dependence of surface-enhanced Raman scattering on gold nanohole and nanodisk arrays. *Nano Lett.* **2008,** *8* (7), 1923-1928.

102. Barcelo, S. J.; Kim, A.; Wu, W.; Li, Z., Fabrication of deterministic nanostructure assemblies with sub-nanometer spacing using a nanoimprinting transfer technique. *ACS Nano* **2012,** *6* (7), 6446-6452.

103. Petti, L.; Capasso, R.; Rippa, M.; Pannico, M.; La Manna, P.; Peluso, G.; Calarco, A.; Bobeico, E.; Musto, P., A plasmonic nanostructure fabricated by electron beam lithography as a sensitive and highly homogeneous SERS substrate for bio-sensing applications. *Vib. Spectrosc.* **2016,** *82*, 22-30.

104. Gartia, M. R.; Xu, Z.; Behymer, E.; Nguyen, H.; Britten, J. A.; Larson, C.; Miles, R.; Bora, M.; Chang, A. S.; Bond, T. C.; Liu, G. L., Rigorous surface enhanced Raman spectral characterization of large-area high-uniformity silver-coated tapered silica nanopillar arrays. *Nanotechnol.* **2010,** *21* (39), 395701.

105. Matricardi, C.; Hanske, C.; Garcia-Pomar, J. L.; Langer, J.; Mihi, A.; Liz-Marzan, L. M., Gold nanoparticle plasmonic superlattices as surface-enhanced Raman spectroscopy substrates. *ACS Nano* **2018,** *12* (8), 8531-8539.

106. Liu, L.; Zhang, Q.; Lu, Y.; Du, W.; Li, B.; Cui, Y.; Yuan, C.; Zhan, P.; Ge, H.; Wang, Z.; Chen, Y., A high-performance and low cost SERS substrate of plasmonic nanopillars on plastic film fabricated by nanoimprint lithography with AAO template. *AIP Adv.* **2017,** *7* (6), 065205.

107. Huang, Z.; Meng, G.; Huang, Q.; Chen, B.; Zhu, C.; Zhang, Z., Large-area Ag nanorod array substrates for SERS: AAO template-assisted fabrication, functionalization, and application in detection PCBs. *J. Raman Spectrosc.* **2013,** *44* (2), 240-246.

108. Hanske, C.; González-Rubio, G.; Hamon, C.; Formentín, P.; Modin, E.; Chuvilin, A.; Guerrero-Martínez, A.; Marsal, L. F.; Liz-Marzán, L. M., Large-scale plasmonic pyramidal supercrystals via templated self-assembly of monodisperse gold nanospheres. *J. Phys. Chem. C* **2017,** *121* (20), 10899-10906.

109. Zhou, Q.; Wen, J. Z.; Zhao, P.; Anderson, W. A., Synthesis of vertically-aligned zinc oxide nanowires and their application as a photocatalyst. *Nanomaterials (Basel)* **2017,** *7* (1), 9.

110. Fu, Q.; Zhan, Z.; Dou, J.; Zheng, X.; Xu, R.; Wu, M.; Lei, Y., Highly reproducible and sensitive SERS substrates with Ag inter-nanoparticle gaps of 5 nm fabricated by ultrathin aluminum mask technique. *ACS Appl. Mater. Inter.* **2015,** *7* (24), 13322-13328.

111. Freeman, R. G.; Grabar, K. C.; Allison, K. J.; Bright, R. M.; Davis, J. A.; Guthrie, A. P.; Hommer, M. B.; Jackson, M. A.; Smith, P. C.; Walter, D. G.; Natan, M. J., Self-assembled metal colloid monolayers: An approach to SERS substrates. *Science* **1995,** *267* (5204), 1629-1632.

112. Yun, S.; Park, Y. K.; Kim, S. K.; Park, S., Linker-molecule-free gold nanorod layer-by-layer films for surface-enhanced Raman scattering. *Anal. Chem.* **2007,** *79* (22), 8584-8589.

113. Luo, S. C.; Sivashanmugan, K.; Liao, J. D.; Yao, C. K.; Peng, H. C., Nanofabricated SERS-active substrates for single-molecule to virus detection in vitro: a review. *Biosens. Bioelectron.* **2014,** *61*, 232-240.

114. Andreou, C.; Mirsafavi, R.; Moskovits, M.; Meinhart, C. D., Detection of low concentrations of ampicillin in milk. *Analyst* **2015,** *140* (15), 5003-5005.

115. Krpetić, Ž.; Guerrini, L.; Larmour, I. A.; Reglinski, J.; Faulds, K.; Graham, D., Importance of nanoparticle size in colorimetric and SERS-based multimodal trace detection of Ni (II) ions with functional gold nanoparticles. *Small* **2012,** *8* (5), 707-714.

116. Sivashanmugan, K.; Liao, J.-D.; Liu, B. H.; Yao, C.-K.; Luo, S.-C., Ag nanoclusters on ZnO nanodome array as hybrid SERS-active substrate for trace detection of malachite green. *Sens. Actuators B: Chem.* **2015,** *207*, 430-436.

117. Wen, Z.-Q.; Li, G.; Ren, D., Detection of trace melamine in raw materials used for protein pharmaceutical manufacturing using surface-enhanced Raman spectroscopy (SERS) with gold nanoparticles. *Appl. Spectrosc.* **2011,** *65* (5), 514-521.

118. Zhou, H.; Yang, D.; Ivleva, N. P.; Mircescu, N. E.; Niessner, R.; Haisch, C., SERS detection of bacteria in water by in situ coating with Ag nanoparticles. *Anal. Chem.* **2014,** *86* (3), 1525-1533.

119. Zhou, H.; Yang, D.; Ivleva, N. P.; Mircescu, N. E.; Schubert, S.; Niessner, R.; Wieser, A.; Haisch, C., Label-free in situ discrimination of live and dead bacteria by surface-enhanced Raman scattering. *Anal. Chem.* **2015,** *87* (13), 6553-6561.

120. Kamińska, A.; Witkowska, E.; Kowalska, A.; Skoczyńska, A.; Ronkiewicz, P.; Szymborski, T.; Waluk, J., Rapid detection and identification of bacterial meningitis pathogens in ex vivo clinical samples by SERS method and principal component analysis. *Anal. Methods* **2016,** *8* (22), 4521-4529.

121. Cîntă Pînzaru, S.; Pavel, I.; Leopold, N.; Kiefer, W., Identification and characterization of pharmaceuticals using Raman and surface-enhanced Raman scattering. *J. Raman Spectrosc.* **2004,** *35* (5), 338-346.

122. Kim, K.; Choi, J.-Y.; Shin, K. S., Photoreduction of 4-nitrobenzenethiol on Au by hot electrons plasmonically generated from Ag nanoparticles: gap-mode surface-enhanced Raman scattering observation. *J. Phys. Chem. C* **2015,** *119* (9), 5187-5194.

123. Qi, D.; Yan, X.; Wang, L.; Zhang, J., Plasmon-free SERS self-monitoring of catalysis reaction on Au nanoclusters/TiO2 photonic microarray. *Chem. Commun. (Camb)* **2015,** *51* (42), 8813-8816.

124. Xiao, Q.; Sarina, S.; Waclawik, E. R.; Jia, J.; Chang, J.; Riches, J. D.; Wu, H.; Zheng, Z.; Zhu, H., Alloying gold with copper makes for a highly selective visible-light photocatalyst for the reduction of nitroaromatics to anilines. *ACS Catal.* **2016,** *6* (3), 1744-1753.

125. He, L.; Liu, C.; Tang, J.; Zhou, Y.; Yang, H.; Liu, R.; Hu, J., Self-catalytic stabilized Ag-Cu nanoparticles with tailored SERS response for plasmonic photocatalysis. *Appl. Surf. Sci.* **2018,** *434*, 265-272.

126. Zhang, K.; Zhao, J.; Ji, J.; Liu, B., Synthesis of micro-sized shell-isolated 3D plasmonic superstructures for in situ single-particle SERS monitoring. *Nanoscale* **2016,** *8* (15), 7871-7875.

127. Rodal-Cedeira, S.; Montes-García, V.; Polavarapu, L.; Solís, D. M.; Heidari, H.; La Porta, A.; Angiola, M.; Martucci, A.; Taboada, J. M.; Obelleiro, F.; Bals, S.; Pérez-Juste, J.; Pastoriza-Santos, I., Plasmonic Au@Pd nanorods with boosted refractive index susceptibility and SERS efficiency: A multifunctional platform for hydrogen sensing and monitoring of catalytic reactions. *Chem. Mater.* **2016,** *28* (24), 9169-9180.

128. Blaser, H. U., Chemistry. A golden boost to an old reaction. *Science* **2006,** *313* (5785), 312-313.

129. Zhao, L. B.; Huang, Y. F.; Liu, X. M.; Anema, J. R.; Wu, D. Y.; Ren, B.; Tian, Z. Q., A DFT study on photoinduced surface catalytic coupling reactions on nanostructured silver: selective formation of azobenzene derivatives from para-substituted nitrobenzene and aniline. *Phys. Chem. Chem. Phys.* **2012,** *14* (37), 12919-12929.

130. Zhao, L.-B.; Chen, J.-L.; Zhang, M.; Wu, D.-Y.; Tian, Z.-Q., Theoretical study on electroreduction of p-nitrothiophenol on silver and gold electrode surfaces. *J. Phys. Chem. C* **2015,** *119* (9), 4949-4958.

131. Wolter, A.; Niessner, R.; Seidel, M., Preparation and characterization of functional poly(ethylene glycol) surfaces for the use of antibody microarrays. *Anal. Chem.* **2007,** *79* (12), 4529-45237.

132. Wiegand, I.; Hilpert, K.; Hancock, R. E., Agar and broth dilution methods to determine the minimal inhibitory concentration (MIC) of antimicrobial substances. *Nat. Protoc.* **2008,** *3* (2), 163.

133. Toporski, J.; Dieing, T.; Hollricher, O., Confocal Raman Microscopy. *Springer*, **2018**, 130-132

134. Sun, M.; Huang, Y.; Xia, L.; Chen, X.; Xu, H., The pH-controlled plasmon-assisted surface photocatalysis reaction of 4-aminothiophenol to p,p′-dimercaptoazobenzene on Au, Ag, and Cu colloids. *J. Phys. Chem. C* **2011,** *115* (19), 9629-9636.

135. Zhu, H.; Ke, X.; Yang, X.; Sarina, S.; Liu, H., Reduction of nitroaromatic compounds on supported gold nanoparticles by visible and ultraviolet light. *Angew. Chem. Int. Ed.* **2010,** *49* (50), 9657-9661.

136. Liu, R.; He, Z.; Sun, J.; Liu, J.; Jiang, G., Tracking the fate of surface plasmon resonance-generated hot electrons by in situ SERS surveying of catalyzed reaction. *Small* **2016,** *12* (46), 6378-6387.

137. Choi, H. K., Lee, K. S., Shin, H. H., & Kim, Z. H., Identification of the first elementary step in the photocatalytic reduction of nitrobenzenethiols on a metallic surface. *J. Phys. Chem. Lett.*, **2016**, *7* (20), 4099-4104.

138. Choi, H. K.; Park, W. H.; Park, C. G.; Shin, H. H.; Lee, K. S.; Kim, Z. H., Metal-catalyzed chemical reaction of single molecules directly probed by vibrational spectroscopy. *J. Am. Chem. Soc.* **2016,** *138* (13), 4673-4684.

139. Linic, S.; Christopher, P.; Ingram, D. B., Plasmonic-metal nanostructures for efficient conversion of solar to chemical energy. *Nat. Mate.* **2011,** *10* (12), 911-921.

140. Lin, Z. Y.; Xiao, J.; Yan, J. H.; Liu, P.; Li, L. H.; Yang, G. W., Ag/AgCl plasmonic cubes with ultrahigh activity as advanced visible-light photocatalysts for photodegrading dyes. *J. Mater. Chem. A* **2015,** *3* (14), 7649-7658.